2006

Development Of Efficient Algorithms For Fluid-Structure Interaction Framework And Its Applications

Young Ho Kim
University of Alabama at Birmingham

DEVELOPMENT OF EFFICIENT ALGORITHMS FOR FLUID-STRUCTURE INTERACTION FRAMEWORK AND ITS APPLICATIONS

by

YOUNG HO KIM

JONG-EUN KIM, COMMITTEE CHAIR
DAVID L. LITTLEFIELD
ROY P. KOOMULLIL
ANDREAS S. ANAYIOTOS
MELINDA M. LALOR

A DISSERTATION

Submitted to the graduate faculty of The University of Alabama at Birmingham,
in partial fulfillment of the requirements for the degree of
Doctor of Philosophy

BIRMINGHAM, ALABAMA

2006

DEVELOPMENT OF EFFICIENT ALGORITHMS FOR FLUID-STRUCTURE INTERACTION FRAMEWORK AND ITS APPLICATIONS

YOUNG HO KIM

ABSTRACT

Computer-based simulation tools are becoming integrated to solve multiphysics and interactions between different disciplines. One of such problems that is of importance is fluid structure interaction (FSI). The goal of this study is to develop efficient and robust algorithms for a FSI framework. Due to the advantages of reusability of well-validated simulation codes for fluid and structural analysis, loosely-coupled methods are now dominant over directly-coupled methods. In loosely-coupled methods, it is important to transfer data efficiently and accurately between inherently unmatched grids used in different disciplines. In addition, efficient moving grid algorithms and time mapping techniques are essential. A new hybrid interpolation method for deformation mapping is suggested. The method provides efficient, accurate, and smooth interpolations in comparison to traditional methods. A partitioned volume grid movement algorithm is developed in which a local reference system is used for the viscous layer, and existent linear and semi-torsional spring analogy is used for the inviscid region. The algorithm reduces computational time significantly, and it prevents vertex-to-edge or vertex-to-face interpenetrations incurred in a large deformation by traditional spring analogy methods. Numerical results with test functions and an aircraft wing deformation illustrate the efficiency and accuracy of the suggested deformation mapping and volume grid movement methods. The validated algorithms are integrated into a FSI framework. Three FSI applications are demonstrated: pulsatile blood flow in an artificial straight/curved

stenotic artery with considering vessel compliance; pulsatile blood flow in in-vivo patient-specific femoral artery bifurcation; and an aircraft wing flutter.

DEDICATION

To my wife Misook Chang and daughters Youn-Su and Jisu

ACKNOWLEDGMENTS

I would like to express my deep appreciation to my major advisor, Dr. Jong-Eun Kim, for his constant encouragement and guidance. This work could not be completed without his consistent interest and support of this research. I am also indebted to his wife, Bong-Sung Park, for her sincere concern and encouragement.

Special thanks due to Dr. David L. Littlefield, Dr. Roy P. Koomullil, Dr. Andreas S. Anayiotos, and Dr. Melinda M. Lalor for their valuable time, advice and concern as committee members. I am grateful to all of the faculty and staff members in Department of Mechanical Engineering, especially to Dr. Bharat K. Soni for his support and concern.

My thanks extend to Dr. Yasushi Ito and Dr. Alan M. Shih for their helps in generating meshes and contributions to this research.

I owe a great debt of gratitude to my family in Korea for their boundless love and apprehension, especially to my parents for their special care and love.

Finally, I am deeply grateful to my dear wife, Misook Chang, for her love and patience, and to my lovely and sweet little daughters, Youn-Su and Jisu, who have brightened up my life.

TABLE OF CONTENTS

Page

LIST OF TABLES

Table ..... *Page*

LIST OF FIGURES

Figure..... *Page*

LIST OF FIGURES (Continued)

LIST OF FIGURES (Continued)

LIST OF FIGURES (Continued)

LIST OF ABBREVIATIONS

ALE	Arbitrary Lagrangian-Eulerian
CFA	Common femoral artery
CFD	Computational fluid dynamics
CILF	Curvature gradient index local fitting
CSD	Computational structural dynamics
CSS	Conventional serial staggered
CT	Computerized tomography
DUS	Doppler Ultrasound
FEM	Finite element method
FSI	Fluid structure interaction
IBA	Interpolation-based algorithm
IIM	Inverse isoparametric mapping
IPS	Infinite-plate spline
LCA	Lateral circumflex artery
LCAS	Local coordinate with an angle and shape function
LCTN	Local coordinate with two nodes
MRI	Magnetic resonance imaging
MQ	Multiquadrics
NURBS	Non-uniform rational B-spline

PAD	Peripheral arterial disease
PFA	Profunda femoral artery
PVA	Polyvinyl alcohol
RBF	Radial basis functions
RMS	Root mean-squared
SEDF	Strain energy density functions
SFA	Superficial femoral artery
SNR	Signal to noise ratio
TPS	Thin-plate spline
UDF	User defined function
WSS	Wall shear stress

CHAPTER 1

INTRODUCTION

1.1 Background

Numerous computational fluid dynamics (CFD) and computational structural dynamics (CSD) solvers have been developed over the decades independently. The results from computational simulation are now accurate enough to predict real physical phenomena. In addition, computer hardware has been improving rapidly. However, in real physical problems, certain phenomena such as FSI are related to the interaction of two or more disciplines. To solve multiphysics problems using computational methods, an efficient and accurate numerical scheme or tool is required.

There have been a number of approaches to solve fluid structure interaction (FSI) problems. They can be categorized into two groups: directly-coupled and loosely-coupled methods. The directly-coupled method is to generate a monolithic program by combining the governing equations used in two different media (fluid and structure) [1, 2], while the loosely-coupled method is to utilize an interface code to couple independent CFD and CSD solvers. The overview of modeling of FSI problem in aeroelasticity can be found in Bennett et al. [3] and Dowell et al. [4]. The review of FSI in liquid filled pipe systems can be found in Tijsseling et al. [5].

The directly-coupled method provides more accurate results than the loosely-coupled one. Aeroelasticity, a major application area of FSI, has been studied by many

researchers with this method. Behr [6] analyzed incompressible flow over two-dimensionalairfoil and cylinder using implicit stabilized space-time formulation for moving boundaries and interfaces, and a new stabilized velocity-pressure-stress formulation. Kroyer [7] solved supersonic flow past moving fins in two-dimensions using ADINA/ADINA-F. Carstens et al. [8] analyzed the flutter behavior of turbo-machinery blades in the time domain. The structural part of the governing aeroelastic equations is time-integrated according to the Newmark algorithm, while the unsteady air-loads are computed at every time step by a Navier–Stokes code. However, their applications with the directly-coupled methods are limited to two-dimensional or simple three-dimensional geometry, because the possibility of divergence of solution is increased as geometries become complicated. Another problem on the direct method is to yield ill-conditioned matrix system from the differences of properties and scales used in CFD and CSD formulations. Other applications with this method in aeroelasticity can be found in Refs. [9-13].

Another FSI application with this method is blood flow through flexible arteries. Tang et al. [14-16] analyzed the mechanical properties of carotid arteries and pulsatile/steady blood flow with simplified flexible artery wall. They also investigated the effect of lipid pool on wall mechanical properties of stenotic arteries interacted with blood flow [17].

Loosely-coupled method comes from an idea that FSI problems can be obtained efficiently and accurately using the well-proven CFD and CSD codes. With the advantages of reusability of well-proven simulation codes for each discipline, loosely-coupled methods have been employed by many researchers in the complex and large

scale problems. For example, an entire airplane, A502 Model, was analyzed by Whiting and Neill [18] using the panel method and an infinite plate spline interpolation technique. The flow over fighter F-16 was analyzed with non-uniform B-spline interpolation method using MDICE program by Love et al. [19].

In order to combine two different codes, an interface tool should be developed to control entire processes. This involves CFD and CSD data transfer using mapping techniques, time step control for job assignment to each discipline with/without parallel computer, and mesh control for moving boundary using numerical algorithms. There are many interpolation methods used in aerodynamic problems. The structural response of wing was monitored using inverse interpolation method [20]. Bilinear interpolation method was employed in analyzing micro aero vehicle wing with implicit multi-block pressure based Navier-Stokes equation [21]. Potsdam and Guruswamy [22] blended surface spline approximation and nearest surface point movement in analyzing transonic flow. Doi [23] analyzed turbo-machinery blade with iso-parametric interpolation function, parallel multiblock structure and dual time stepping. Other application with this method can be found in Refs. [24-28].

Assuming that the interaction between fluid and structure is not severe to the extent of considering remeshing the domain of fluid or structure, the following procedures must be considered to develop a tool (refer to as FSI framework) for loosely-coupled methods that can adopt any CFD and CSD solvers.

First, it is important to transfer data efficiently and accurately between inherently unmatched grids of different disciplines. In most cases, the fluid domain is discretized by a fine grid while the structural domain is discretized by a relatively coarse grid due to the

different nature of physics and numerical procedures. Among a variety of interpolation methods, making the right choice is a key factor in obtaining accurate solutions.

For the load transfer from fluid (fine grid) to structure (coarse grid), tracking methods with point-search algorithms and shape functions yield accurate results. For the deformation mapping from structure to fluid, two types of interpolation methods have been used: surface tracking and spline methods. The spline methods are popular because of smoothness and ease of implementation. However, these methods require significant computation time and the system matrices are prone to becoming ill-conditioned when used with unstructured grids, particularly with large numbers of nodes in complex three-dimensional systems. On the other hand, the surface tracking method can be applied to complex geometries with the advantage of finding matching pairs easily, but it may yield low accuracy at highly curved geometries.

Secondly, the fluid volume grid movement must be considered based on the interpolated deformation of fluid domain from the first step. The popular spring analogy methods require significant computation time. Moreover, the method yields the vertex-to-edge or vertex-to-face interpenetrations in case of large deformation especially in viscous layers.

1.2 Objectives and Outline

The goal of this study is to develop efficient algorithms for FSI framework and its applications to real world problems. The framework is comprised of a load projection, surface deformation, volume deformation, time mapping, and input/output control modules.

Chapter 2 describes a FSI framework using loosely-coupled method. The pre-requisites of CSD and CFD codes that can be used in FSI framework are explained. The roles of each module in the FSI framework are briefly introduced. The flow chart of loosely-coupled FSI framework is illustrated.

Chapter 3 explains a load projection module which is a component of the FSI framework. A surface tracking interpolation method used in the load transfer module guarantees the load transfer from fluid to solid in conservative and robust ways. The searching algorithms required for the implementation of the surface tracking method are described.

Chapter 4 presents a new hybrid interpolation method using Curvature gradient Index Local Fitting (CILF) for motion transfer used in surface deformation transfer module. CILF uses a surface spline method at local geometries having a high curvature gradient and a tracking method at the remaining geometries.

Chapter 5 addresses a new hybrid moving grid algorithm for volume deformation module. The new method uses an averaged point normal of moving surfaces at local geometries having a high curvature gradient, and it uses a simple local coordinate at the remaining geometries for viscous layers. A conventional spring analogy method is used for inviscid layers.

Chapter 6 explains the classical serial staggered time mapping method implemented in FSI framework with Perl script and Dos batch command.

Chapter 7 shows three applications of FSI framework. First, pulsatile flow through artificial straight/curved stenotic arteries is simulated. The pulsatile flow is modeled by sinusoidal waves and nonlinear hyper-elastic model is used for wall of the

arteries. The arteries are pre-stretched and pre-stressed to take residual stress into account. Secondly, flow patterns of an in-vivo complicated non-planar femoral artery bifurcation are analyzed and compared to the realistic magnetic resonance imaging (MRI) data. The pressure boundary condition at inlet is calculated from MRI velocity profiles. The velocity mapping of MRI data using an interpolation method at outlets is applied to observe the effect of skewed velocity profile from curvature of the arteries. An inverse method to find material coefficients in a constitutive model for in-vivo materials is employed. The last application is flutter simulation of an aircraft wing using time marching full dynamic FSI analysis instead of conventional modal approach.

CHAPTER 2

FLUID STRUCTURE INTERACTION FRAMEWORK USING LOOSELY-COUPLED METHOD

2.1 Pre-requisites of CSD and CFD Solvers

To maximize the advantage of re-use of existent well-validated CFD/CSD solvers without any modification in loosely-coupled method, some pre-requisites are needed as follows:

- Adoption of script command for batch of work
- Accessibility of input/output files for data transfer
- Arbitrary Lagrangian-Eulerian (ALE) in CFD solvers for moving grids
- Embedment of user-defined function for boundary/initial conditions and material constitutive models (optional)

Most of CFD/CSD solvers satisfy first three requirements. The last requirement is not embedded in most CFD/CSD solvers. Time-dependent boundary conditions or user-customized material properties are indispensable for some biomechanics applications.

2.2 Modules of FSI Framework

Assuming that CSD/CFD codes meet the pre-requisites, a FSI Framework can be developed to solve FSI problems. The framework consists of a load projection, surface deformation, volume deformation, time mapping, and input/output control modules. The data communication is transferred using natural files in the framework, because the

source code of two chosen commercial CFD/CSD solvers can not be accessed. This data communication scheme requires significant computation time to read and write data in hard drive, but it saves computational memory. This scheme is essential for enormous-memory-requirement application. In addition, the scheme can be used for CFD/CSD solvers in different platforms such as Linux, Windows, Unix, and etc [30]. However, if source codes of the existent CFD/CSD solvers in the same platform can be accessed by users and the memory is enough for saving all interface data, the data communication should be performed through run-time memory. The entire procedures of loosely-coupled FSI framework are illustrated in Fig. 2.1. The main roles of each module in the framework are as follows:

- Load projection module
    1. Convert fluid pressures to forces for all nodes on wetted fluid surface (common boundary between fluid and structure)
    2. Transfer the forces to all nodes on the wetted structural surface
- Surface deformation module
    1. Deform the wetted fluid surface based on deformation of the wetted structural surface with an interpolation method
- Volume deformation module
    1. Move fluid volume grids based on the wetted surface deformation
    2. Check negative volumes resulting from penetration of nodes into faces or edges

- Time mapping module
    1. Control iteration procedures for explicit/implicit coupling
    2. Generate script and batch files for automatic iterations
- Input/output module
    1. Convert input and output formats of each codes into a general format
    2. Extract the wetted surface information such as coordinates and node connectivity information
    3. Update the data transferred from each solver

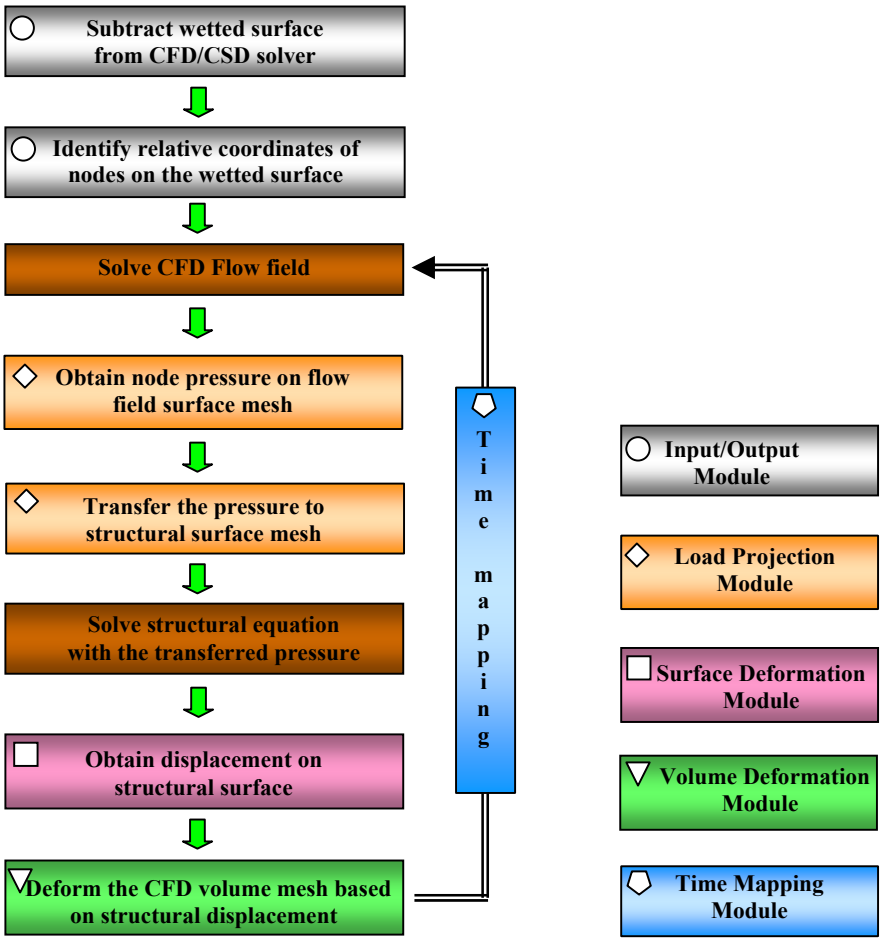

Fig. 2.1 FSI flowchart

CHAPTER 3

LOAD TRANSFER

3.1 Introduction

In loosely-coupled fluid structure interaction analysis, the data transfer between fluid and structure using interpolation techniques is required in space due to naturally unmatched grids between the two media. Load transfer, one mode of data transfer, enforces the equilibrant loads on the structural boundary interface based on pressure and tractions on the fluid boundary interface obtained from flow solvers.

3.2 Surface Tracking Interpolation Method

The surface tracking interpolation method requires a searching algorithm for identifying local coordinates of fluid nodes on the nearest structural element using the element connectivity information and area coordinates (shape functions). The integrated or given pressure/tractions of fluid cell element are converted to forces. Then, these forces are transferred to structural nodes using the linear shape functions. Fig. 3.1 shows the flow chart. The detail description of this method can be found in Ref. [31].

3.2.1 Searching algorithms

Several searching algorithms have been suggested such as neighbor to neighbor, brute-force, advanced-front, octree and vectorized grid for unstructured grids. Overview of these methods can be found in Ref. [32]. One of these methods, neighbor to neighbor

algorithm is outperformed in terms of speed and easy implementation. This method, however, may fail to identify the locations in some cases having specific geometries. Fig. 3.2 shows one of these cases. The other method called brute-force method shows slow performance but may yield robust results. The method searches all of the structural elements for one fluid node until a criterion meets.

In this study, the former method is mainly used to guarantee efficiency, and the latter is used for some nodes where the former fails to identify.

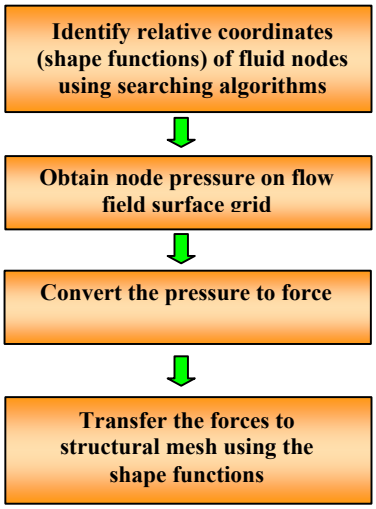

Fig. 3.1 Flow chart of the surface tracking interpolation method

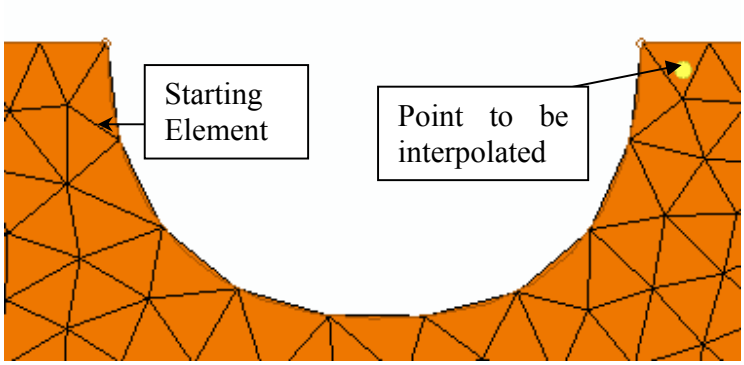

Fig. 3.2 Failure of neighbor to neighbor searching algorithm

3.2.1.1 Neighbor to neighbor search algorithm

This method is to find the shortest path starting from an arbitrary element to the destination (host) element using connectivity information of unstructured grid and area shape functions N_i (Fig. 3.3) with the path direction as shown in Fig. 3.4. The algorithms can be explained as follows:

1. Constitute a list of surrounding elements of each structural element using the connectivity information
2. Find d_s, the shortest distance between any two structural nodes
3. Choose a starting element arbitrarily, and calculate N_i of the point to be interpolated
4. Test a criterion as

$$\min(N_i, 1 - N_i) \geq 0, \forall i \tag{3.1}$$

5. If the criterion is satisfied and the projected distance from fluid node to structural element is shorter than d_s, save the index of the host structural element and exit. Otherwise, move to the neighbor element indicated by $\min(N_i)$ and go to step 4

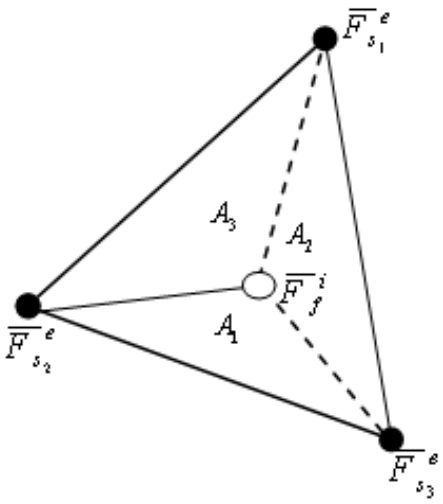

$$A = A_1 + A_2 + A_3$$

$$N_1 = A_1 / A$$

$$N_2 = A_2 / A$$

$$N_3 = A_3 / A$$

Shape functions (in 2D)

Fig. 3.3 Shape functions using area coordinate in a linear triangular element

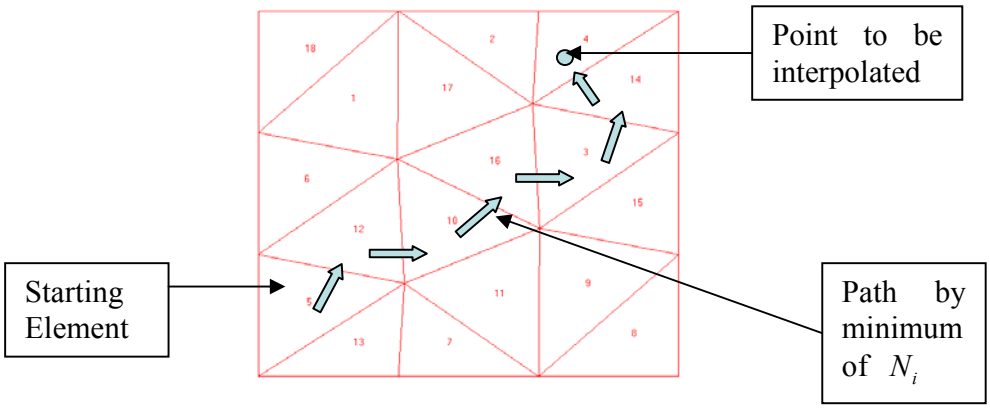

Fig. 3.4 Neighbor to neighbor search algorithm

In the step 5, if the algorithm fails due that the projected distance is greater than d_s, the brute-force algorithm is employed.

3.2.1.2 Brute-Force algorithm

This method can be implemented easily by testing Eq. (3.1) until the criterion satisfies for all of the fluid nodes. It's robust but slow.

3.2.2 Load transfer

Let's call the common boundary between two media wetted surface. In order to evaluate the fluid pressure and tracking forces on the structure, the load on a given wetted fluid surface (Γ_F) must be transferred to a wetted structure surface (Γ_s) in a conservative way. The force at each structural node can be written as

$$f_k = \sum_{l=1}^{l_F} [\Phi_l][c_{lk}] \tag{3.2}$$

where, l_F is the number of fluid nodes on the structural element, c_{lk} are constants depending on the chosen approximation schemes, and

$$\Phi_l = \int_{\Gamma_F} (-pn + \sigma_F \cdot n) D_l ds \tag{3.3}$$

where, p is the pressure, σ_F is fluid viscous stress tensor, n is the normal at a point on the wetted surface, D_l are some functions with global and local supports on Γ_F. In order to obtain Φ_l, the pressure and wall shear stress in each direction are extracted.

Because the pressure and stresses cannot be transferred directly due to different areas of the unmatched grids, they must be converted to an equivalent force. Every fluid node can be projected to the nearest structural element by the neighbor-to-neighbor and

brute-force search algorithm. Then, the equivalent forces on the fluid node can be distributed to structural elements as

$$\overline{F}^{e}_{s_j} = N_j \overline{F}^{i}_{f} \qquad i = 1,2,3 \tag{3.4}$$

where $\overline{F}^{i}_{f}$ is the equivalent force at the fluid node *i*, $\overline{F}^{e}_{s_j}$ is the point force at each node of structural element, *e*, as shown in Fig. 3.3.

After the forces at each node using Eq. (3.4) for all elements on the wetted structure surface are evaluated, the summed forces at each node will be used in computational structural analysis. Fig. 3.5 illustrates the load transfer from fluid to structural grid.

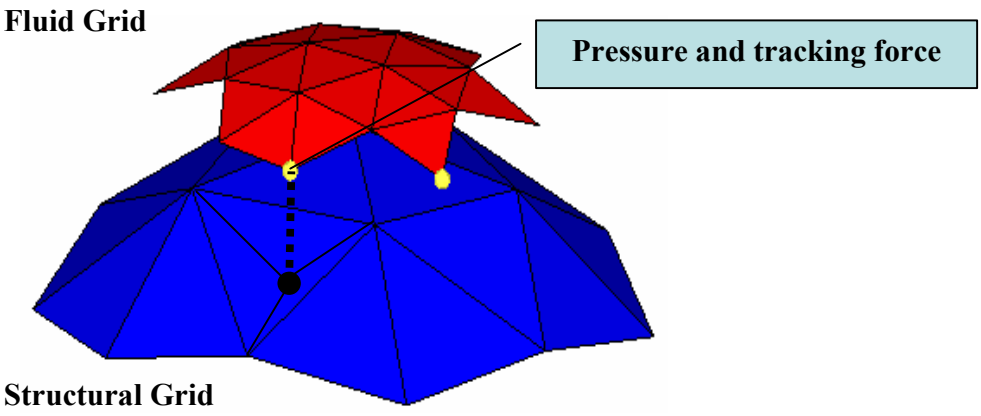

Fig. 3.5 Load transfer from fluid to structural grid

3.2 Results and Discussion

The load transfer of AGARD 445.6 wing is performed to demonstrate the accuracy of the method in three-dimensional domain. The unstructured fluid and

structural grids enclose the actual three-dimensional wing with 62,399 and 5,010 nodes, and 334,935 and 15,839 tetrahedron elements, respectively. The wetted surfaces as shown in Fig. 3.6 extracted from the tetrahedron elements have 21,414 for fluid and 8766 triangular elements for structural wing.

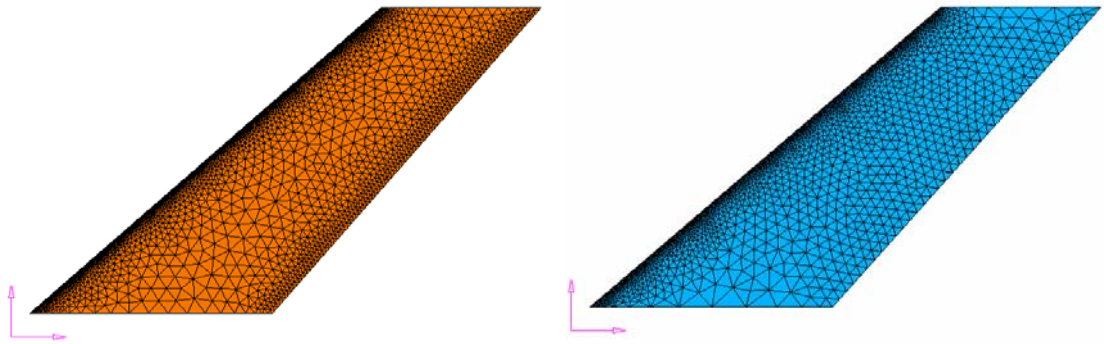

Fig. 3.6 Wetted fluid and structural surface grid

In order to test the implemented code, total pressure and shear stresses on each coordinate obtained at a time step of the flutter simulation of AGARD 445.6 wing are converted to forces, and the forces are transferred to the structural nodes. For the visualization purpose, the absolute forces on both grids are converted to pressure again as shown in Fig. 3.7. A good agreement was found between the pressure data on two grid sets. On the structural grid, however, the spotted force concentration is shown locally due to the different grid resolution. The spots may be smeared and smoothed considering higher order approximation using first derivative of load distribution, or graphical approximation such as overset grids and subdivision and interpolation.

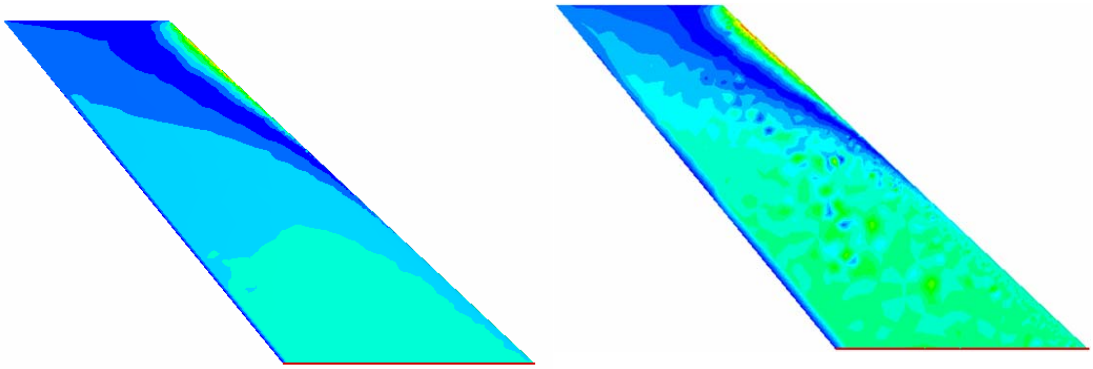

Fig. 3.7 Load transfer of AGARD 445.6 Wing

CHAPTER 4

NEW HYBRID INTERPOLATION METHOD FOR SURFACE DEFORMATION

4.1 Introduction

In the loosely-coupled method, the information between the independent codes needs to be transferred in efficient and accurate way. However, due to the inherently different spatial discretization of two codes, interpolation techniques are indispensable.

The numerous interpolation methods used in deformation mapping can be categorized into two groups: surface spline and tracking methods. The surface spline methods solve a linear equation consisting of radial basis functions to obtain a globally representative surface. Harder [33] presented a surface spline method for a plate known as infinite-plate spline (IPS). The IPS method provides reasonable results without additional constraints, such that input grid should be a rectangular array. This method is one of the most popular interpolation methods because of its ease of use and implementation. Duchon [34] presented a thin-plate spline (TPS) method that can represent an irregular surface with a function that minimizes the bending energy of a thin plate. TPS can be easily extended to multi-dimensional problems. In addition, TPS is a powerful tool for data interpolation on unstructured grids because the splines are invariant during scaling, rotation, and translation. Hardy [35] suggested a multiquadrics (MQ) method for reconstructing irregular topologies with scattered data using quadratic

basis functions similar to TPS. The basis functions used in IPS, TPS and MQ methods are recalled as radial basis functions (RBF). Beckert [20] addressed a multivariate interpolation scheme using RBF in three-dimensions. Samareh [36] proposed a method that uses a non-uniform rational B-spline (NURBS) representation to reduce the data transfer time. For all of the interpolation methods that can be categorized as surface spline methods, a system of equations needs to be solved to obtain interpolated information.

The surface tracking methods use natural coordinates associated with the deformed grid and a point-search algorithm. Murti and Valliappan [37] presented a method that uses inverse isoparametric mapping (IIM) for isoparametric finite elements to find a local coordinate (computational domain) from given global coordinate (physical domain). After finding the local coordinate, the shape functions of finite elements are used to interpolate physical quantities. Based on this method, Pidaparti [38] transferred structural and aerodynamic data for FSI application, and Byun and Guruswamy [39] solved wing-body aeroelasticity on a parallel computer using a domain decomposition approach. Maman and Farhat [40] provided a program called 'Matcher' using a consistent interpolation-based algorithm (IBA) by projecting fluid nodes to the structural mesh. Cebral [41] suggested a variation of 'Matcher' that guaranteed conservation of forces using the Galerkin method and an adaptive Gaussian integration scheme. This method, however, needs matrix inversion similar to spline methods. Farhat et al. [31] modified 'Matcher' to guarantee the conservation of forces without matrix inversion. Smith et al. [42] evaluated six interpolation methods, IIM, IPS, TPS, finite plate spline,

NURBS and MQ. They indicated that TPS and MQ are the most robust, cost-effective and accurate among the tested methods.

In FSI analysis solved in the loosely-coupled manner, spline methods are popular in mapping structural deformation onto the fluid domain because of smoothness and ease of implementation. However, these methods require significant CPU time and the system matrices are prone to becoming ill-conditioned when used with unstructured grids, particularly with large numbers of nodes in complex three-dimensional systems. A subdomain approach has been applied to TPS and MQ to reduce this instability [43]. On the other hand, the surface tracking method can be applied to complex geometries with the advantage of finding matching pairs (e.g. fluid node and structure element in FSI) easily, but it may yield low accuracy at highly curved geometries.

In this study, a new hybrid mapping method referred to as Curvature gradient Index Local Fitting (CILF) is suggested. CILF uses a surface spline method at local geometries having a high curvature gradient and a tracking method at the remaining geometries. The goal of this study is to develop an accurate and efficient surface-to-surface mapping method between unstructured fine and coarse grid systems by integrating three-dimensional TPS (one of the spline methods) and one of the tracking methods. The suggested method is applicable not only to FSI analysis, but to any multiphysics simulation with heterogeneous grids. Numerical results using two-dimensional analytical test functions, and three-dimensional applications such as sphere [44] and wing deformation are presented.

4.2 Mapping Methods

Due to the use of heterogeneous grid systems in multiphysics simulations, the mapping process is essential for data transfer. For instance, in FSI analysis, the pressure in flow field must be transferred to structural surface by equivalent tractions. On the other hand, the deformation of structure must be mapped to the fluid surface to accommodate remeshing or mesh motion of the fluid domain. In most cases, the fluid domain is discretized by a fine grid while the structural domain is discretized by a relatively coarse grid due to the different nature of physics and numerical procedures.

Alternatively, in general multiphysics modeling there may be two grid systems; one fine grid and another relatively coarse one as is shown in Fig. 4.1. It is necessary to transfer physical quantities (scalars or vectors) from one grid to the other in an accurate and efficient way.

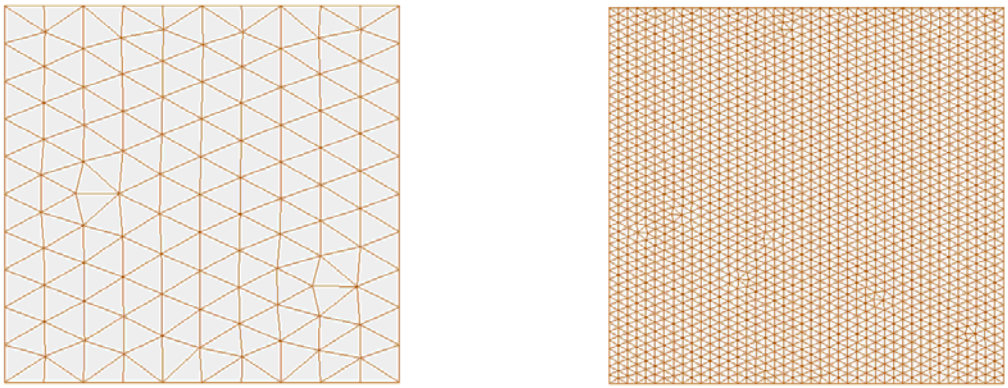

a) Coarse grid **b) Fine grid**

Fig. 4.1 Two different grid configurations

4.2.1 Mapping data from a fine grid onto a coarse grid

Physical quantities defined on the fine grid can be easily mapped onto a coarse grid using surface tracking methods with point-search algorithms. A quantity at a node in the coarse grid can be estimated by the values at nodes of the enclosing element in fine grid using the shape functions employed in previous load transfer. For a triangular element as shown in Fig. 3.3, this becomes

$$\overline{q}_c^i = \sum_{j=1}^{3} N_j \overline{q}_{f_j}^e \tag{4.1}$$

where $\overline{q}_c^i$ and $\overline{q}_{f_j}^e$ are any physical quantity (e.g. displacement vector) on the coarse and fine grids, respectively. The superscripts *i* and *e* are node and element indices, respectively.

4.2.2 Mapping data from a coarse grid onto a fine grid

For mapping data from coarse grids onto fine grids, there have been two different approaches: surface tracking and spline methods. In a manner similar to that outlined above, a quantity at a node in the fine grid can be estimated by the values at nodes of the enclosing element on the coarse grid using the shape functions

$$\overline{q}_f^i = \sum_{j=1}^{3} N_j \overline{q}_{c_j}^e \tag{4.2}$$

Node-based physical quantities can be transferred with these mapping methods. To understand the process clearly and visualize the results, geometry deformation will now be considered as an example of a physical quantity to be mapped.

When the surface tracking method is used for geometry mapping, Eq. (4.2) may not yield acceptable results for mapping of data from the coarse grid onto the fine grid due to

the non-smoothness introduced by different grid resolutions. To overcome this problem, nodes of the fine grid can be moved by initial distances [37] with the calculated displacement $\overline{q}_{fr}^{i}$ written as

$$\overline{q}_{fr}^{i} = \overline{q}_{f}^{i} + \overline{n}_{f}^{i} d_{f}^{i} \tag{4.3}$$

where $\overline{n}_{f}^{i}$ is a unit normal vector to the nearest coarse grid, and d_{f}^{i} is the initial distance measured from the initial grid configuration.

Another approach to yield a smooth interpolated surface is to use spline methods, in which the deformation of the coarse grid can be expressed as a surface function. For example, if a set of nodes on a curved thin plate is given, a function for the curvature can be obtained using splines based on the given nodes. TPS was indicated as a robust, cost-effective, and accurate method in Ref. [39]. The splines can be obtained by minimizing following energy function in the two-dimensional space

$$E = \iint_{R^2} \left(\frac{\partial^2 f}{\partial x^2} \right)^2 + 2\left(\frac{\partial^2 f}{\partial x \partial y} \right)^2 + \left(\frac{\partial^2 f}{\partial y^2} \right)^2 dxdy \tag{4.4}$$

This equation can be solved by using weighted sums of a radial basis function as follows:

$$f(x,y) = \sum_{i=1}^{m} a_i K_i(x,y) + a_{m+1} + a_{m+2}x + a_{m+3}y \tag{4.5}$$

where $K_i(x,y) = \frac{1}{16\pi}\phi(x,y)\ln\phi(x,y)$, $\phi(x,y) = (x-x_i)^2 + (y-y_i)^2$,

m is the number of nodes on the plate, and x_i and y_i are the coordinates of the given nodes. The spline coefficients a_i in Eq. (4.5) are determined by solving the system of linear equations

$$Aa = b \tag{4.6}$$

where a is a spline coefficient vector, A is a system matrix comprised of radial basis functions and b is a displacement vector.

4.2.3 A new hybrid mapping method

A new hybrid method referred to as CILF is suggested that uses a surface spline method for local grid regions where the curvature gradient index is satisfied by a criterion, and a tracking method for the rest of the grid. TPS without a subdomain approach is used for the surface spline method in CILF. A tracking method with initial distance vectors [37] is employed for the tracking scheme in CILF.

4.2.3.1 Curvature gradient index and criterion

In the first step, the curvature gradient indices of the coarse grid are calculated from the gradient of dihedral angles at a time step:

$$CI_e^l = \cos^{-1}(\overline{n}_e \cdot \overline{n}^l)\Big|_k^{k+1} \qquad l = 1,2,3 \qquad (4.7)$$

where CI_e^l denotes a curvature gradient index corresponding an adjacent element of element (e) in the coarse grid, k is a time step index, and $\overline{n}_e$ and $\overline{n}^l$ are unit normal vectors of the element and its adjacent element respectively.

The absolute value of the curvature gradient can be used as a criterion. Alternatively, a relative criterion can be determined as a percentage of the elements used in three-dimensional local TPS. After computing the index, all of the curvature gradient indices are sorted as an array in descending order. Then, a three-dimensional local TPS technique is applied.

4.2.3.2 Three-dimensional local TPS

The key feature of CILF is to apply TPS to the local grid that is assigned the spline method by the absolute or relative criterion based on the curvature gradient index. The three-dimensional local TPS suggested in this paper uses *element-based local splines* with a small data set, comprised of all nodes adjacent to the two end nodes along the edge of an element satisfying the threshold criterion, as is shown in Fig. 4.2. The local TPS can be achieved by the following steps:

Step 1: Project nodes (data set) to a plane parallel to the element flagged for TPS

Step 2: Calculate distances (d) from the nodes to the projected nodes (p)

Step 3: Form the three-dimensional matrix A and vector b as given in Eq. (10)

$$A = \begin{bmatrix} K & P \\ P^T & 0 \end{bmatrix}, \quad b = \begin{bmatrix} d_1 & \cdots & d_m & 0 & 0 & 0 & 0 \end{bmatrix}^T$$

$$K = \begin{bmatrix} K_1(p_{1_x}, p_{1_y}, p_{1_z}) & \cdots & K_m(p_{1_x}, p_{1_y}, p_{1_z}) \\ \vdots & & \vdots \\ K_1(p_{m_x}, p_{m_y}, p_{m_z}) & \cdots & K_m(p_{m_x}, p_{m_y}, p_{m_z}) \end{bmatrix}$$

$$P = \begin{bmatrix} 1 & p_{1_x} & p_{1_y} & p_{1_z} \\ \vdots & \vdots & \vdots & \vdots \\ 1 & p_{m_x} & p_{m_y} & p_{m_z} \end{bmatrix} \tag{4.8}$$

where

$$K_i(x, y, z) = \frac{1}{16\pi} \phi(x, y, z) \ln \phi(x, y, z)$$

$$\phi(x, y, z) = (x - x_i)^2 + (y - y_i)^2 + (z - z_i)^2$$

and m is the number of the nodes projected onto the plane.

Step 4: Obtain interpolated distances of all nodes on the fine grid of the element by

$$f(x,y,z)=\sum_{i=1}^{m}a_iK_i(x,y,z)+a_{m+1}+a_{m+2}x+a_{m+3}y+a_{m+4}z \tag{4.9}$$

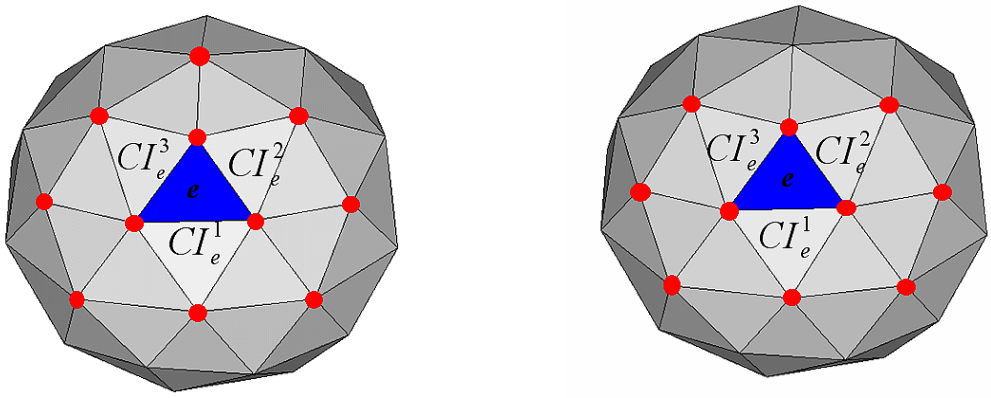

a) Neighbor nodes in case of $CI_e^1,\ CI_e^2,\ CI_e^3 \geq criterion$ or $two\ of\ them \geq criterion$

b) Neighbor nodes in case of $CI_e^1 \geq criterion$ and, $CI_e^2,\ CI_e^3 \leq criterion$

Fig. 4.2 Data set used for local TPS

4.3 Results and Discussion

4.3.1 Two-dimensional test functions

In order to demonstrate the accuracy and efficiency of the suggested method, four two-dimensional analytical test functions were chosen:

$$F_1(x,y)=(1+9x^2+16y^2)^{-1} \tag{4.10}$$

$$F_2(x,y)=1-((x^2+y^2)/2)^{1/2} \tag{4.11}$$

$$F_3(x,y)=1.5xe^{-x^2-y^2} \tag{4.12}$$

$$F_4(x,y)=(1.25+\cos(5.4y))/(6+6(3x-1)^2) \tag{4.13}$$

where $-1.5 \le x, y \le 1.5$. In this study, fine grid is comprised of 1968 nodes and coarse one has 128 nodes irregularly spaced on a plate as shown in Fig. 4.1. The coarse grid is deformed by the above equations, and then the deformed coarse grid is mapped onto the fine grid using conventional methods and CILF. The criterion for CILF is set to an absolute value, ±5 deg. To evaluate the accuracy of CILF method compared to IPS and the tracking method with an initial distance vector, the root mean-squared (RMS) errors are calculated as

$$RMS\ error = \sqrt{\sum_{k=1}^{n}\left[F(x_k, y_k) - f(x_k, y_k)\right]^2 \Big/ n} \tag{4.14}$$

where $F(x_k, y_k)$ is the original function, $f(x_k, y_k)$ the interpolated function, and *k* and *n* are node indices and the total number of nodes on the fine grid, respectively.

In terms of the accuracy, RMS errors of CILF are much smaller than those of surface tracking as shown in Table 4.1. The interpolated and original data of the four functions are illustrated in Fig. 4.3 and show the smoothness of CILF compared to surface tracking. In terms of the efficiency, CILF for the function F_1, applied with 37.5% of the elements interpolated by TPS, is about four times faster than the IPS method as is also shown in Table 4.2. The method is still 1.7 times faster than IPS, although CILF employs 96.2 % local TPS for the function F_3.

To demonstrate that CILF is much faster than IPS as the number of nodes is increased, the bell shape function F_1 with 236, 369, and 920 nodes is interpolated. The results shown in Table 3 indicate that CILF is up to 215 times faster than IPS. IPS requires significant CPU time to allocate and invert the matrix for the solution to the linear algebraic system needed to generate a global spline. CILF reduces the required

time by taking a maximum of 15 neighbor nodes for generating local splines. In addition, the use of small numbers of nodes can decrease a possibility of yielding ill-conditioned systems. The RMS errors of CILF shown in Table 4 are similar to those of IPS.

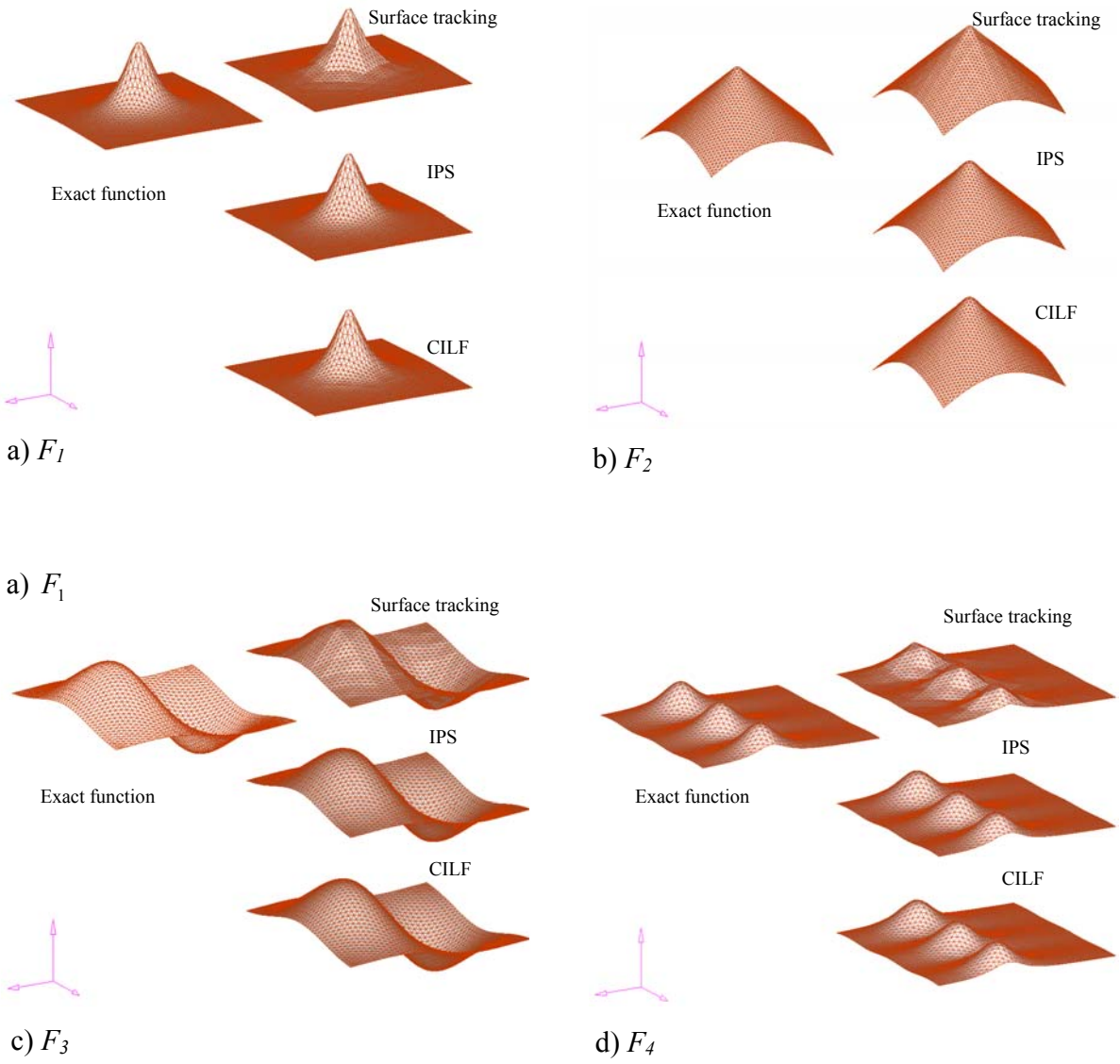

Fig. 4.3 Graphical comparison of surface tracking, IPS and CILF for four analytical test functions

Table 4.1 Comparison of RMS errors of test functions

	Surface Tracking	IPS	CILF
F_1	0.0124	0.0041	0.0048
F_2	0.0065	0.0026	0.0036
F_3	0.0112	0.0007	0.0023
F_4	0.0110	0.0033	0.0039

Table 4.2 Comparison of relative CPU time of test functions

	Surface Tracking	IPS	CILF
F_1	0.16	3.80	1 (37.5)*
F_2	0.10	2.30	1 (77.9)
F_3	0.07	1.74	1 (96.1)
F_4	0.14	2.12	1 (63.9)

* percentage of the number of elements interpolated by local TPS

Table 4.3 Relative CPU time versus total number of nodes

Number of nodes	Surface Tracking	IPS	CILF
128	0.16	3.80	1
236	0.14	11.94	1
369	0.11	30.29	1
920	0.08	215.85	1

Table 4.4 RMS errors versus total number of nodes

Num. of nodes	Surface Tracking	IPS	CILF
128	0.0124	0.0041	0.0048
236	0.0090	0.0023	0.0030
369	0.0061	0.0013	0.0017
920	0.0029	0.0003	0.0006

4.3.2 Three-dimensional mapping of a sphere deformation

Three-dimensional mapping can be achieved without any difficulty using CILF. An example of sphere deformation is chosen as shown in Fig. 4.4. The coarse grid is deformed into an ellipsoid using scaling factors of 2.5, 1.25, and 1.5 in x, y, and z direction respectively, and then mapped onto the fine grid. The sphere has unit radius, with 441 and 3789 nodes for coarse and fine grids, respectively. The result using the IPS is not shown here because a global spline cannot be obtained without using a subdomain technique. Therefore, only the surface tracking method and CILF are compared in this case. The efficiency and accuracy of CILF are controlled by a relative criterion that determines the number of elements used in local TPS. As illustrated in Fig. 4.5, RMS errors and CPU times are approximately in reverse proportion. The relative criterion can thus be chosen by considering the trade-off between accuracy and efficiency for a given problem. The RMS errors are not changed appreciably, but the roughness around edges from the surface tracking method is smoothed notably by CILF, as shown in the magnified view in Fig. 4.6.

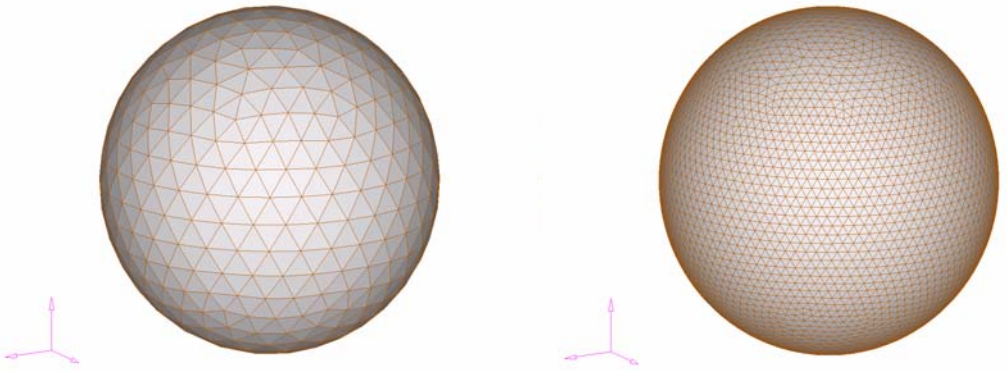

a) Coarse grid **b) Fine grid**

Fig. 4.4 Sphere grids used for three-dimensional mapping

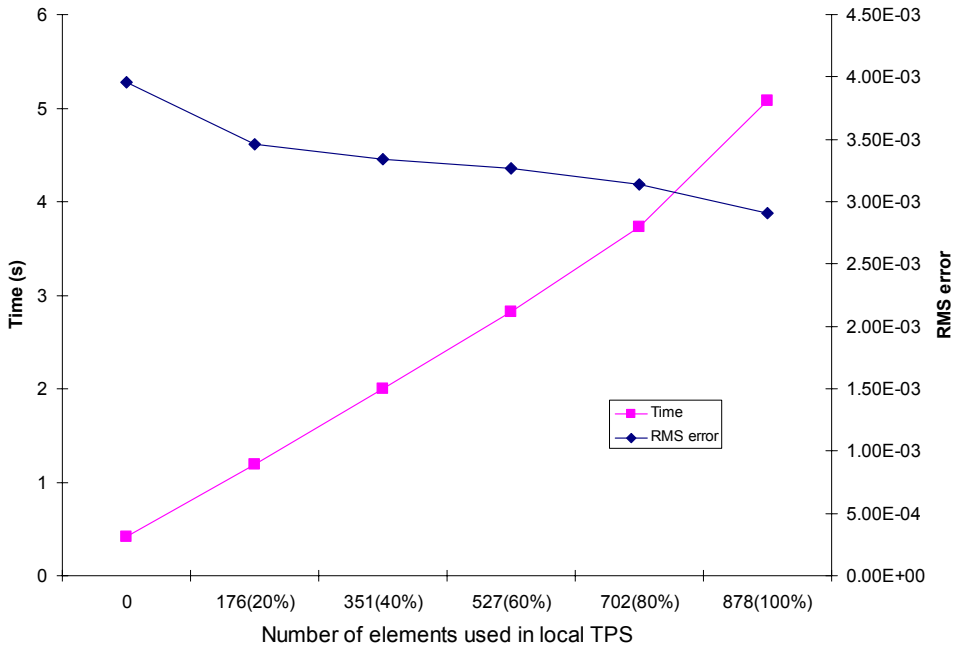

Fig. 4.5 CPU time and RMS error versus number of elements used in local TPS

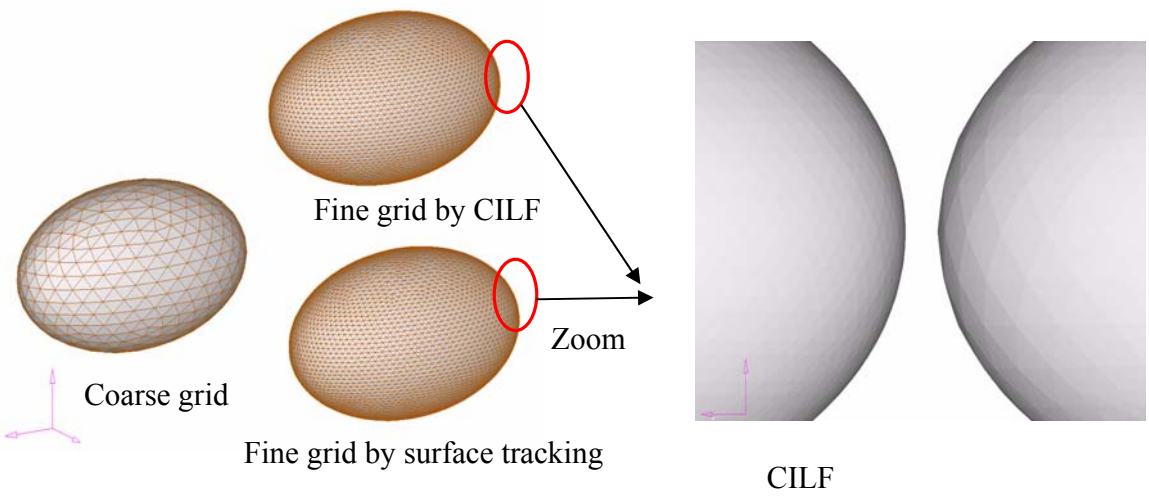

Fig. 4.6 Graphical comparison of surface tracking and CILF for mapping of sphere deformation

4.3.3 AGARD wing deformation

As an example of CILF applied to a FSI problem, the motion transfer of the fourth vibration mode of the AGARD 445.6 wing is performed. The unstructured fluid and structural grids enclose the actual three-dimensional wing surface with 35870 and 3282 nodes respectively. Fig. 4.7 shows interpolated fluid grid based on the structural deformation using CILF. Fig. 4.8 shows that CILF and IPS provide smoother contour lines than the tracking method. The CPU time in Table 4.5 shows that CILF is 130 times faster than IPS. The effect of the relative criterion on smoothness is shown in Fig. 4.9. The CPU time required varies approximately in proportion to the value of the criterion, as shown in Table 4.6. The relative criterion can thus be chosen by considering the trade-off between smoothness and efficiency for a given problem.

a) Structural grid **b) Interpolated fluid grid by CILF**

Fig. 4.7 A mode shape of the AGARD 445.6 wing.

Table 4.5 Comparison of CPU times for wing deformation mapping

Methods	Relative CPU time
Tracking	0.32
IPS	130.48
CILF	1.0

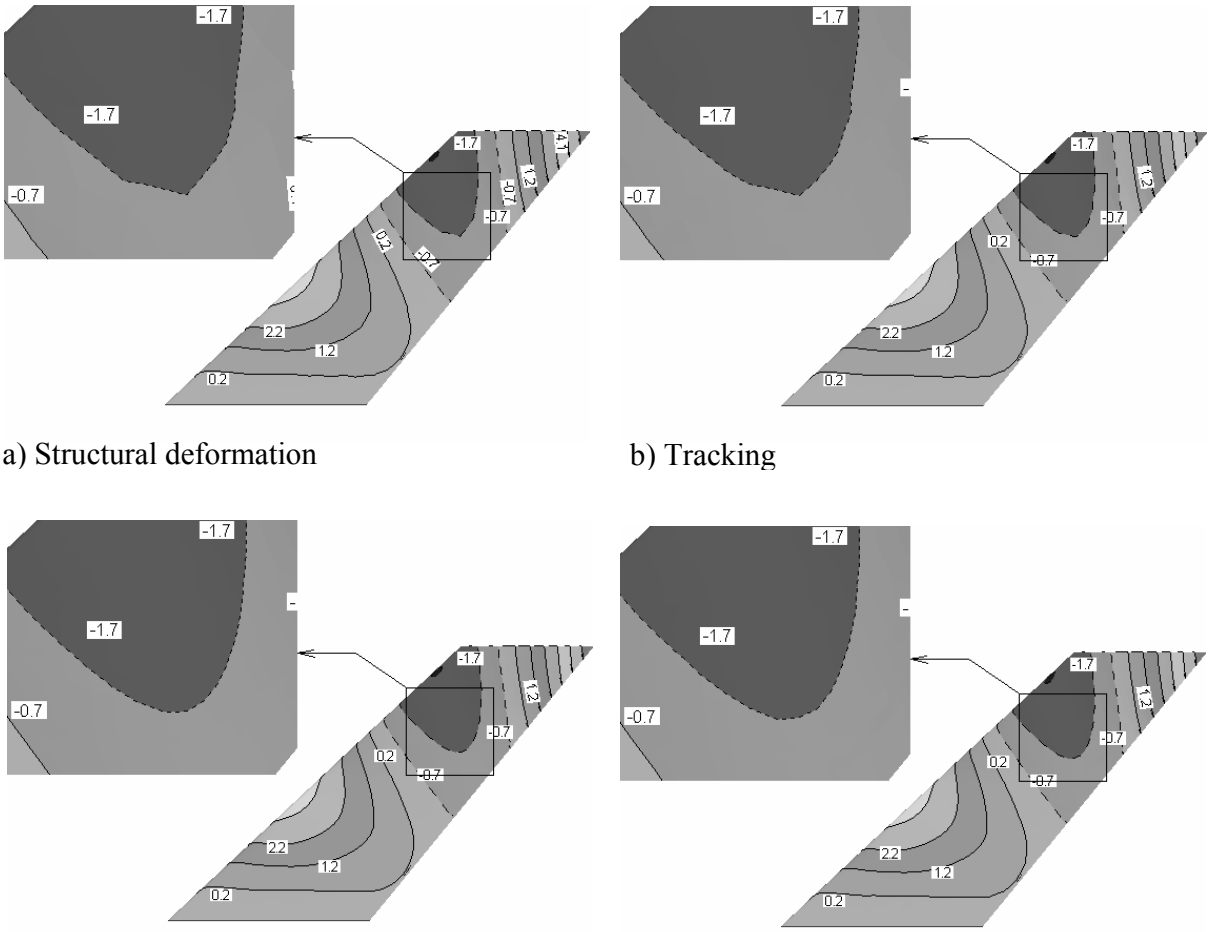

a) Structural deformation b) Tracking

c) IPS d) CILF

Fig. 4.8 AGARD 445.6 wing deformation contour

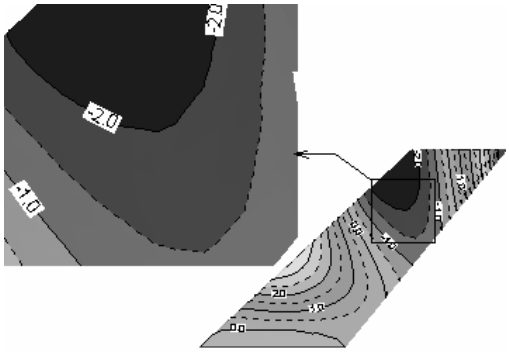

a) 0 %

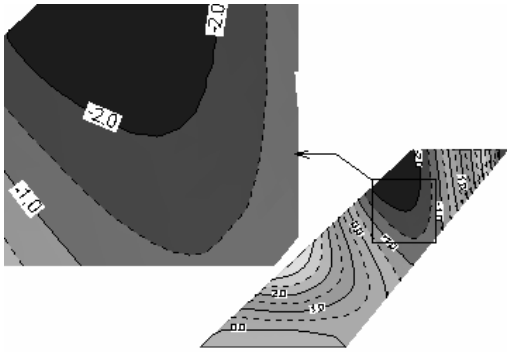

b) 25 %

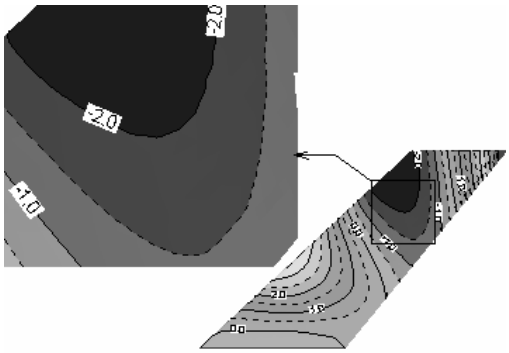

c) 50 %

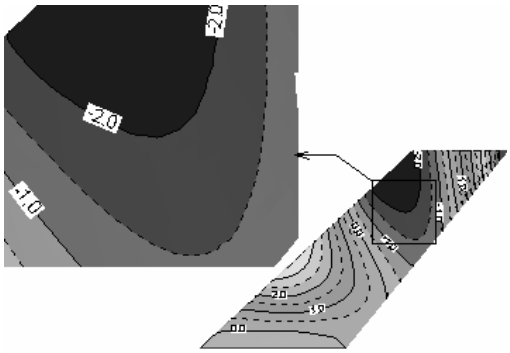

d) 75 %

Fig. 4.9 Smoothness by relative criteria

Table 4.6 CPU time by relative criteria

Structural elements (%)	Relative CPU time
0	1.000
25	1.865
50	2.506
75	3.130

4.4 Summary

A new hybrid mapping method, named as Curvature gradient Index Local Fitting (CILF) for data transfer between unmatched unstructured grids is suggested to map surfaces in loosely-coupled FSI problems. This approach overcomes numerical instabilities and excessive computation time incurred by interpolating a large data set in the spline methods as well as the low accuracy from tracking methods. The results presented show that the method provides efficient, accurate and smooth interpolations in comparison to the traditional methods.

CHAPTER 5

MOVING MESH ALGORITHM FOR VOLUME DEFORMATION

5.1 Introduction

In solving fluid structure interaction (FSI) problems using the loosely-coupled method, an efficient and robust volume mesh movement algorithm is indispensable to moving the fluid volume mesh based on the common interface surface deformation mapped by CILF (described in chapter 4). The most common scheme used for unstructured grids is the spring analogy method. Batina [45] suggested a simple method by replacing each mesh edge with a spring whose stiffness is inversely proportional to the edge length. This method, however, did not prevent some vertices from crossing over opposite edges. The vertex crossing problem was partly solved by adding torsional spring to each vertex in a two-dimensional application. This problem was also solved by attaching additional linear spring to confine the movement of each vertex [47]. The method was revealed to be more stable on iterating procedure required in FSI simulation than the torsional spring method in some cases. The method was applied to a three-dimensional problem [47]. Degand and Farhat [48], Murayama et al. [49] and Burg [50] presented a three dimensional extension of the torsional spring method. Zeng and Ethier [51] suggested a semi-torsional spring that substitutes for entire complex 3-D torsional spring. This method is easy to implement and provides good quality of mesh.

Another approach in moving mesh is to make use of the elastostatic analogy method. In the method, the fluid field is asssumed as a pseudo-elastic solid [52, 53]. The method, however, has the same penetration problem as spring analogy when a linear elastostatic field is confront with severe element distortion. To solve this problem, a method using pseudo non-homogeneous material based on geometrical information has been introduced. The elastic modulus is inversely proportional to the cell volume/area [54, 55], or the distance from the deforming surface [56]. This modulus is changed to the weighted coefficients and applied to the spring analogy [57, 58]. These methods worked well, but they required significant computation time and memory especially due to condensation of nodes at boundary layer.

In this study, a partitioned volume mesh movement algorithm is suggested. The new method employs a simple and efficient topological local coordinate method for moving the meshes in boundary layer, and the conventional semi-torsional spring analogy for moving the meshes in inviscid region. The local coordinate method uses two types of local coordinates depending on a curvature gradient index to construct boundary layers normal to the moved surface. An averaged point normal of moving surfaces and its relative angle to the local directional vector is used at local geometries having a high curvature gradient, while a simple local coordinate is used at local geometries having a low curvature gradient. Entire volume grid movements from the fourth vibration modes of the AGARD 445.6 and NACA0012 wings are tested to show the efficiency of the suggested method.

5.2 Volume Deformation Algorithms for Viscous Layers

High aspect ratio grids are required for analyzing fluid flow such as turbulence and shear thinning right around the wall in the rheology and aerodynamics. It is, however, difficult to implement the movement of high aspect ratio grids due to the silver type tetrahedral elements that yield negative volumes easily. Moreover, they make the system of linear equation used in spring analogy method more ill-conditioned than moderate aspect ratio grids. In this study, a partitioned method is suggested in moving unstructured boundary layer grid based on a curvature gradient index to solve the problem.

The local coordinate of a node in boundary layers is determined based on the curvature gradient. At local geometries having a high curvature gradient, a relative angle and shape functions of the node are employed to identify its local coordinate. The relative angle can be calculated using an averaged point normal of surrounding surface elements. The shape functions are calculated by identifying the location of projected node of the node at the closest surface element. At local geometries having a low curvature gradient, the nearest node on the moving surface and two neighbored nodes of its surrounding elements are used to find its local coordinate.

5.2.1 A local coordinate with an angle and shape functions (LCAS)

Consider a node P_0, its nearest node P_{01} on the moving fluid interface surface, and surrounding nodes of the P_{01} in Fig. 5.1. An angle α can be calculated with

$$\alpha = \cos^{-1}\left(\frac{\overline{n}_{p_{01}} \cdot (\overline{p}_0 - \overline{p}_{01})}{\left\|\overline{n}_{p_{01}}\right\|\left\|\overline{p}_0 - \overline{p}_{01}\right\|}\right) \tag{5.1}$$

where, $\overline{n}_{p_{01}}$ is a point normal of P_{01}.

After projecting P_0 on the nearest surface element along $\overline{n}_{p_{01}}$ direction, the shape functions N_i (i = 1, 2, and 3) can be calculated from the definition of shape functions with the projected node P_{0p}

$$\begin{Bmatrix} N_1 \\ N_2 \\ N_3 \end{Bmatrix} = \begin{bmatrix} p_{01x} & p_{02x} & p_{03x} \\ p_{01y} & p_{02y} & p_{03y} \\ p_{01z} & p_{02z} & p_{03z} \end{bmatrix}^{-1} \begin{Bmatrix} p_{0px} \\ p_{0py} \\ p_{0px} \end{Bmatrix} \tag{5.2}$$

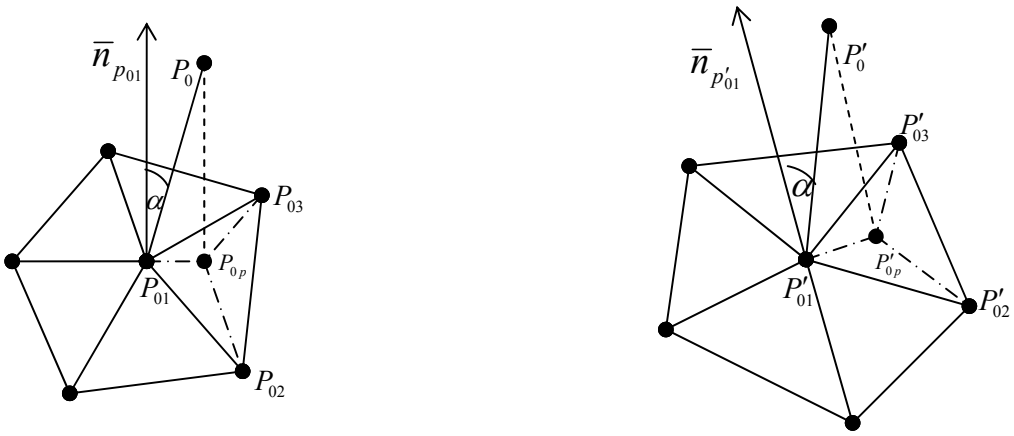

a) Before movement **b) After movement**

Fig. 5.1 Local coordinates of P_1 with an angle and shape functions

With the calculated angle and shape functions, the moved point P'_0 can be determined as following steps

Step 1: Calculate a new point normal $\overline{n}_{p'_{01}}$ based on the moved fluid common interface surface.

Step 2: Obtain P'_{0p}, a projected point of p'_{01} using

$$\begin{Bmatrix} p'_{0px} \\ p'_{0py} \\ p'_{0px} \end{Bmatrix} = \begin{bmatrix} p'_{01x} & p'_{02x} & p'_{03x} \\ p'_{01y} & p'_{02y} & p'_{03y} \\ p'_{01z} & p'_{02z} & p'_{03z} \end{bmatrix} \begin{Bmatrix} N_1 \\ N_2 \\ N_3 \end{Bmatrix} \tag{5.3}$$

and draw a line from P'_{0p} along $\overline{n}_{p'_{01}}$ direction

Step 3: Draw a line from P'_{01} with the calculated angle as shown in Fig. 5.1 on the plane including $\overline{n}'_{p_0}$ and the line obtained from step 2. The drawn line will intersect the line drawn from step 2. The cross point is the moved point P'_0 of P_0

5.2.2 A local coordinate with two nodes (LCTN)

In order to determine three arbitrary axes to define a local coordinate for a node P, the nearest node P_1 and its two neighbored nodes P_2 and P_3 whose angle is close to 90 degrees are chosen as shown in Fig. 5.2. Based on the three nodes, two unit vectors $\overline{n}_{p_1p_2}$, $\overline{n}_{p_1p_3}$, and one normal vector of the triangle $p_1p_2p_3$, $\overline{n}_{p_1p_2p_3}$ representing three axes for the local coordinate system are determined as following equations [59].

$$\overline{n}_{p_1p_2} = \frac{\overline{p}_2 - \overline{p}_1}{\left\|\overline{p}_2 - \overline{p}_1\right\|}, \overline{n}_{p_1p_3} = \frac{\overline{p}_3 - \overline{p}_1}{\left\|\overline{p}_3 - \overline{p}_1\right\|}, \overline{n}_{p_1p_2p_3} = \frac{\overline{n}_{p_1p_3} \times \overline{n}_{p_1p_2}}{\left\|\overline{n}_{p_1p_3} \times \overline{n}_{p_1p_2}\right\|} \tag{5.4}$$

A new coordinate P_l of P in the local coordinate system can be written with origin P_1 as:

$$\begin{Bmatrix} P_{lx} \\ P_{ly} \\ P_{lz} \end{Bmatrix} = \begin{bmatrix} \overline{n}_{p_1p_2x} & \overline{n}_{p_1p_3x} & \overline{n}_{p_1p_2p_3x} \\ \overline{n}_{p_1p_2y} & \overline{n}_{p_1p_3y} & \overline{n}_{p_1p_2p_3y} \\ \overline{n}_{p_1p_2z} & \overline{n}_{p_1p_3z} & \overline{n}_{p_1p_2p_3z} \end{bmatrix}^{-1} \begin{Bmatrix} P_x - P_{1x} \\ P_y - P_{1y} \\ P_z - P_{1z} \end{Bmatrix} \tag{5.5}$$

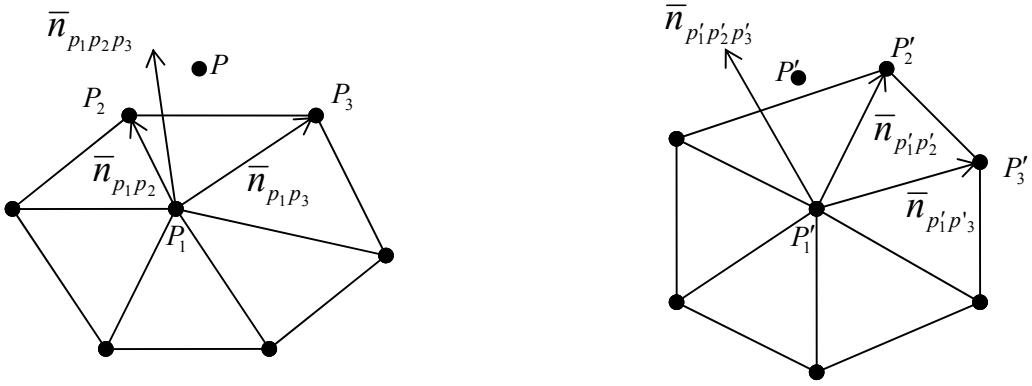

a) Before movement **b) After movement**

Fig. 5.2 Local coordinate of P with three arbitrary axes

With the P_l, the moved point P' can be calculated using

$$\begin{Bmatrix} P'_x \\ P'_y \\ P'_z \end{Bmatrix} = \begin{bmatrix} \overline{n}_{p'_1p'_2x} & \overline{n}_{p'_1p'_3x} & \overline{n}_{p'_1p'_2p'_3x} \\ \overline{n}_{p'_1p'_2y} & \overline{n}_{p'_1p'_3y} & \overline{n}_{p'_1p'_2p'_3y} \\ \overline{n}_{p'_1p'_2z} & \overline{n}_{p'_1p'_3z} & \overline{n}_{p'_1p'_2p'_3z} \end{bmatrix}^T \begin{Bmatrix} P_{lx} \\ P_{ly} \\ P_{lz} \end{Bmatrix} + \begin{Bmatrix} P'_{1x} \\ P'_{1y} \\ P'_{1z} \end{Bmatrix} \tag{5.6}$$

5.3 Volume Deformation Algorithms for Inviscid Region

5.3.1 Linear spring analogy

In the three-dimensional linear spring analogy, spring stiffness is inversely proportional to the distance of the edges. Let's consider the stiffness k_{ij} of the edge e_{ij} in Fig. 5.3. The stiffness is

$$k_{ij} = l_{ij}^{-1} \tag{5.6}$$

where (x_i, y_i, z_i) and (x_j, y_j, z_j) are the coordinate of nodes i and j, and l_{ij} is $[(x_j - x_i)^2 + (y_j - y_i)^2 + (z_j - z_i)^2]^{1/2}$. Given a set of nodal displacements from the movement of the wetted surface, the interior nodal displacement can be obtained by solving following equations iteratively until all the forces are in equilibrium

$$\Delta x_i^{n+1} = \frac{\sum_{j=1}^{m} k_{ij} \Delta x^n}{\sum_{j=1}^{m} k_{ij}}, \quad \Delta y_i^{n+1} = \frac{\sum_{j=1}^{m} k_{ij} \Delta y^n}{\sum_{j=1}^{m} k_{ij}}, \quad \Delta z_i^{n+1} = \frac{\sum_{j=1}^{m} k_{ij} \Delta z^n}{\sum_{j=1}^{m} k_{ij}} \tag{5.7}$$

where, n is iteration number and m is the number of the nodes connected to node i.

A local displacement u_{ij} must be considered in the global coordinate system to get the global displacement U_{ij} of nodes in a network of springs. Then U_{ij} is

$$U_{ij} = T_{ij} u_{ij} \tag{5.8}$$

Similarly, a global force F_{ij} can be obtained from a force f_{ij} at the local coordinate system following as:

$$F_{ij} = T_{ij} f_{ij} \tag{5.9}$$

The local force f_{ij} can be calculated as:

$$f_{ij} = k_{ij} u_{ij} \tag{5.10}$$

Substitute f_{ij} to F_{ij} using Eq. (5.8) and (5.9)

$$F_{ij} = T_{ij} k_{ij} T_{ij}^{-1} U_{ij} \tag{5.11}$$

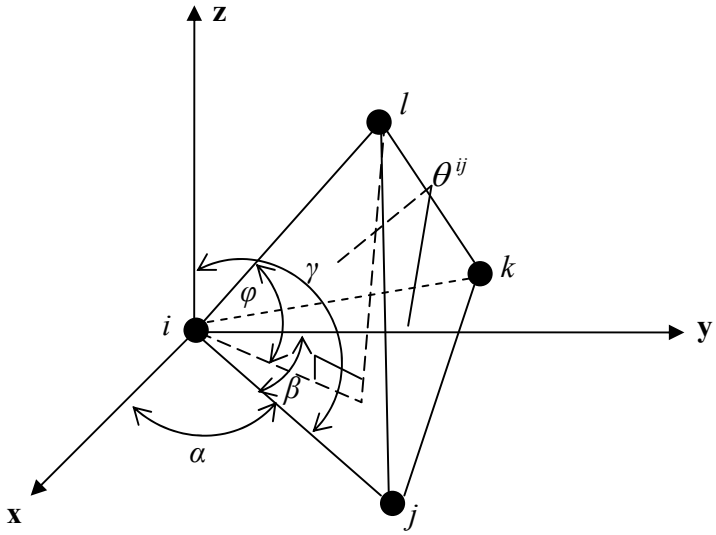

Fig. 5.3 Diagram of nodes of one tetrahedron element surrounding a node *i*

Let's define $T_{ij} k_{ij} T_{ij}^{-1}$ as K_{ij}^{linear}, then the K_{ij}^{linear} in the three-dimension is

$$K_{ij}^{linear} = \frac{1}{l_{ij}} \begin{bmatrix} R_{ij} & -R_{ij} \\ -R_{ij} & R_{ij} \end{bmatrix} \tag{5.12}$$

where, $R_{ij} = \begin{bmatrix} \cos^2\alpha & \cos\alpha\cos\beta & \cos\alpha\cos\gamma \\ \cos\alpha\cos\beta & \cos^2\beta & \cos\beta\cos\gamma \\ \cos\alpha\cos\gamma & \cos\beta\cos\gamma & \cos^2\gamma \end{bmatrix}$

After summing up the forces at each node, the static equilibrium equation can be solved using a Gauss-Seidel iterative method.

5.3.2 Semi-torsional spring analogy

The stiffness of a conventional torsion spring on a node is inversely proportional to the sine of the angle which prevent intrusion of the node to its opposite faces or edges. In the three-dimensional conventional torsional analogy, the derivative of φ with respect to a spatial variable ξ is [50]

$$\frac{\partial \varphi}{\partial \xi} = \frac{\sin \varphi}{\cos \varphi}\left(\frac{1}{V^{ijkl}} \frac{\partial V^{ijkl}}{\partial \xi} - \frac{1}{A^{ijk}} \frac{\partial A^{ijk}}{\partial \xi} - \frac{1}{l^{ij}} \frac{\partial l^{ij}}{\partial \xi} \right) \tag{5.13}$$

where, V^{ijkl} is the volume of a tetrahedron element in Fig. 5.3 and A^{ijk} is the area of triangular face associated with nodes i, j, and k.

Substitute ξ to x, y, and z of four nodes i, j, k, and l, then torsional vector Q_{ijkl} can be written as:

$$Q_{ijkl} = \left[\frac{\partial \varphi}{\partial x_i} \quad \frac{\partial \varphi}{\partial y_i} \quad \frac{\partial \varphi}{\partial z_i} \quad \frac{\partial \varphi}{\partial x_j} \quad \frac{\partial \varphi}{\partial y_j} \quad \frac{\partial \varphi}{\partial z_j} \quad \frac{\partial \varphi}{\partial x_k} \quad \frac{\partial \varphi}{\partial y_k} \quad \frac{\partial \varphi}{\partial z_k} \quad \frac{\partial \varphi}{\partial x_l} \quad \frac{\partial \varphi}{\partial y_l} \quad \frac{\partial \varphi}{\partial z_l} \right]^T \tag{5.14}$$

A torsional stiffness matrix $K_{ijkl}^{torsion}$ can be calculated as:

$$K_{ijkl}^{torsion} = \frac{1}{\sin^2 \varphi} Q_{ijkl} {Q_{ijkl}}^T \tag{5.15}$$

The stiffness matrix results in complexity in constructing a system of linear equation for force equilibrium and adding the computational time. Moreover, due to the assumption of infinitesimal displacement in calculating derivative of each directional cosine, the incremental small deformation method is required for a large deformation.

The semi-torsional spring method saves the computing time and removes infinitesimal displacement limitation using a simple semi-torsion stiffness as:[51]

$$K_{ij}^{semi-torsion} = \kappa \sum_{m=1}^{NE_{ij}} \frac{1}{\sin^2 \theta_m^{ij}} \tag{5.16}$$

where NE_{ij} is the number of elements sharing edge *i-j*, θ_m^{ij} is the facing angle defined as the angle that face the edge *i-j* on the *m*th element attached to the edge, and κ is a coefficient having the dimension of the stiffness. The stiffness matrix is added to the linear stiffness one.

5.4 Results and Discussion

In order to demonstrate the efficiency of the suggested method, volume grid deformation based on the surface motion of the fourth vibration modes of NACA0012 and AGARD 445.6 wings are implemented. NACA0012 and AGARD 445.6 wings have 714,105 and 1,604,519 tetrahedral elements comprised of 121,256 and 274,292 nodes, respectively. Fig. 5.4 and 5.5 shows deformed boundary layer grids of two wings. Different colors indicate ten deformed boundary layers. The computation time comparison in Table 5.1 and 5.2 demonstrates that the new hybrid method is about 30 times faster than semi-torsional analogy. The computation time depends mainly on the number of nodes in inviscid region determined by the number of deformed viscous layer without having negative volumes.

The new hybrid method for viscous layer works well. However, movement of grids in the inviscid region using weighted semi-torsional spring analogy fails sometimes in relatively large deformation. The best way to solve this problem for inviscid region

may be successive incremental spring analogy or smoothing method with checking negative volumes.

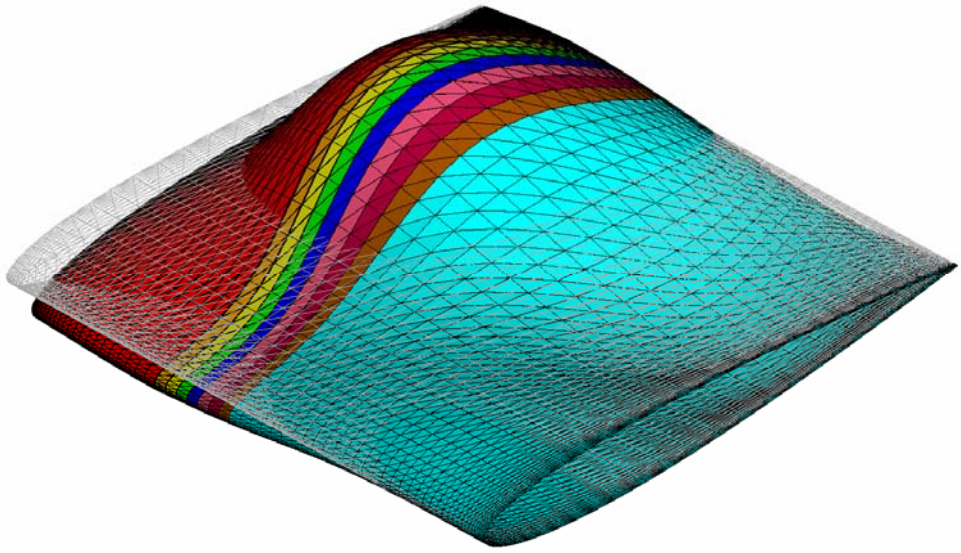

Fig. 5.4 Viscous layer deformation of NACA0012 wing

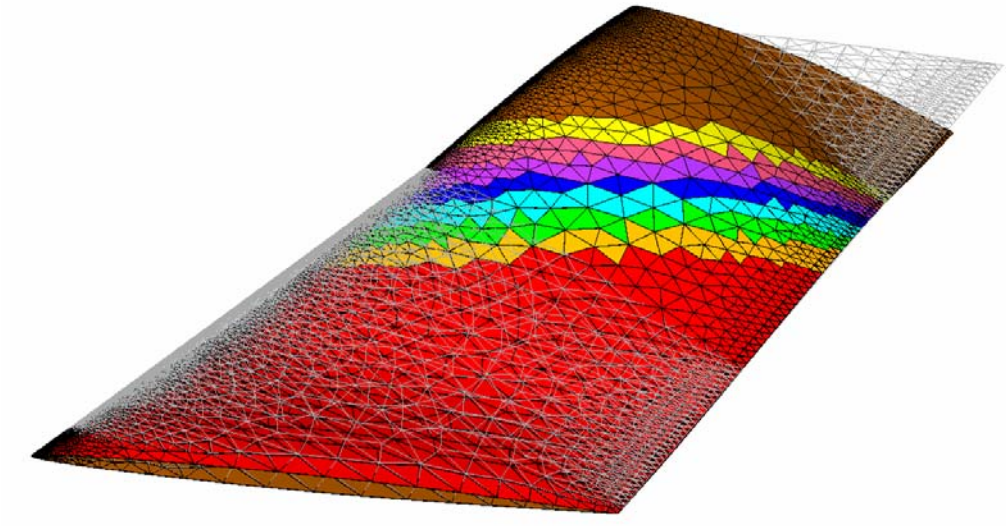

Fig. 5.5 Viscous layer deformation of AGARD 445.6 wing

Table 5.1 Comparison of relative CPU time used in NACA0012 deformation

Methods	Relative CPU time
Hybrid with LCTN (56,036)*	1
Hybrid with LCAS (79,361)	3.651
Semi-torsional (121,256)	29.15

*number of nodes in inviscid region

Table 5.2 Comparison of relative CPU time used in AGARD 445.6

Methods	Relative CPU time
Hybrid with LCTN (59,612)*	1
Hybrid with LCAS (91,814)	6.693
Semi-torsional (274,292)	N/A

*number of nodes in inviscid region

CHAPTER 6

TIME MAPPING

6.1 Introduction

Due to inherent different time integration methods used in fluid and structural analyses, time mapping algorithms are needed to synchronize computational fluid dynamics (CFD) and computational structural dynamics (CSD) solvers. There are two types of time mapping algorithms: explicit and implicit mapping. Explicit mapping can be used when structural movements or load differences are very small during one time step period. This method is easy to implement, but it would be unstable if the time step is not small enough to consider the differences of load or displacement between consecutive time steps. The main concern of this method is how to determine a time step that does not take too much CPU time and makes two different solvers stable.

The conventional serial staggered (CSS) method is one of explicit mapping methods. The roadmap of CSS is illustrated in Fig. 6.1. Most FSI application problems need finer temporal integration for the fluid than that for the structure. So that, subcycling method in the fluid solver is used for an efficient time mapping. Piperno [61-63] suggested a partitioned procedure for solving transient coupled aeroelastic problems using the subcycling staggered method in solving 1-D piston, 2-D wing airfoil, and 3-D AGARD 445.6 wing. This method, however, has only first-order time-accuracy that yields inaccurate results that would make FSI results inaccurate. To overcome the

problem, an improved serial staggered method has been suggested by Farhat and Lesoinne [60]. The method has second order and is one of the implicit coupling method that allows large time step. The procedure is illustrated in Fig. 6.2. This method was applied to the aeroelastic analyses of an entire F16 fighter [64]. Kim et al. [57] used the method with subcycling in solving FSI of an aircraft.

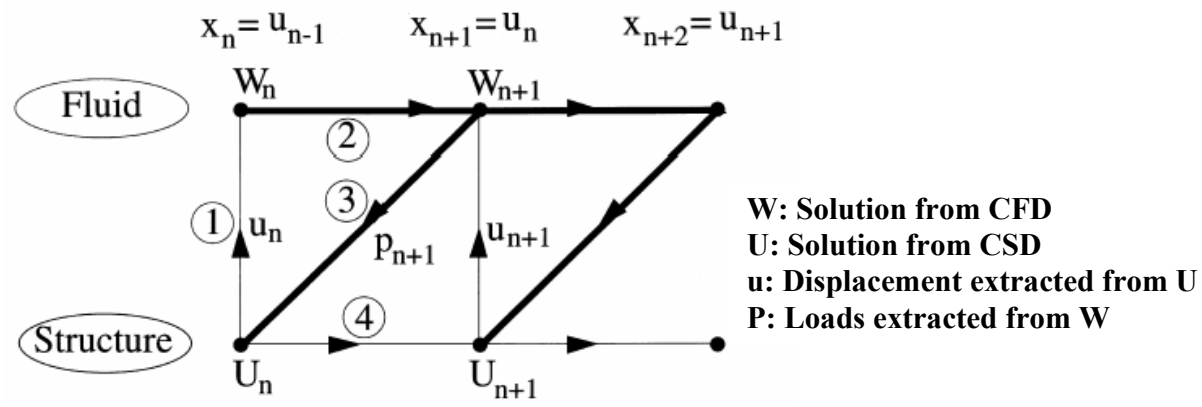

Fig. 6.1 CSS: the conventional serial staggered procedure (from Ref. [60])

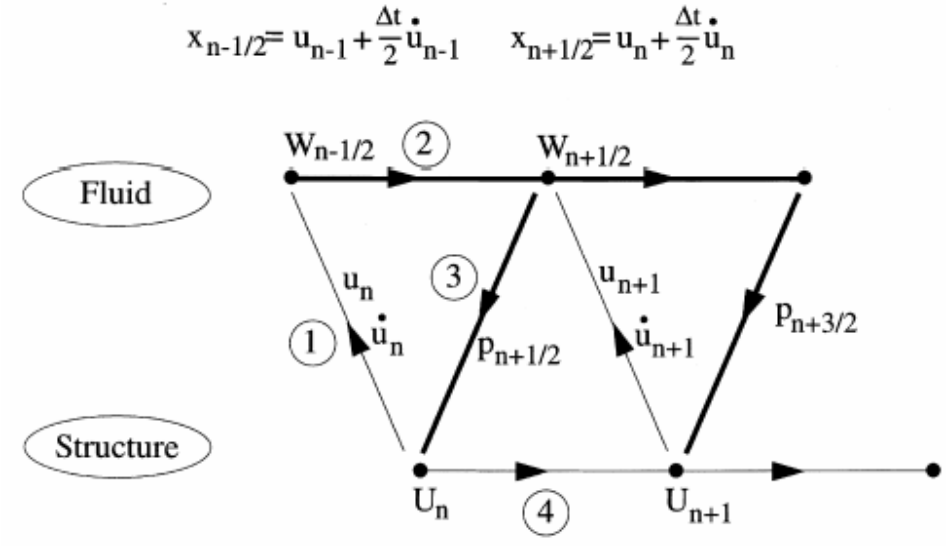

Fig. 6.2 ISS: the improved serial staggered procedure (from Ref. [60])

6.2 Conventional Serial Staggered Method

The first step of this method is to determine a reasonable FSI time step Δt for synchronizing the time step Δt_f for a CFD and Δt_s for a CSD solver that guarantee the convergence and accuracy of two solvers. In many FSI problems, fluid flow analysis needs finer temporal resolution than structural analysis. For this, the time step Δt_f can be chosen for Δt, but this takes excessive computational time to exchange data between two solvers at every time step Δt_f. In order to solve this problem, a subcycling method with a factor $n_{s/f} = \Delta t_s / \Delta t_f$ was suggested [60]. In this study, the factor $n_{s/f} = 200$ is used for a flutter analysis of a wing.

In order to perform FSI simulation with the determined time step and subcycling in fluid domain iteratively, the entire modules in FSI framework can be controlled automatically. Using Perl scripts and Dos batch commands, an example of Perl scripts used in this study is illustrated in Fig. 6.3.

```
$file4 = "Swing.key";
$file1 = "Fwing.key";
$file2 = "Fwing.cas";
$file3 = "FwingRes.cas";
for($i = 0; $i < 200 ; $i++){
        $d = $i/200 +0.05;
        $j = $i+10;
   system("Iter.bat $file1 $file2 $file3 $file4 $j $d");
}
```

Fig. 6.3 An example of Perl Script for CSS method

CHAPTER 7

APPLICATIONS

7.1 Introduction

Pulsatile flow through artificial straight/curved stenotic arteries and an in-vivo non-planar femoral artery bifurcation, and flutter of AGARD 445.6 wing are simulated to validate the FSI framework. For these applications, two commercial codes, ANSYS (ANSYS, Inc.) and FLUENT (Fluent Inc.), are used for CSD and CFD solvers, respectively.

7.2 Application I - Pulsatile Flow through Straight/Curved Carotid Stenotic Arteries

7.2.1 Introduction

This section consists of two sub-sections: 1) Straight/Curved carotid stenotic arteries; 2) Constitutive models for arteries

7.2.1.1 Straight/Curved carotid stenotic arteries

It has been well accepted that arterial stenoses may yield artery fatigue, additional adhesion of lipoproteins to wall due to the recirculation at post-stenotic regions, and abrupt plaque rupture that are main causes of heart attack and stroke. Many researchers believe that a right understanding of blood flow mechanism inside vessel could provide useful insights into vascular diseases. Many experimental studies have been carried out

over the past few decades to analyze the blood flow through straight or curved stenotic arteries. Li et al. [65] showed the reduced intraluminal pressure by stenotic amplification using in-vitro dog carotid arteries. Pulsatile flow through in-vitro asymmetric 75 % and 95 % area reduction stenotic carotid vessels were observed by Cao and Rittgers [66]. The downstream (laminar, fully turbulent, and transition flow) of an abrupt axissymmetric 75% stenosis was measured by ultra-fast magnetic resonance imaging (MRI) in Ref. [67]. Doriot [68] showed the axial wall stress due to the arterial axissymmetric stenosis might be one of the factors of development of atherosclerosis. Above studies were performed using straight rigid stenotic arteries which are not like in-vivo arteries. In order to consider the nonlinear properties of arteries which are more physiological, Ku et al. [69, 70] analyzed the fluid flow through non-rigid straight stenotic tube using non-linear materials such as Odgen and PVA hydrogel.

Computational methods have been widely employed in the area of biomechanics because of the rapid improvement of computer facilities and numerical algorithms. Mittal et al. [71] used large-eddy simulation technique for the study of turbulent flow through arterial stenosis. Mallinger [72] showed the instability of flow at the poststenotic region although the pulsatile flow is simulated in three-dimensional axissymmetric stenotic artery. Lee et al. [73] analyzed the turbulent flow through series stenoses using two-dimensional κ-ω turbulent model. Varghese and Frankel [74] compared κ-ω turbulent model with κ-ε turbulent one and showed the former model is better in low Reynolds number. Ryval et al. [75] suggested two simple equations for analyzing turbulent blood flow. Tang et al. [15] made an experiment on the steady flow through asymmetric/axis-symmetric stenosis silicon tube and simulated the flow with ADINA

that used directly-coupled method. The Ogden material used and their stress-strain curve were determined from experimental data. They simulated the steady flow through thick-wall tube whose mechanical properties is similar to bovine carotid considering important pre-stretched and pre-stressed effects [14]. With same thick-wall tube, they simulated pulsatile flow and showed artery collapse due to the negative pressure resulting from recirculation at the post-stenotic regions [16].

While many researchers have studied the flow through straight stenotic tubes, the flow in curved stenotic tubes was studied by only a few researchers. Yao et al. [76] simulated stead flow in curved arteries with elliptic stenosis changing two parameters such as angles of curvature and degrees of stenosis. Their results indicated that the parameters must be considered for measuring the severity of stenosis.

In this study, a three-dimensional model of pulsatile flow through a simplified curved stenotic artery is presented and simulated using FSI framework to take into account the interaction between the flow and artery wall. A finite element code, ANSYS, is used for CSM analysis. A material constitutive model, hyperelastic Mooney-Rivlin model, is used for simulating realistic structural behavior of artery wall, which is initially pre-stretched and pre-pressurized for considering residual strain that influences the stress distribution of the wall [77]. The blood flow is analyzed as an unsteady laminar flow with full Navier–Stokes equations with convective terms. For time mapping algorithm, a serial staggered method is used. The results show the phase lag, pressure difference, and wall shear stress of the curved stenotic artery. The results are compared with those of straight artery.

7.2.1.2 Constitutive models for arteries

It is well known that large compliant arteries have highly nonlinear, visco, and hyper elasticity with anisotropic mechanical behaviors. To analyze the effect of pulsatile blood pressure on stenosis and plaque on arteries or assess the mechanical properties in the deployment of stent in an analytical/computational way, representative mathematical models of the large arteries are essential. Strain energy density functions (SEDF), one of the mathematical models, have been commonly used because constitutive stress-strain relations are easily derived directly from the SEDF. Earlier researchers developed many constitutive models. Among their works, Fung et al. [78]; Chuong and Fung's exponential [79], Takamizawa and Hayashi's logarithmic [80] and Vaishnav et al.'s polynominal [81] are predominantly basis functions of many recent newest constitutive models. Humphrey [82] compared their SEDFs and showed that the exponential form provided best fit for certain arteries, although it needed some alternations for muscular arteries.

Those three SEDF forms were obtained by oversimplifying parameters such as limited transmural pressure range, axis-symmetric, only circumferential stress-strain, and etc. To identify realistic physiological properties of typical individual arteries, mixed and modified SEDFs have been developed. Holzapfel et al. [83] developed the combined SEDFs using neo-Hookean SEDF for isotropic and exponential SEDF for anisotropic layer (collagen fiber) to consider residual stress [84] and anisotropic properties. This SEDF is modified with wavy nature of the collagen and fraction of both elastin and collagen contained in the media by Zulliger et al. [85]. Other modified ones can be found in Vito and Dixon [86].

The above SEDFs do not consider viscoelastic properties that Gow and Taylor [87]; Anliker et al. [88] pointed out important structural properties of arteries. The fact that viscoelasticity especially in the hypertensive arteries becomes increased has been reported in many studies [89-92].

Viscoelastic constitutive models were developed considering symmetric and principal strain direction coincided with base vectors in cylindrical coordinates in the earlier studies [93-95]. Demiray [96] proposed quasi-linear constitutive model for determining viscoelastic coefficients using the solution of a torsional wave in a pre-stressed thin tube. Holzapfel et al. [97] proposed three dimensional generalized Maxwell model including SEDF developed by Holzapfel et al. [83] for a viscoelastic structural model of healthy young arterial walls in the passive state of the smooth muscles.

Assuming that users can use only already-built-in CSD solvers without source program, the implementation of constitutive models is not possible. For this reason, most applications with arteries using the CSD solvers take a built-in constitutive model such as Mooney-Livlin [17, 98, 99] instead of specific constitutive model. However, some advanced CSD solvers such as ANSYS and ABAQUS have the interface tool that have still limitation to the constitutive models without taking viscoelasticity into account though. Using usermat function in ANSYS, Zhang [28] implemented two-dimensional orthotropic exponential pseudo-elastic, and incompressible model. Holzapfel et al. [97] simulated balloon angioplasty with layer-specific three dimensional constitutive model using the UEL programming interface in ABAQUS.

7.2.2 Geometry and grid

The straight artery geometry is shown in Fig. 7.1. The radius $R(z)$ of the inner wall of the artery is defined as:

$$R(z) = R_0 - \begin{cases} S_0 R_0 [1 - \cos(2\pi(z - z_1)/(z_2 - z_1))]/2, & z_1 \le z \le z_2 \\ 0, & \text{otherwise} \end{cases} \tag{7.1}$$

where R_0 is the radius of the non-stenotic part of the artery inner wall, S_0 is the stenosis severity by diameter , which is usually calculated from

$$S_0 = \frac{R_0 - R_{\min}}{R_0} \tag{7.2}$$

and z_1 and z_2 are the beginning and ending positions of the stenosis.

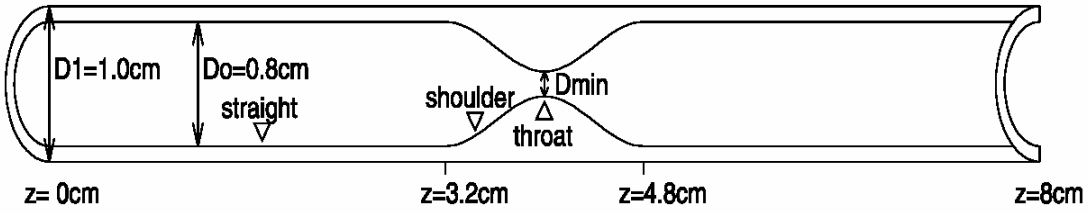

Fig. 7.1 Geometry of stenotic artery (from Ref. [16])

Because the available displacement experimental data is measured with 80% stenosis severity in Ref. [16], the severity is applied in this study to compare the results.

Using the HyperMesh grid generator, structural grid of the artery and fluid grid of blood inside artery are made. The structural grid comprises 3220 nodes and 13667 tetrahedral elements and the fluid grid has 18769 nodes and 101885 tetrahedral elements as shown in Fig. 7.2. The finer grids are generated at the throat and shoulder to more accurate results. To make pre-stretched (36.5%) and curved geometry, ANSYS is used.

The degree of freedom is constrained in x direction at the center of the straight artery and displacement at the both ends of the artery are imposed as shown in Fig. 7.3.

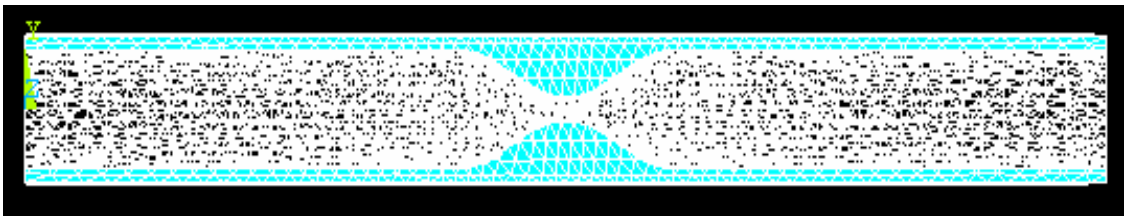

a) Structural grid

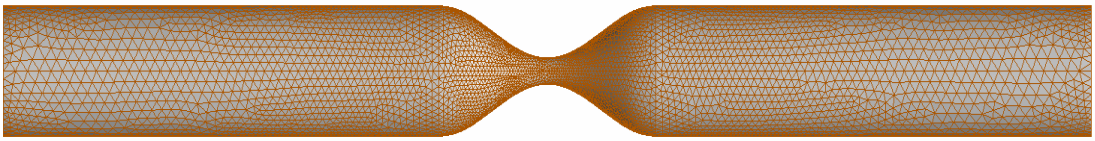

b) Fluid grid

Fig. 7.2 Structural and fluid grids of stenotic artery

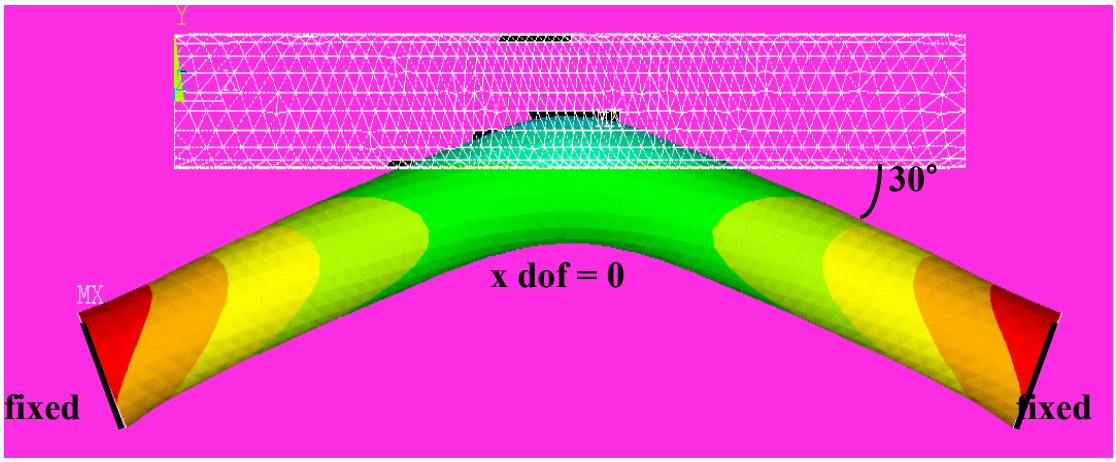

Fig. 7.3 Geometry of curved stenotic artery from straight one

7.2.3 Parameters and boundary conditions

7.2.3.1 Structure

The material of the artery is polyvinyl alcohol (PVA) hydrogel. The PVA hydrogel is homogenous, hyperelastic, nonlinear, and nearly incompressible material. Young's modulus of the material is 2×10^5 Pa and Poisson's ratio is 0.4999 which is as close to 0.5 as possible. Hyperelastic Mooney-Rivlin model is chosen to describe the material. This model is selected because of the excellent fit to experimental data as shown in Fig. 7.5 and availability in ANSYS. Given the principal stretch ratios at any deformation state of a material point as λ_1, λ_2, and λ_3, the strain invariants are defined as:

$$I_1 = \lambda_1^{\,2} + \lambda_2^{\,2} + \lambda_3^{\,2} \tag{7.3}$$

$$I_2 = \lambda_1^{\,2}\lambda_2^{\,2} + \lambda_2^{\,2}\lambda_3^{\,2} + \lambda_3^{\,2}\lambda_1^{\,2} \tag{7.4}$$

and, the ratio of the deformed elastic volume over the undeformed volume of the material J can be calculated as:

$$J = \lambda_1\lambda_2\lambda_3 \tag{7.5}$$

The deviatoric strain invariants are written as:

$$\overline{I_1} = \frac{I_1}{J^{1/3}} \qquad \overline{I_2} = \frac{I_2}{J^{1/3}} \tag{7.6}$$

The strain energy potential W for five parameters C_{ij}'s Mooney-Rivlin model is

$$W = \sum_{i+j=1}^{2} C_{ij} (\overline{I_1} - 3)^i (\overline{I_2} - 3)^j + \frac{\kappa}{2} (J-1)^2 \tag{7.7}$$

where, κ is bulk modulus. The parameters in Table 7.1 are determined using curve fitting tools in ANSYS with 18 experimental data as shown in Fig. 7.4. Fig. 7.5 shows that the constitutive model with the five parameters from ANSYS agrees with the experimental data.

Table 7.1 Five parameters for Mooney-Rivlin model of PVA hydrogel

Parameters	Values(MPa)
C_{10}	0.00483831337749
C_{01}	0.0157456261132
C_{20}	0.0630274350665
C_{11}	-0.06934258113
C_{02}	0.0214277129574

To simulate physiological conditions of blood vessel, the artery is pre-stretched and pre-stressed. The displacement 2.92 cm in the axial direction is first imposed and curved as shown in Fig. 7.3. Next, the flow in the pre-stretched artery is analyzed with flow initial boundary condition to obtain the pressure on inner wall. The pressure is transferred to structural artery to impose pre-stress. The residual strain from the pre-stretched and pre-stressed plays an important role in wall stress distribution.

7.2.3.2 Fluid

The flow is assumed to laminar, Newtonian, viscous and incompressible. Navier-Stokes equation is chosen for analyzing the flow in FLUENT. The viscosity of blood is

0.004 kg/m-s and the density is 1055 kg/m^3. The cosine function $IP(t)$ for the pressure at inlet of the artery is used to make the flow pulsatile flow.

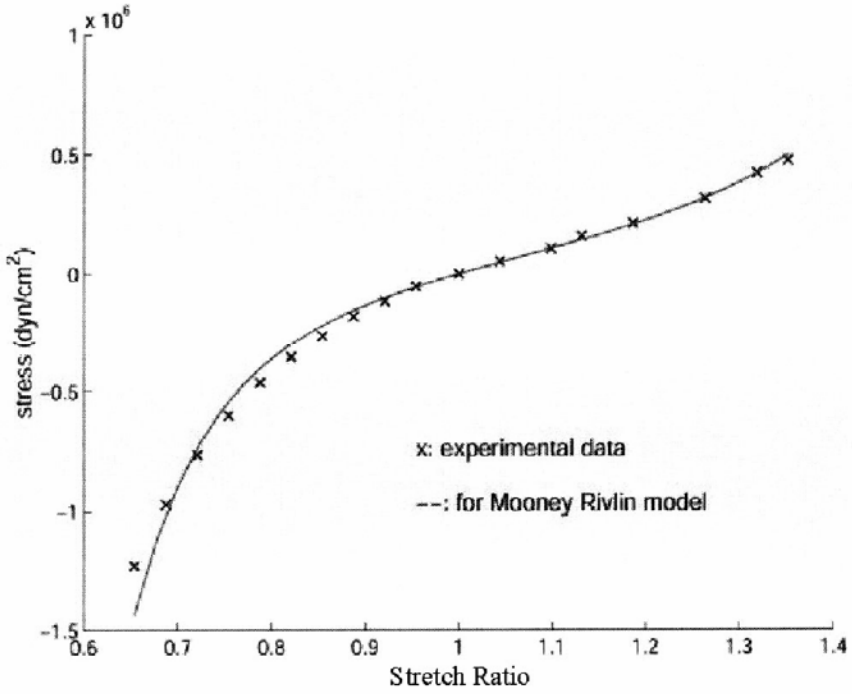

Fig. 7.4 Stress –strain curve of PVA hydrogel (from Ref. [16])

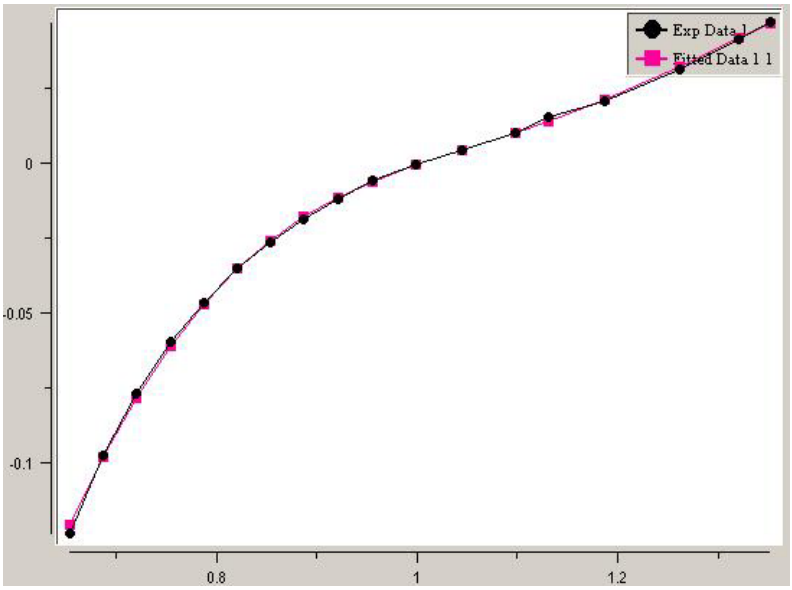

Fig. 7.5 Strain Vs. stress(y, MPa) of PVA hydrogel fitted using ANSYS

$$IP(t) = 30 * (\cos(2\pi * (t + 0.75)) + 1.0) + 70 \quad (7.8)$$

$IP(t)$ depicts approximately the experimental data as shown in Fig. 7.6. In the Fig. 7.6, the time is shifted by 0.27 sec to fit maximum value of $IP(t)$ to experimental maximum one. If curve fitting to experimental data were used, the accurate corresponding function could be obtained. In order to set the pulsatile flow condition in FLUENT, a user defined function (UDF) is used. The UDF is written by C language as followings:

```
#include "udf.h"
DEFINE_PROFILE(unsteady_pressure, thread, position)
{
  float t, pressure;
  const double pi = 3.1415926535897931;
  face_t f;

  t = RP_Get_Real("flow-time");

  pressure = (30.0*(cos(4.0*pi*(t+0.75)/2.0)+1.0)+70.0)*133.3;

  begin_f_loop(f, thread)
  {
   F_PROFILE(f, thread, position) = pressure;
  }
  end_f_loop(f, thread)
}
```

The UDF is complied and embedded in FLUENT.

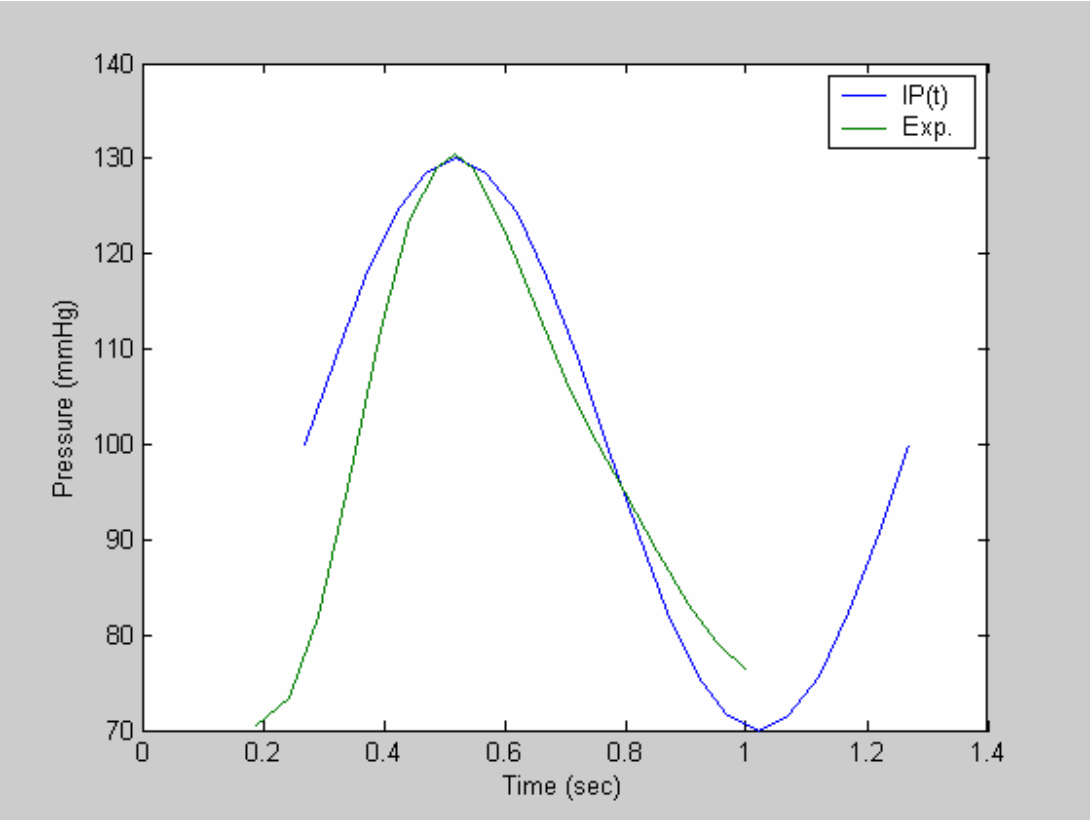

Fig. 7.6 Experimental and numerical inlet pressure for stenotic arteries

7.2.4 Time mapping

After simulating the ANSYS and FLUENT with initial and boundary condition, time step is determined as 0.05 and 0005 for solid and fluid, respectively. 20 iterations of FSI are implemented for one period using CSS method and subcycling method with Perl script and Dos batch command as shown in Fig. 7.7,. The auto-time step option in ANSYS is turned on to reduce CPU time and prevent divergence of solution.

```
$file4 = "STube.key";
$file1 = "FTube.key";
$file2 = "FTube.cas";
$file3 = "FTubeRes.cas";
for($i = 0; $i < 20 ; $i++){
        $d = $i/20 +0.05;
        $j = $i+3;
   system("Iter.bat $file1 $file2 $file3 $file4 $j $d");
}
```

Fig. 7.7 Perl Script for CSS method

7.2.5 Results

7.2.5.1 Straight stenotic artery

For validating the FSI framework, the displacement of the artery in the radial direction is compared with those of the artery from Ref. [16] in Fig. 7.8. The maximum displacement value 1.7679 mm in radial direction at cross section z = 2.0 cm occurs at 0.325 sec (the time is shifted by 0.27). The maximum displacement does not agree with experimental one (1.2655mm). The error may result from different boundary conditions, and material properties. In ANSYS, uniaxial, biaxial, or volumetric strain-versus-stress information for Mooney-Rivlin model is needed, However, Ref. [16] only has an area strain-stress curve. This may cause the error in terms of material properties. The 0.075 second phase delay well agrees with experimental one as illustrated in Fig. 7.9 [100]. The delay was not detected by Tang's numerical simulation [16]. The time-dependent velocity magnitude distribution on the cutting plane is illustrated on Fig. 7.10. The maximum velocity is 5.2 m/s. The wall shear stress magnitude due to the dynamic pressure is shown in Fig. 7.11. The maximum wall shear stress is 604 Pa. The Von-Mises stress distribution

is shown in Fig. 7.12. The maximum stress is 328,199 Pa when the maximum displacement occurs.

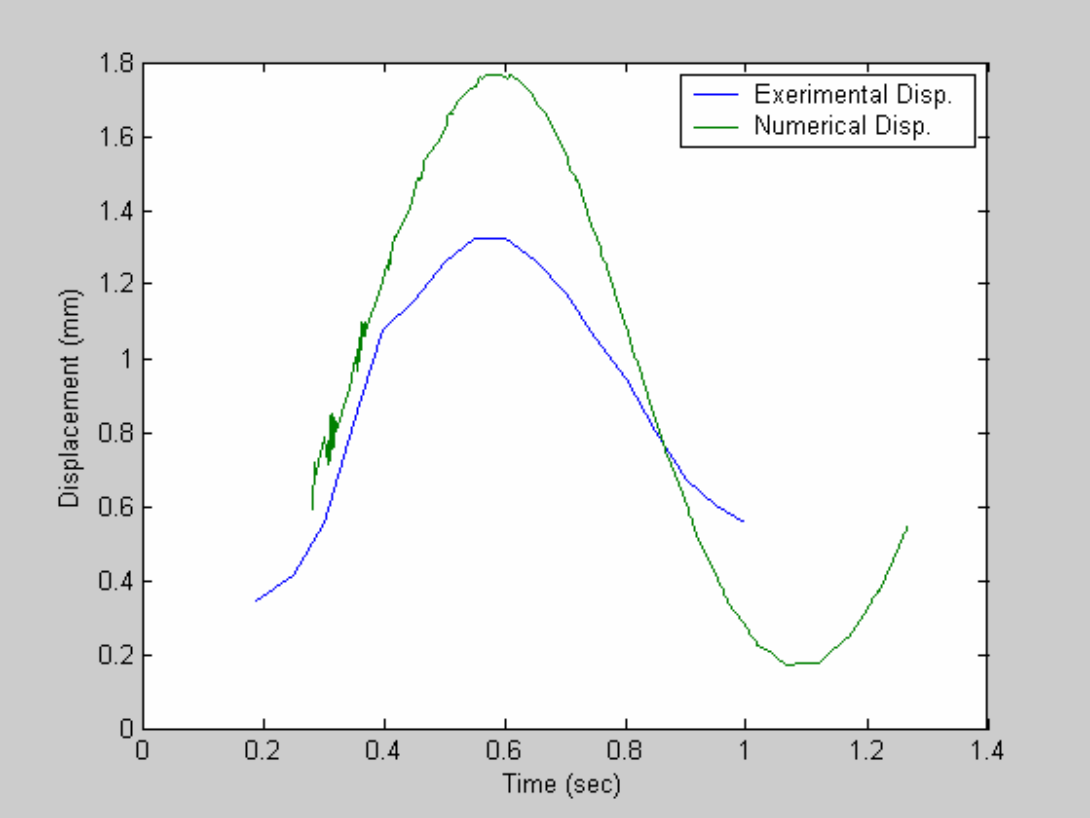

Fig. 7.8 Experimental and numerical displacement of straight stenotic artery

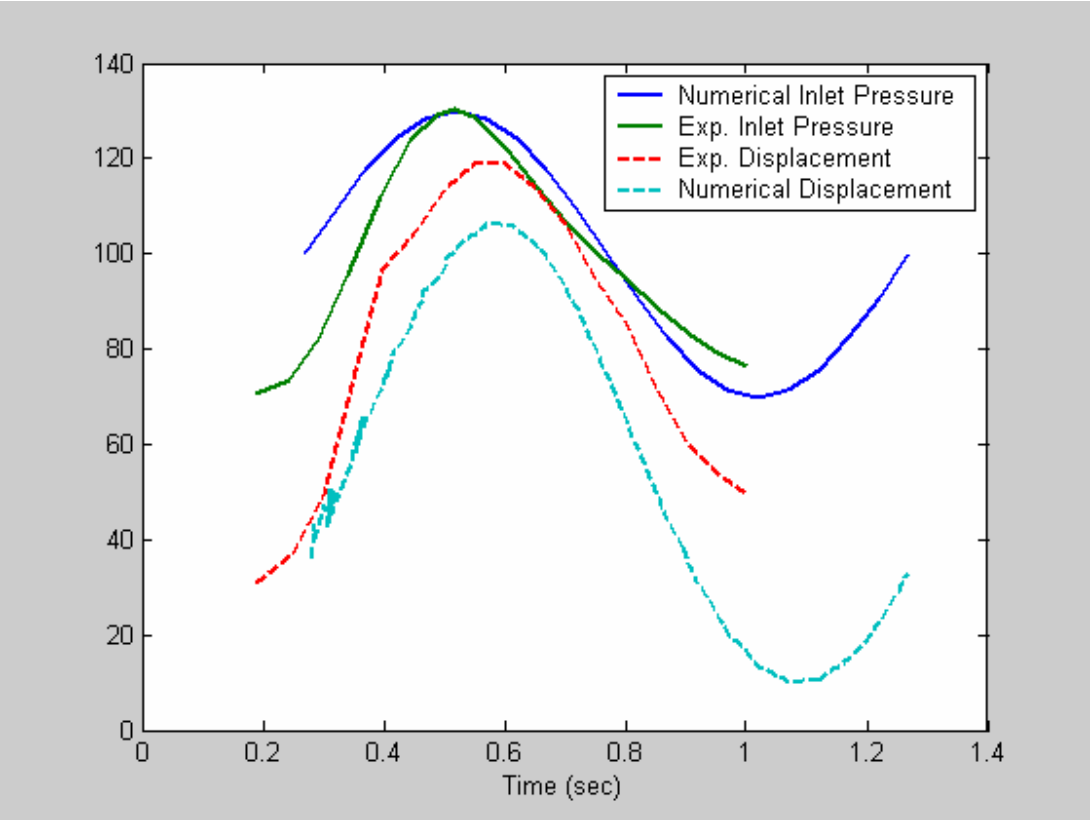

Fig. 7.9 Experimental and numerical displacement with inlet pressures of a straight stenotic artery

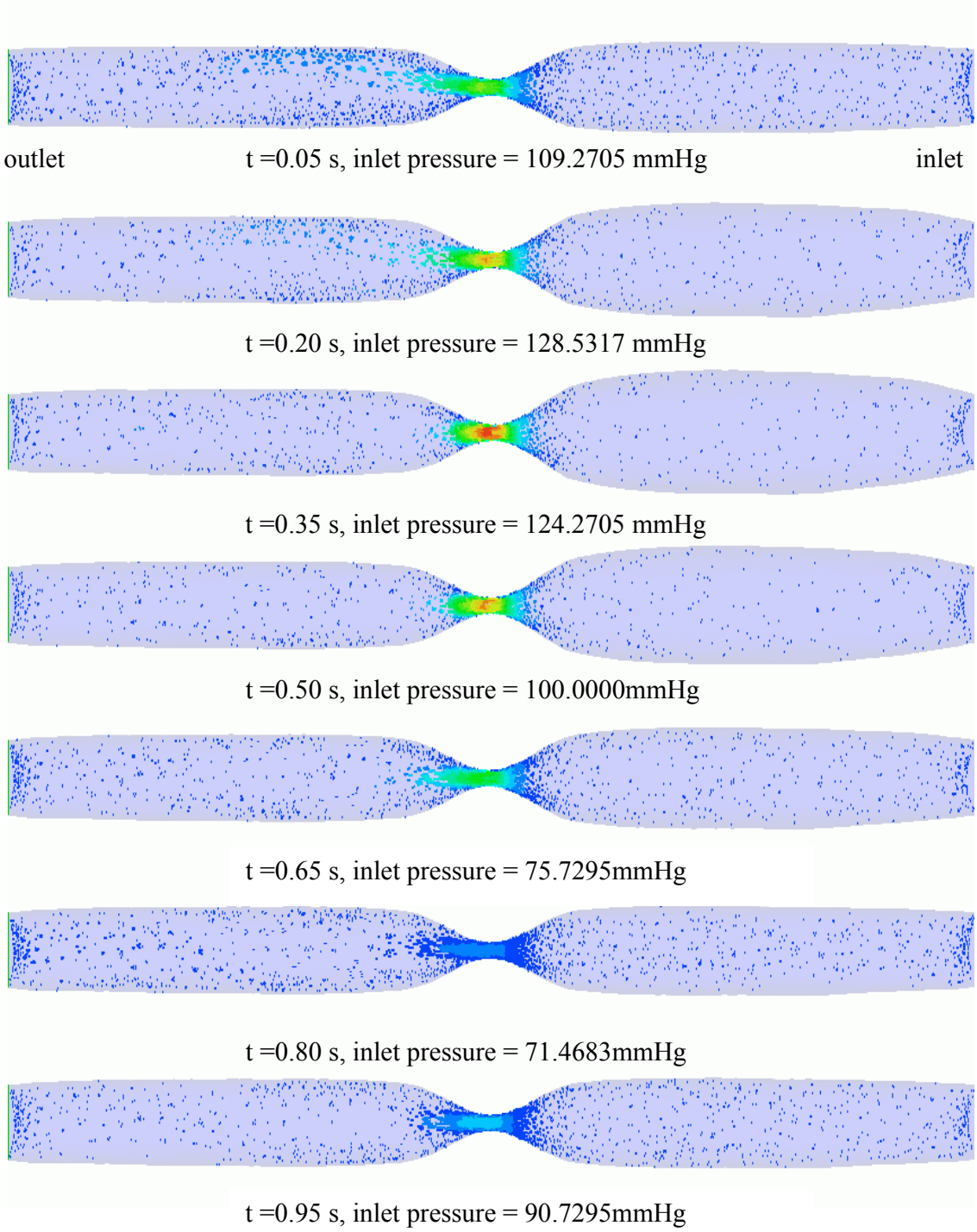

Fig. 7.10 Velocity magnitude distribution in varying time and pressures a straight stenotic artery

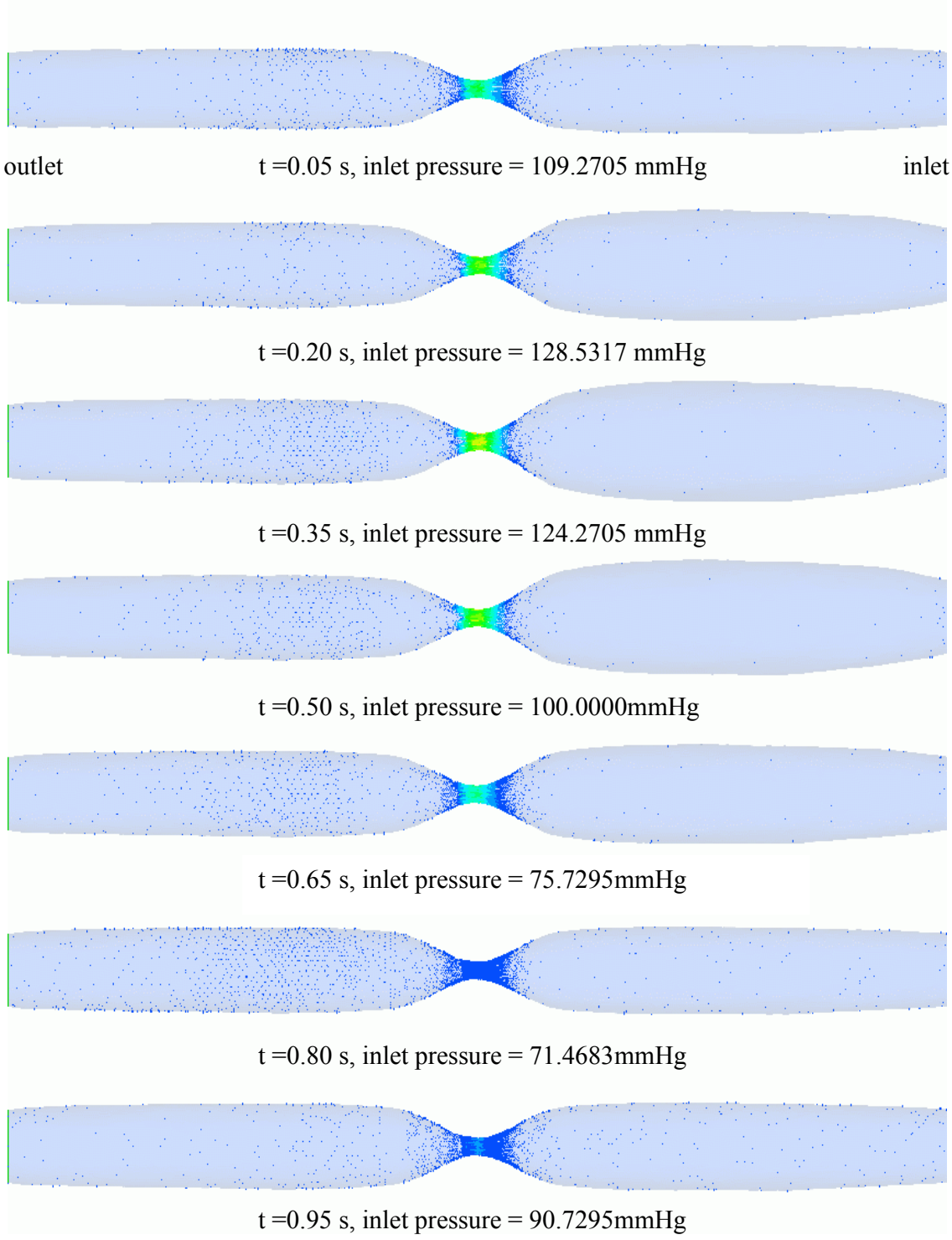

Fig. 7.11 Wall shear stress distribution in varying time and pressures a straight stenotic artery

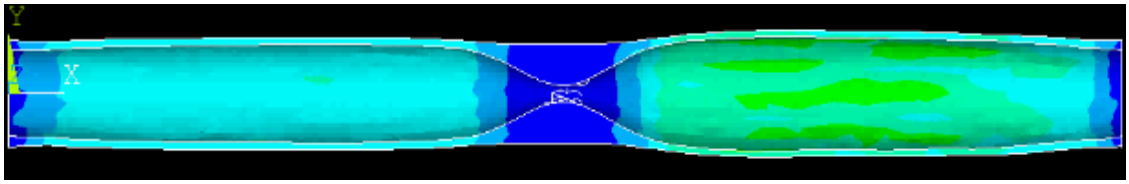

outlet t =0.05 s, inlet pressure = 109.2705 mmHg inlet

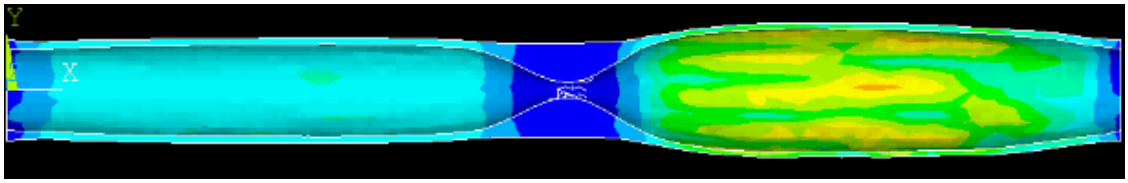

t =0.20 s, inlet pressure = 128.5317 mmHg

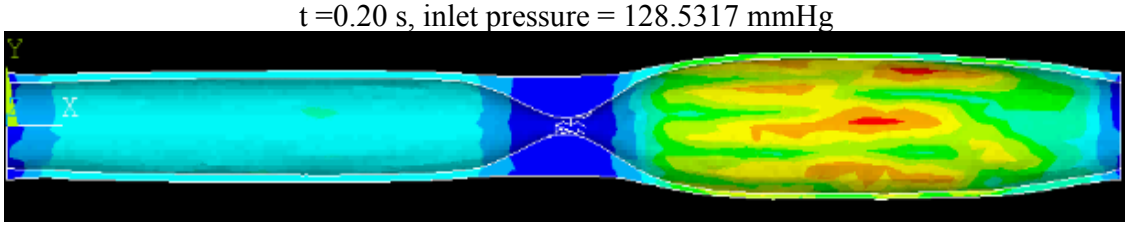

t =0.35 s, inlet pressure = 124.2705 mmHg

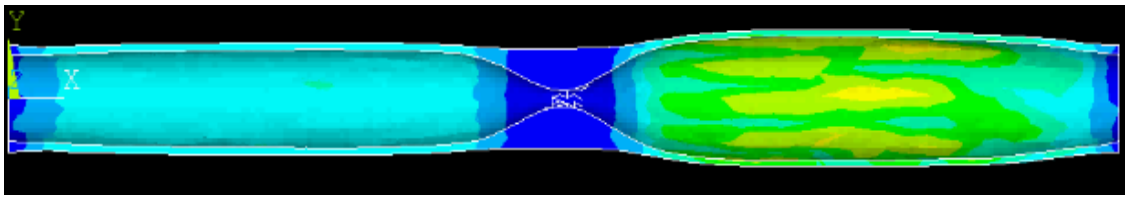

t =0.50 s, inlet pressure = 100.0000mmHg

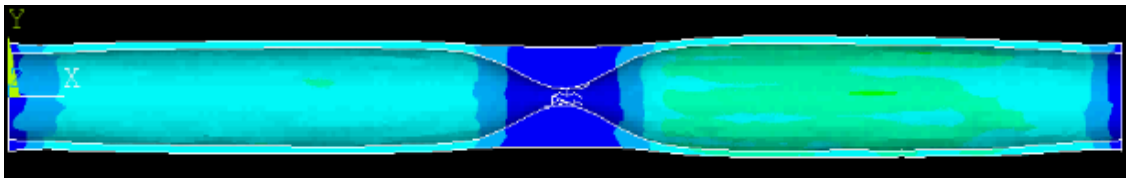

t =0.65 s, inlet pressure = 75.7295mmHg

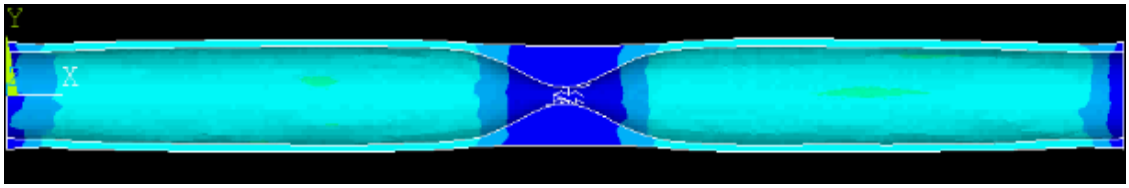

t =0.80 s, inlet pressure = 71.4683mmHg

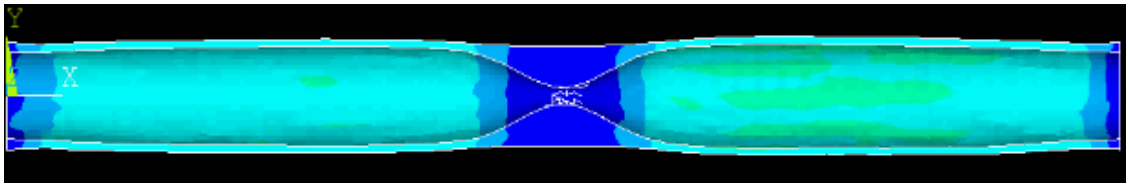

t =0.95 s, inlet pressure = 90.7295mmHg

Fig. 7.12 Von-Mises stress distribution in varying time and pressures

7.2.5.2 Curved stenotic artery

The initial displacement of curved stenotic artery is about 1.25 mm, which is greater than that of straight one by the amount of 0.65mm. To compare the displacements of two arteries, displacement of straight and curved artery is plotted as shown in Fig. 7.13. The straight one keeps the periodic displacement, but the curved one dose not. The realistic periodic simulation must be considered to investigate this problem.

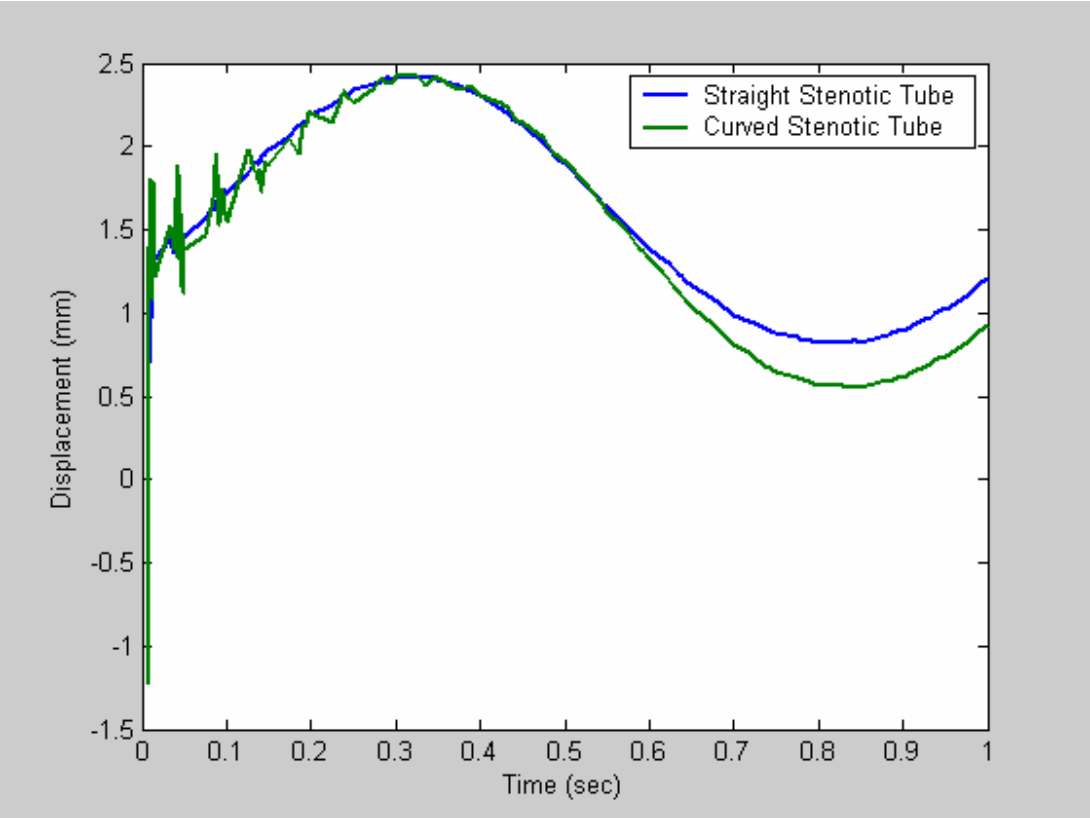

Fig. 7.13 Displacement of straight and curved stenotic artery

The velocity magnitude distribution on the cutting plane is illustrated on Fig. 38. The maximum velocity is 5.02 m/s, which is lower than 5.2m/s in the straight artery. The wall shear stress magnitude due to the dynamic pressure is shown in Fig. 7.14. The

maximum wall shear stress is 570 Pa, which is lower than 604 Pa in the straight artery. The Von-Mises stress distribution is shown in Fig. 7.15. The maximum stress is 320,848 Pa when the maximum displacement occurs.

Severe recirculation at the poststenotic region is shown in Fig. 7.16 when inlet pressure is 75.7295 mmHg. The recirculation may be one of causes of the development of atherosclerosis.

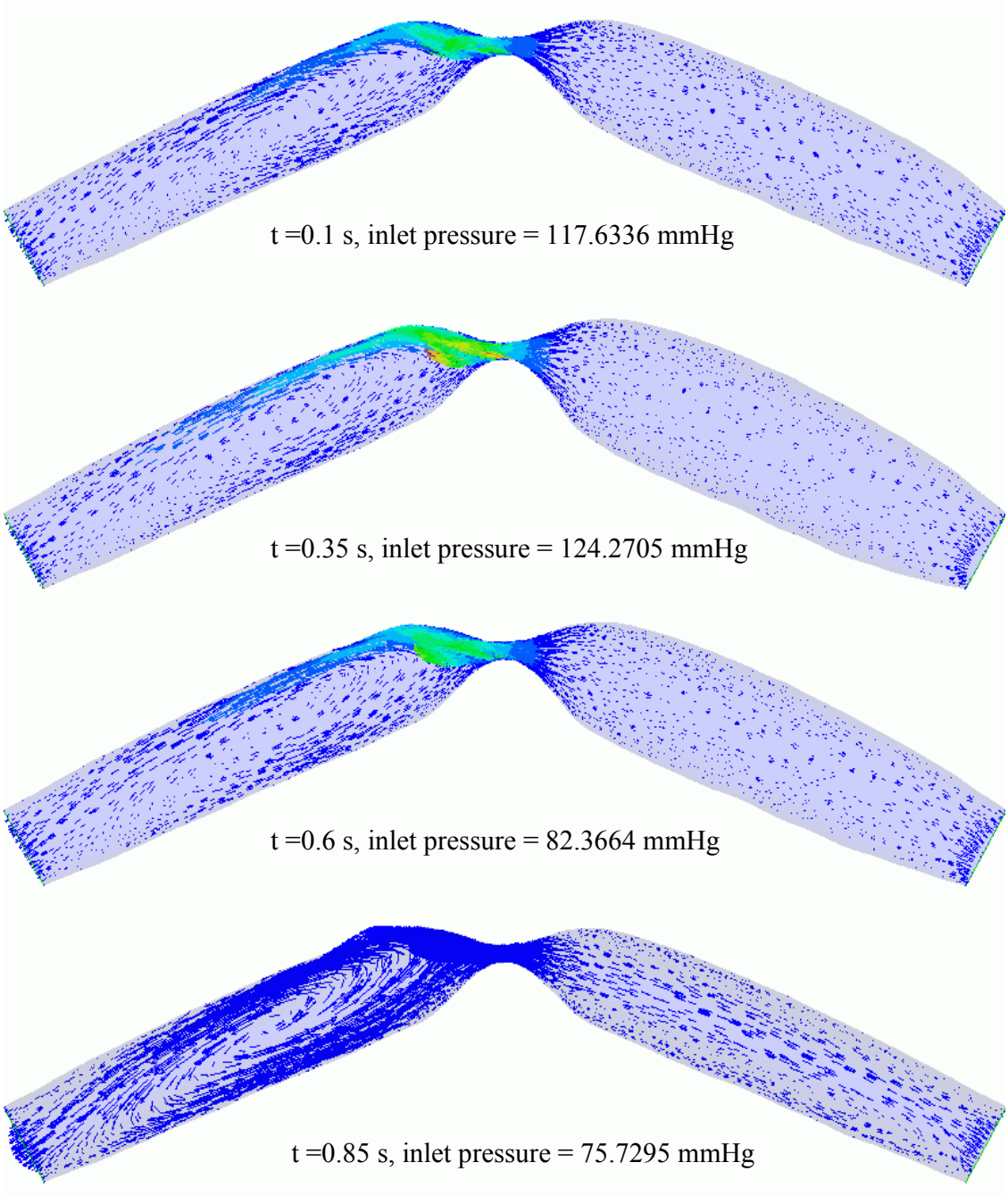

Fig. 7.14 Velocity magnitude distribution in varying time and pressures of a curved stenotic artery

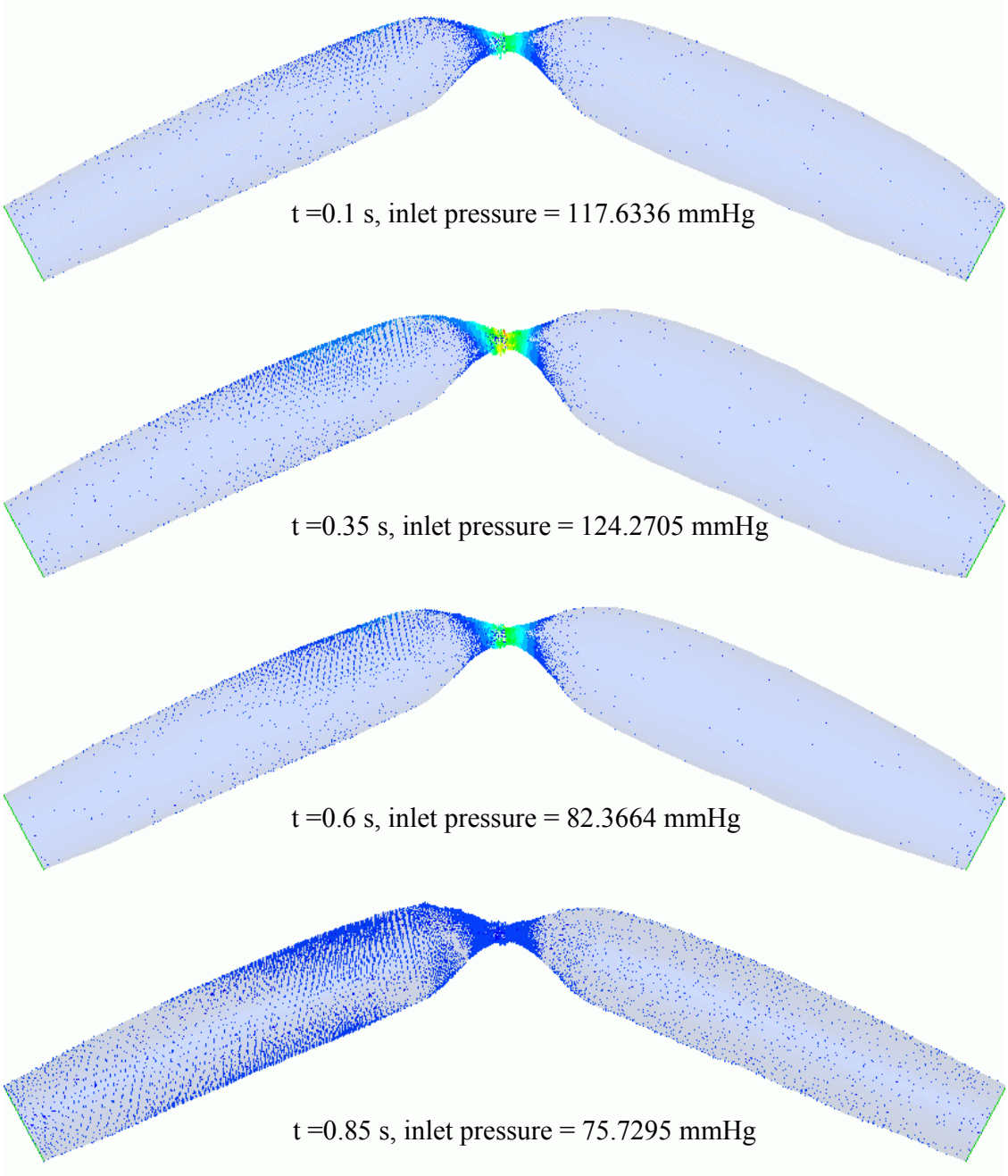

Fig. 7.15 Wall shear stress distribution in varying time and pressures of a curved stenotic artery

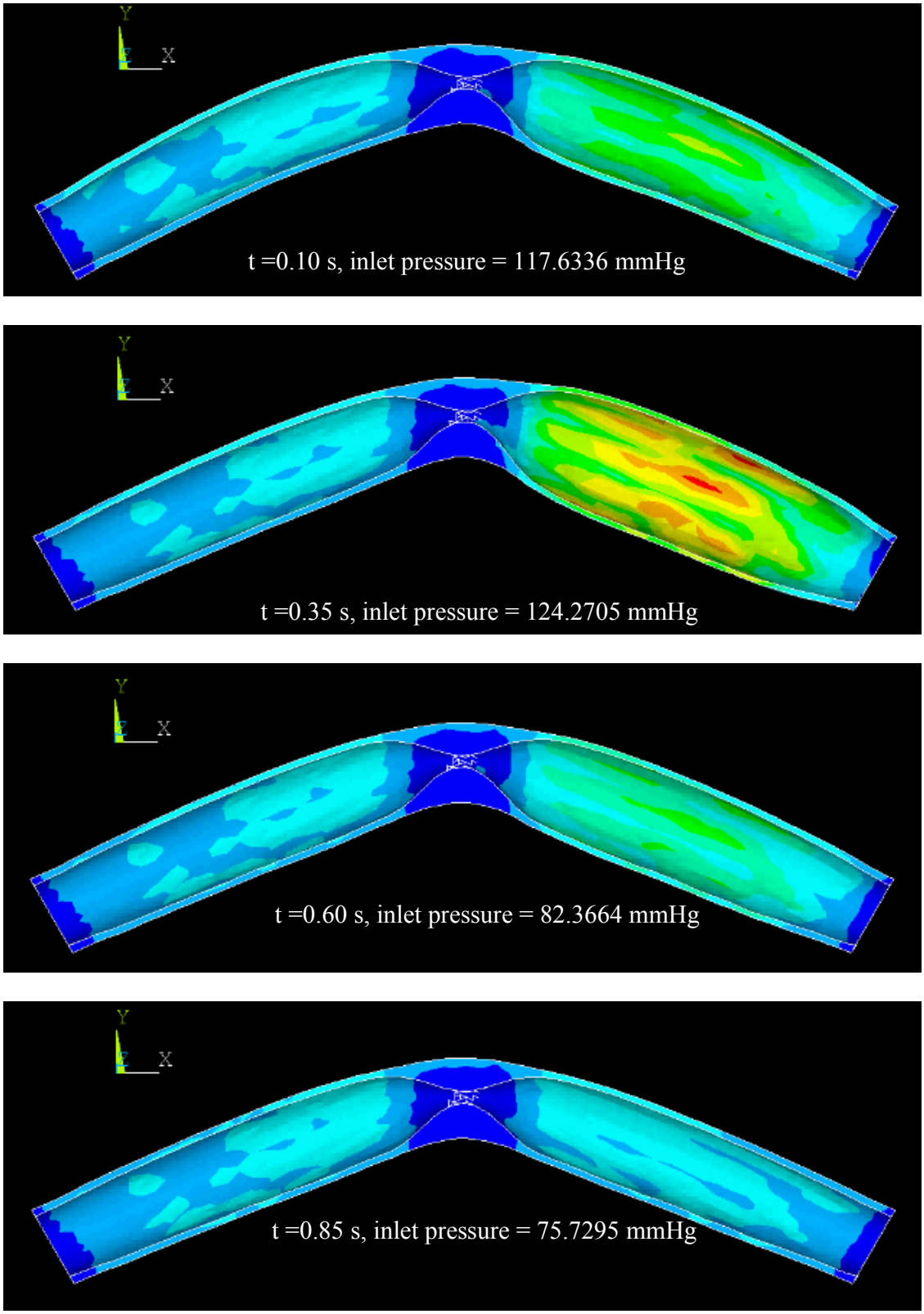

Fig. 7.16 Von-Mises stress distribution in varying time and pressures

7.3 Application II - Hemodynamics of the In-Vivo Common Femoral Artery Bifurcation

7.3.1 Introduction

Peripheral arterial disease (PAD) is prevalent in 12-20 percent of Americans age 65 and older [101]. Especially, almost one in four people screened annually through a nation wide screen programming are identified to have moderate or high risk of lower extremity PAD [102]. Lower limb PAD develops most commonly as a result of atherosclerosis. The atherosclerosis may result from consequent reduction of blood flow, and in turn it may affect the accumulation of plaque or genesis of atheroma simultaneously on the vessel wall.

It has been well demonstrated that wall shear stress (WSS) calculated from velocity near the wall, which is strongly related to interactions between pulsatile flow and compliance of blood vessel or/and vascular geometry such as bifurcation, high curvature, junction, graft and stenosis, is a leading factor of the development and process of atherosclerosis on the femoral [103-106] and the other ateries [107-110] in many experimental ways. The WSS comparative studies of femoral and carotid arteries can be found in Refs. [111-113].

Many hemodynamic factors relating WSS implicated in atherogenesis have been overviewed well in Ref. [114]. Therefore, accurate WSS calculation may be a leading factor in diagnose onset and progress of atherosclerosis. In the patient-specific diagnosis of the diseased artery, however, due to the inherent complex features of patient-specific arteries, the findings from previous works to obtain the hemodynamic factors may not be applicable to the patient. Nowadays, the MRI and Doppler Ultrasound (DUS) [115-118] are commonly used as in-vivo diagnostic tools. However, the DUS is not suitable for

analyzing velocity in femoral artery bifurcation which is not obviously circular [119]. Then, the MRI may be the best choice for making diagnosis patient artery disease. Current velocity measurement from MRI, however, in especially bifurcation of diseased femoral artery does not provide accurate data due to the non-circular geometry and low flow downstream which cause to signal-to-noise ratio (SNR) [120, 121].

Because of improvement of computer facilities and accurate and robust numerical algorithms over two decades, computational fluid dynamics (CFD) has been employed and proven in calculating WSS in many simplified, averaged, and physiologically equivalent arteries [122-128]. Recent advances in computational reconstruction techniques and/or quantification of velocity profile from MRI and computerized tomography (CT) make the CFD method powerful tools in analyzing the blood flow characteristics such as secondary flow, circulated flow and vortices of realistic patient-specific arteries in accurate and relatively cost-effective ways [129-137]

The combination of three-dimensional reconstructed from MRI and/or CT images for the patient-specific geometry with/without disease and realistic velocity profile for boundary condition can help interpreting in-vivo data especially around lumen of artery and in turn contributing to the findings of right MRI extraction from images. As mentioned before, the compliance of wall is an important factor of hemodynamics. It is well proven in many studies that the consideration of compliance of the wall with pulsatile flow is required for capturing biofidelic and realistic hemodynamic properties [138-147].

To my knowledge, the studies for patient-specific femoral artery bifurcation have not been done yet with considering compliance of wall and pulsatile flow simultaneously.

In this study, a realistic three-dimensional model of pulsatile blood flow through image-based common femoral artery bifurcation using a loosely-coupled FSI framework is simulated to obtain accurate WSS by taking into account the interaction between the blood flow and arterial wall motion.

7.3.2 Geometry and grid

A biofidelic femoral artery bifurcation about 4 cm in length of 55 year old female volunteer suffering from paraplegia has been reconstructed by ETLab [148] using 40 slices of total 992 CT scan images from the abdomen to the toes using GE LightSpeed Pro Scanner with 1.25mm slice thickness including 0.25mm overlap. The image resolution was 512x512 pixels, each pixel representing 0.7929x0.7929mm^2 area. Image segmentation and geometry extraction from the images were achieved using open source libraries (Insight Segmentation and Registration Toolkit, ITK, and Visualization Toolkit, VTK). Two methods, a direct advancing front method and a modified decimation method, were developed to create high-quality surface meshes. An advancing front-based meshing method was employed for three-dimensional volume meshing [149]. These images do not have enough resolution to detect wall thickness due to the high SNR. The 0.74mm wall thickness of common femoral artery (CFA) is adopted from [150]. The 4.122 averaged ratio of radius-to-thickness of CFA is used for determining the thickness of superficial, profunda, and lateral circumflex artery (SFA, PFA, and LCA). Reconstructed patient-specific femoral artery bifurcation is shown in Fig.7.17. The flow domain and artery structure is arranged simultaneously to show the inherent different resolution between two grids which is essential in loosely-coupled method. The flow domain has 367,315 tetrahedral and 18,695 triangular elements for flow analysis and common interface

respectively. The fine mesh is employed in the near-wall region to calculate WSS. The structural artery has 43,774 tetrahedral and 4,761 triangular elements for structural analysis and common interface to save the CPU time in structural analysis.

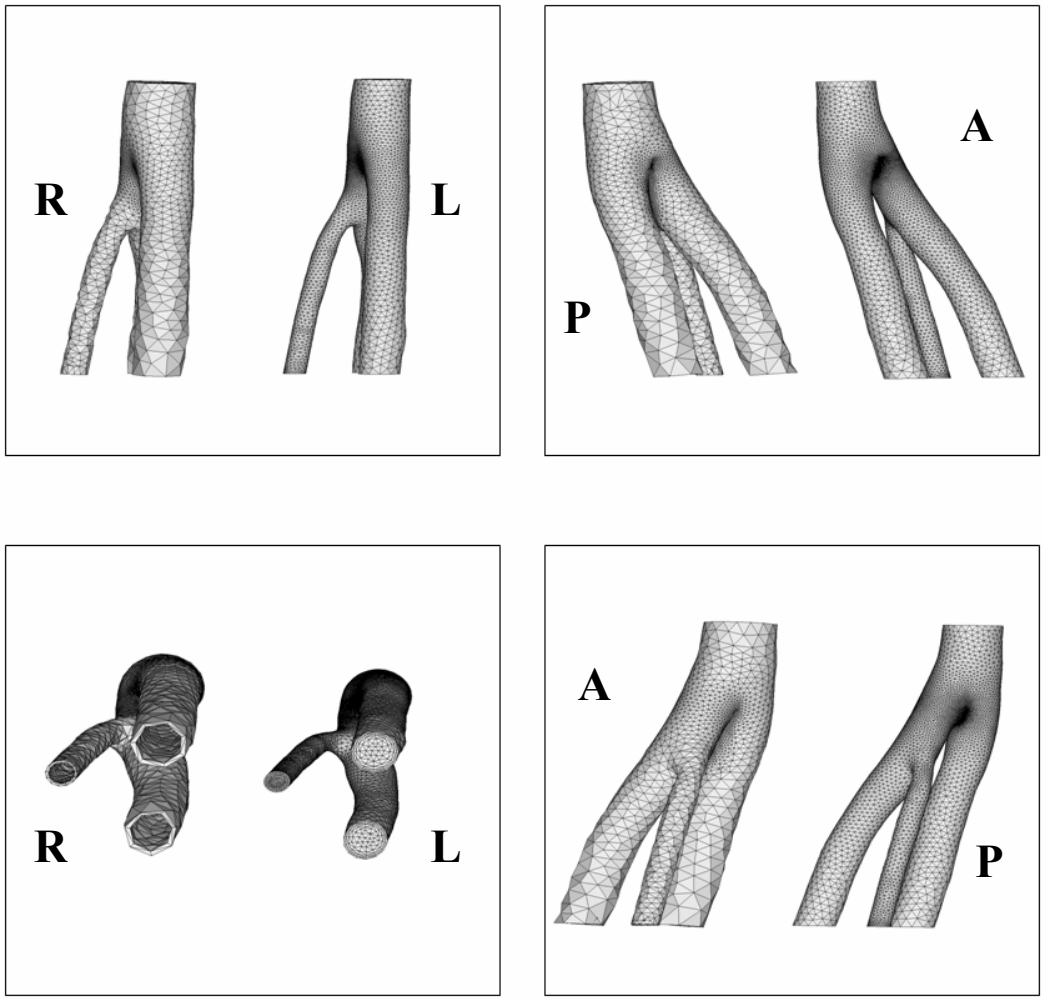

A: Anterior, P: Posterior, L: Left, R: Right

Fig. 7.17 Structural and fluid grid of in-vivo femoral artery bifurcation reconstructed from MRI

7.3.3 Parameters and boundary conditions

7.3.3.1 Structure

In order to consider mechanical consequent properties of surrounding tissues on the in-vivo artery, the relationship between stress and strain rate should be observed in MRI. Due to the high SNR of image, however, the relationship can not be found in this study. The blood vessel is assumed as homogenous, hyperelastic, nonlinear, and nearly incompressible material. Poisson's ratio is chosen as 0.4999 which is as close to 0.5 as possible to depict incompressible material. The density of the vessel is 1100 kg/m^3. The five coefficient Mooney-Rivlin model which is used in Ref. [151] is chosen to describe the material as shown in Table 7.2. The reconstructed in-vivo geometry has already expanded with equivalent displacement and residual stress due to the pre-stressed and pre-stretched. If the normal intraluminal pressure were loaded on this expanded geometry, the extra pressure could cause sudden expansion of the artery. Therefore, the pressure load should start at zero pressure in order to conserve the original in-vivo geometry at the starting cardiac cycle.

Table 7.2 Five parameters for Mooney-Rivlin model of femoral artery

Parameters	Values (kPa)
C_{10}	18.90
C_{01}	2.75
C_{20}	590.42
C_{11}	857.18
C_{02}	0

For doing this, one of five coefficients is modified using inverse FEM. With changing first one of the five coefficients, the relationship between stress and stretch ratio

in the uniaxial expansion with zero pressure at the boundary conditions can be obtained using

$$T_{11} = 2*\left(\frac{\partial W}{\partial \bar{I}_2}\bar{I}_2 + \frac{\partial W}{\partial \bar{I}_3} + \frac{\partial W}{\partial \bar{I}_1}B_{11} - \frac{\partial W}{\partial \bar{I}_2}B^{-1}{}_{11}\right) \tag{7.9}$$

where, T_{11} is first principal stress in Cauchy stress tensor, and B_{11} is one of left Cauchy-Green tensor. Mean expansion of diameter is set to 6.2% of CFA diameter [152] for the PAD patient at the systolic phase. Using Eq. (7.9) and inverse FEM, the final first coefficients is modified to 4000 Pa. The plot in Fig. 7.18 shows the uniaxial constitutive models depending on different coefficients.

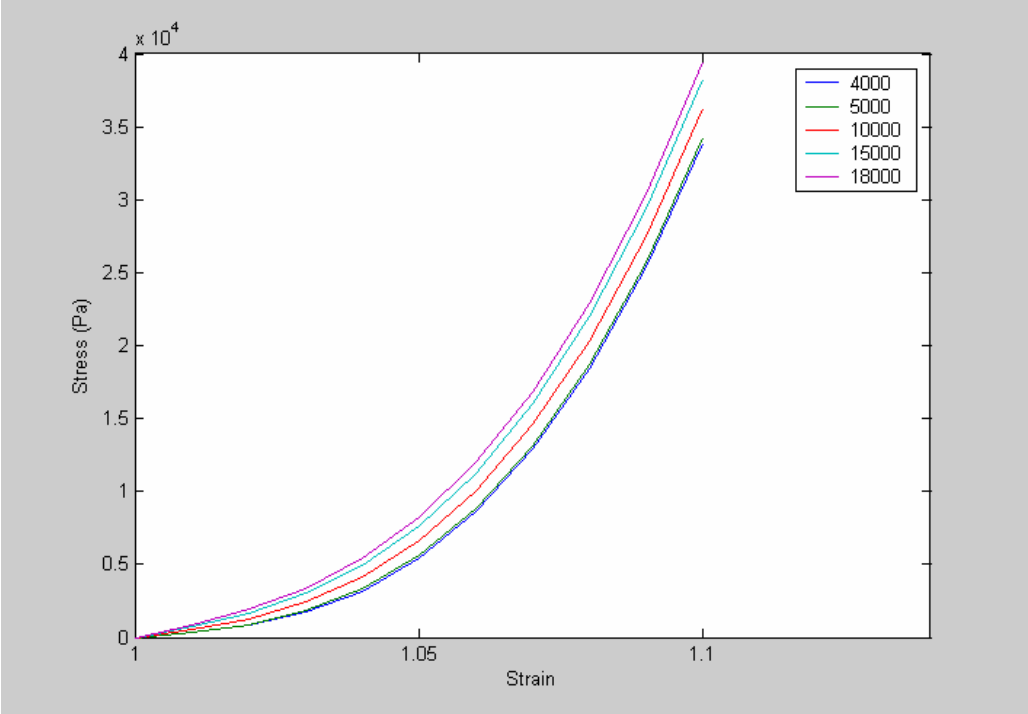

Fig. 7.18 Uniaxial constitutive models depending on different coefficients

7.3.3.2 Fluid

The flow is assumed to laminar, Newtonian, viscous and incompressible Navier-Stokes equation is chosen for analyzing the flow in FLUENT. The viscosity of blood is 0.0035 kg/m-s and the density is 1085 kg/m^3.

7.3.3.2.1 Inlet

Typically, the only flow rates calculated from MRI is required at the boundary for rigid wall boundary condition. However, the time-dependent pressure profile is indispensable for compliant wall simulation. In order to calculate pressure at the second locations of CFA as shown in Fig. 7.19, two physiological flow rate curves at the first and second location based on velocity profiles from magnitude and phase images are obtained as shown in Fig. 7.20.

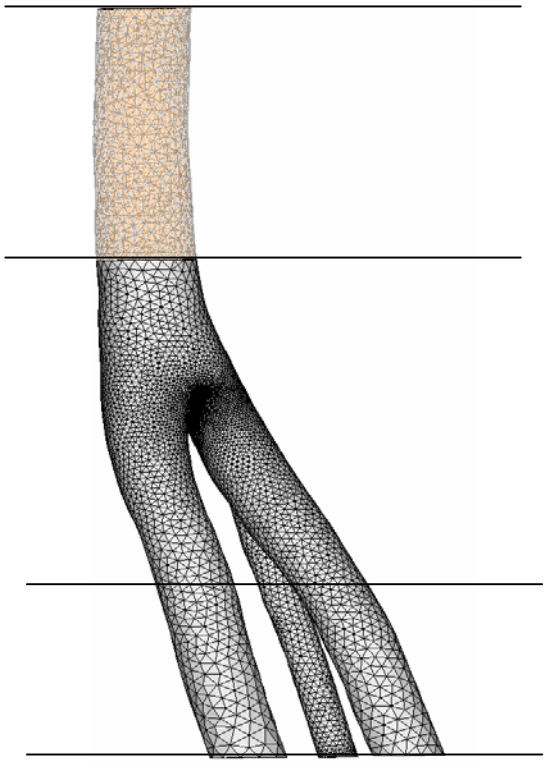

Fig. 7.19 Four locations for measuring velocity profiles

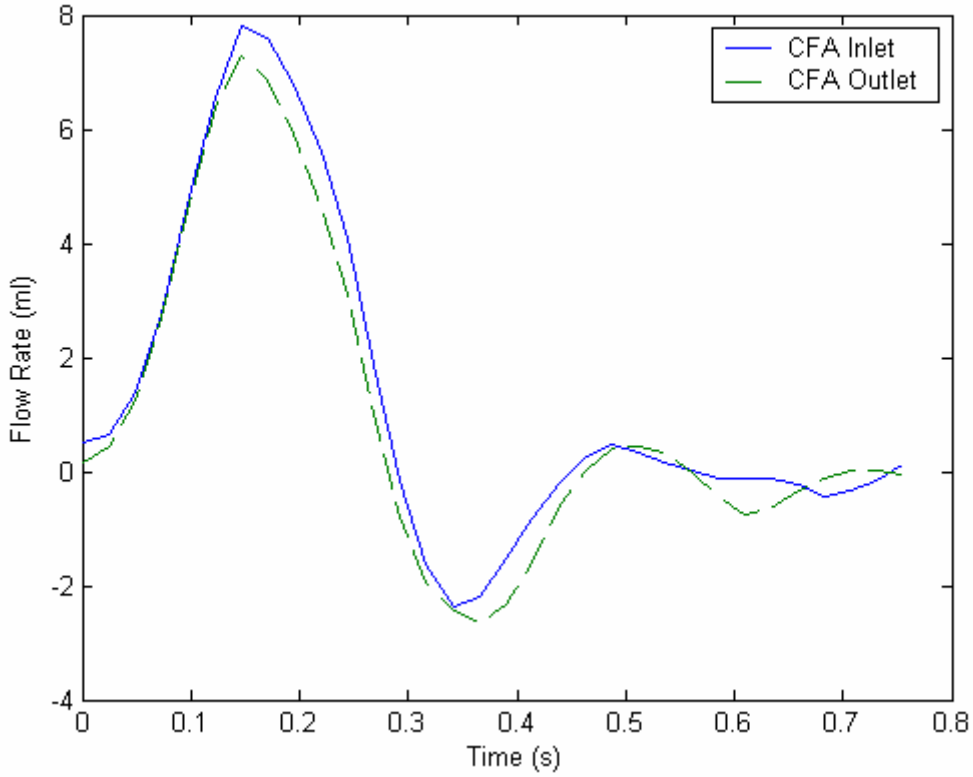

Fig. 7.20 Flow rates of CFA inlet and outlet

Navier-Stokes equation for one dimensional flow in an elastic tube can be reduced to [153]

$$Q_i(t) - Q_o(t) = \frac{3\pi r^3}{2hE}\frac{dP_o(t)}{dt} \tag{7.10}$$

where Q_i and Q_o is the flow rate at the inlet and outlet respectively, P_o is the pressure at the outlet, r is the radius of tube, h is the wall thickness, and E is the elastic modulus.

The shape of pressure waveform can be obtained using Eq. (7.10) as illustrated in Fig. 7.21. The pressure waveform was used for boundary condition at the end of CFA by UDF in FLUENT.

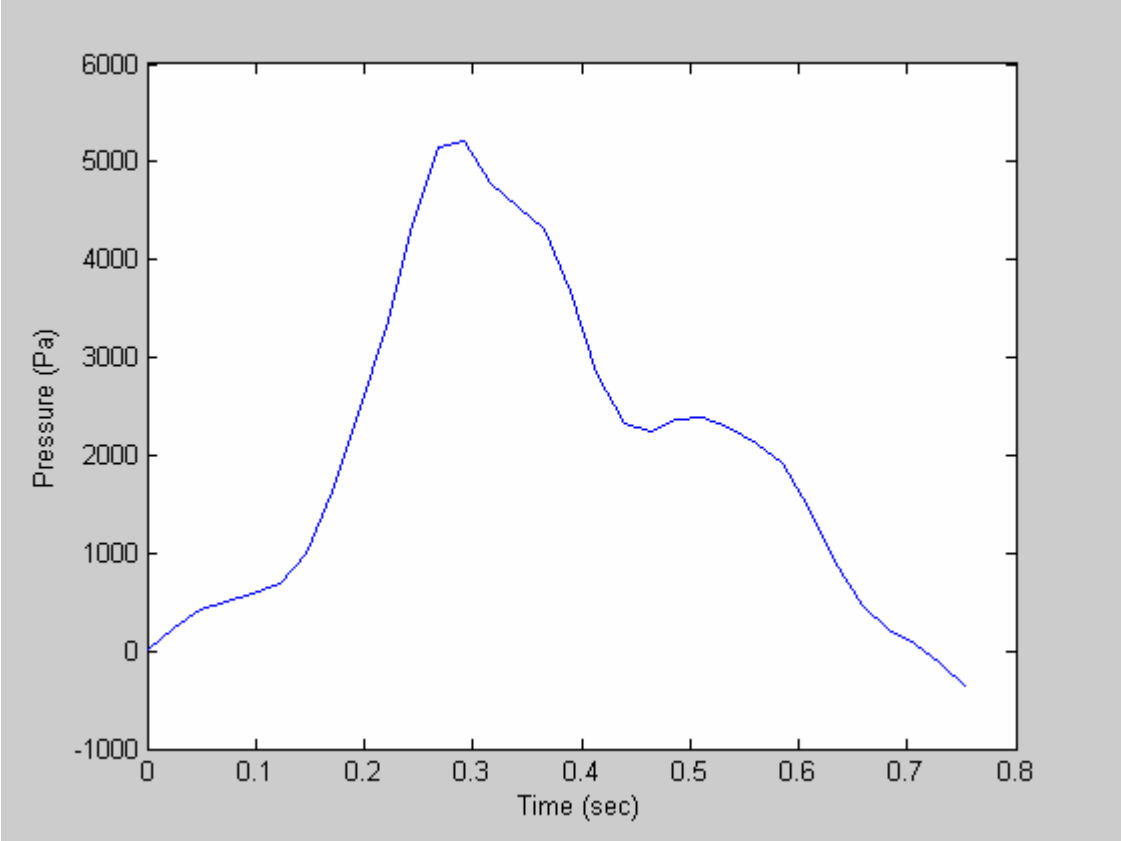

Fig. 7.21 Pressure at the second location of CFA

7.3.3.2.2 Outlet

Phase contrast MRIs is acquired for measuring blood flow velocity at four different locations, 39.2mm, 19.2mm above branch and 11 mm, 21 mm under branch, along the femoral artery, 60.2mm in length by a GE MR scanner (1.5 T, Signa). The scan parameter are 4mm slice thickness, 40 ms TR, 6 ms TE, 32 cardiac phases, 20deg FA, 113*150 cm FOV, and 512*512 matrix. The encoding velocity was 150 cm/s corresponding to 180 deg phase shift. Only axial velocity was measured under the assumption of relatively trivial in-plane velocity components. The 0.5894mm in-plane resolution is not enough to capture accurate velocity due to the strong disturbances at the

main bifurcation so that the four locations were chosen away from main bifurcation as shown in Fig. 7.19.

The measured velocity at the first location is used for the calculation of pressure drop between the first and second location. The pressure drop information is put on the inlet boundary condition in this simulation. The detail of calculation of the pressure drop will be described in the next section. Due to the phase image at the systole which has relatively high SNR, the region of interest was determined simultaneously checking magnitude image and signal gradient. The boundary of the defined ROI at the systole is used through entire cardiac cycle considering movement of center of ROI. The different centers of ROI at each time level were found by comparing maximum number of magnitude value over a threshold at the surrounding pixel of manually determined center. The velocity can be calculated with [154]

$$V = VENC * \Phi_v / 180°,\ \Phi_v = [-180°, \cdots 180°] \tag{7.11}$$

where, *VENC* is encoding velocity, and Φ_v is the phase angle obtained by phase image. The calculated velocity is mapped utilizing smoothing interpolation method [155].

Time-dependent velocity profiles were mapped through 32 cardiac phase. Around 40 pixels for SFA and PFA and 20 pixels for LCA to quantify velocity from their MRI was used. From the velocity, the velocities of 74 (SFA), 60 (PFA) and 147 (LCA) nodes are interpolated.

The flow rates at SFA, PFA and LCA outlets is consistent with MRI data of them through cardiac cycles globally as shown in Fig. 7.22. The smoothed and biased velocity profiles of them at systolic phases shown in Fig. 7.23 were reasonably consistent with

MRI velocity profiles which can not be generated from Womersley velocity profile. These time-varing mapped velocity files are used in FLUENT via UDF.

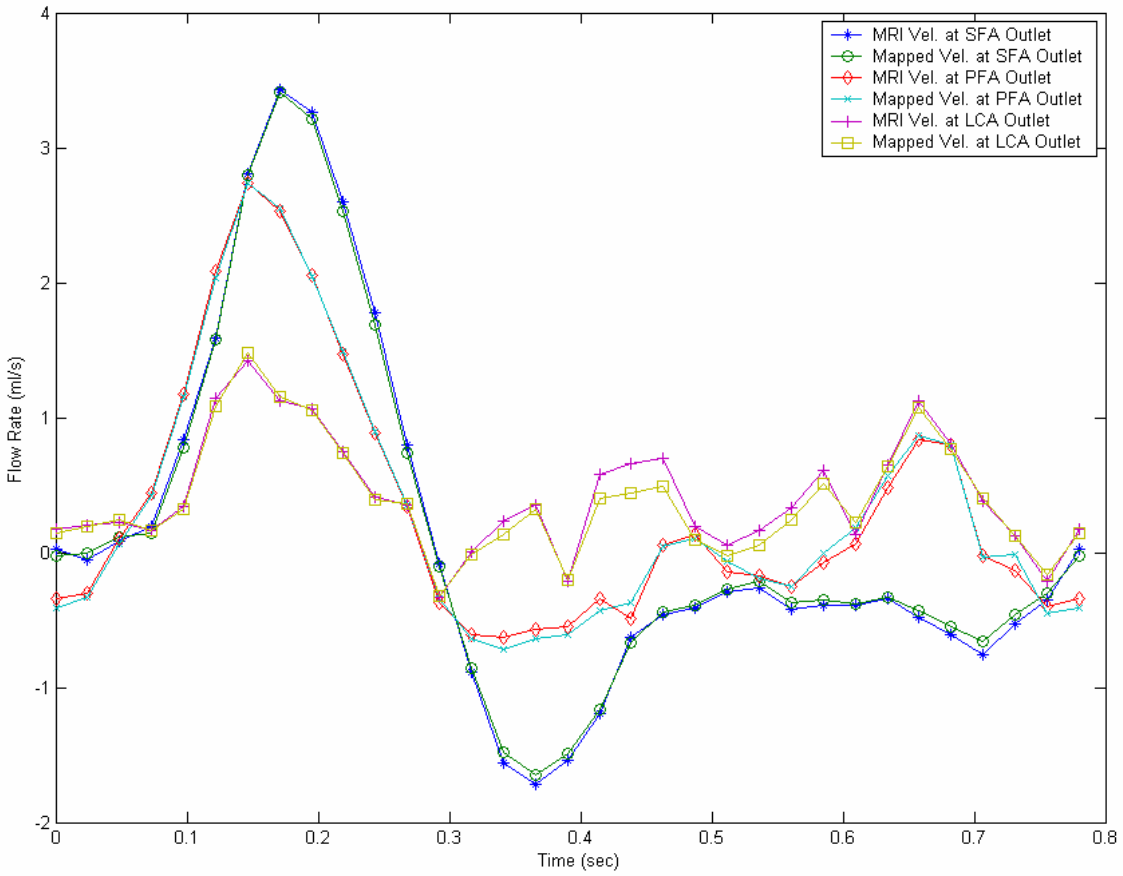

Fig. 7.22 Flow rate comparison of MRI and mapped velocity profiles at the SFA, PFA and LCA outlets.

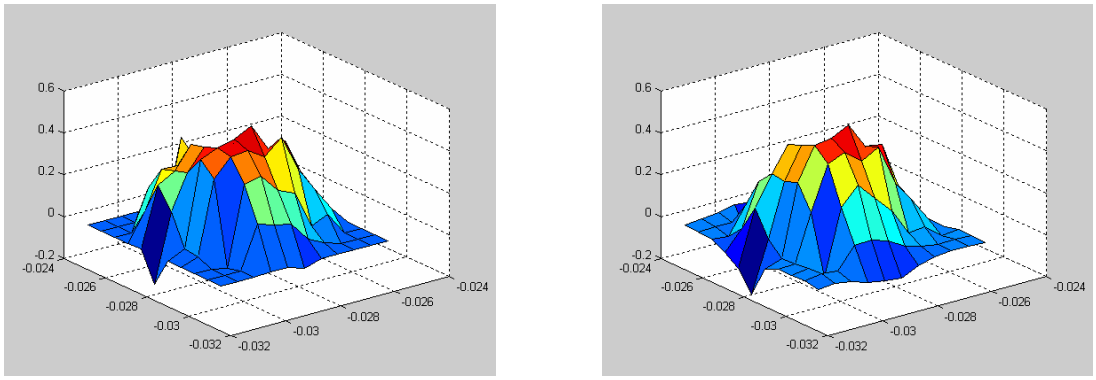

a) MRI **b) Mapped (TPS)**

Fig. 7.23 Comparison of MRI and mapped velocity at the systolic phase

7.3.4 Time mapping

After simulating the ANSYS and FLUENT with initial and boundary condition, time step is determined as 0.0121 and 0.00305 for solid and fluid for 0.78 second cardiac period, respectively. 64 iterations of interaction are implemented for one cardiac cycle using CSS method and subcycling method with Perl script and Dos batch command. Total 160 iterations that are the same as two and half cardiac cycles are performed to avoid initial perturbation for FSI. The auto-time step option in ANSYS is turned on to reduce CPU time and prevent divergence of solution.

7.3.5 Results

7.3.5.1 Flow pattern comparison

Fig. 7.24 shows the velocity contours in the z direction and secondary flow especially around bifurcation area at a deceleration phase for rigid and compliant arteries. The flow on the compliant artery show more reduced velocity than that on the rigid one. The streamlines in Fig 7.25 at the deceleration phases provide recirculation on the bulb

and PFA regions of compliant artery is stronger than that on them of rigid one. In addition, the stream lines in the SFA and PFA of both arteries follow commonly the curvature of the artery and slightly bias toward the anterior which has relatively high ratio of radius of curvature.

The effects of compliance on the flow pattern shows well when the maximum expansion of diameter on maximum pressure as shown in Fig. 7.26. The more biased flow pattern on the compliant artery is observed [156].

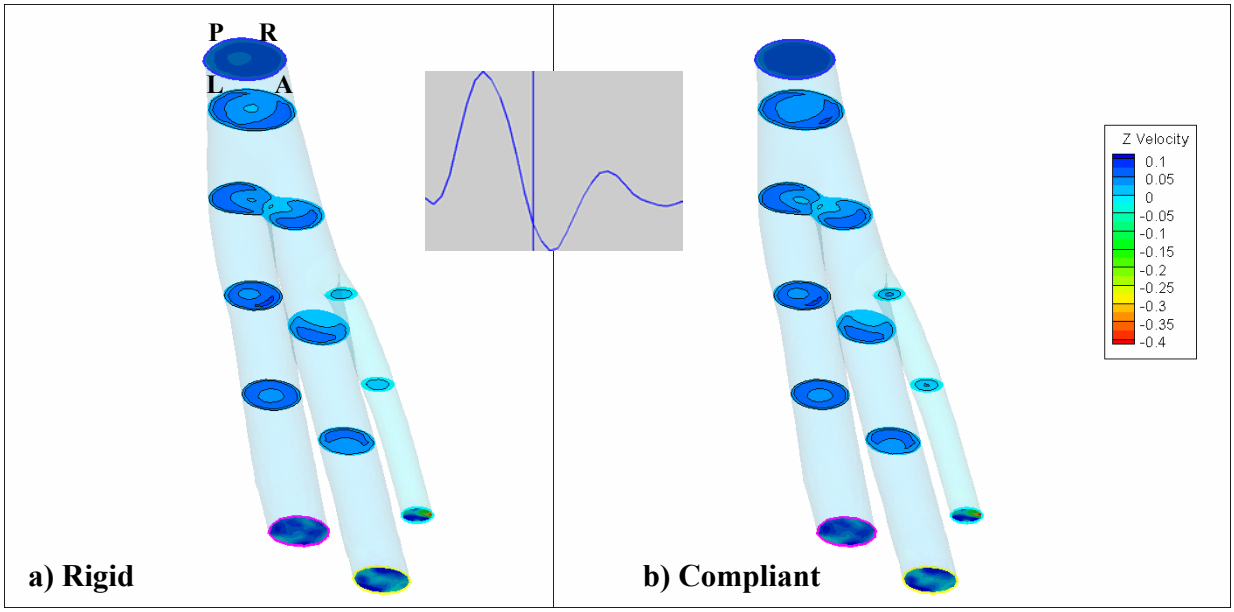

Fig. 7.24 Velocity contours in z direction of rigid and compliant artery (t = 0.3172 s)

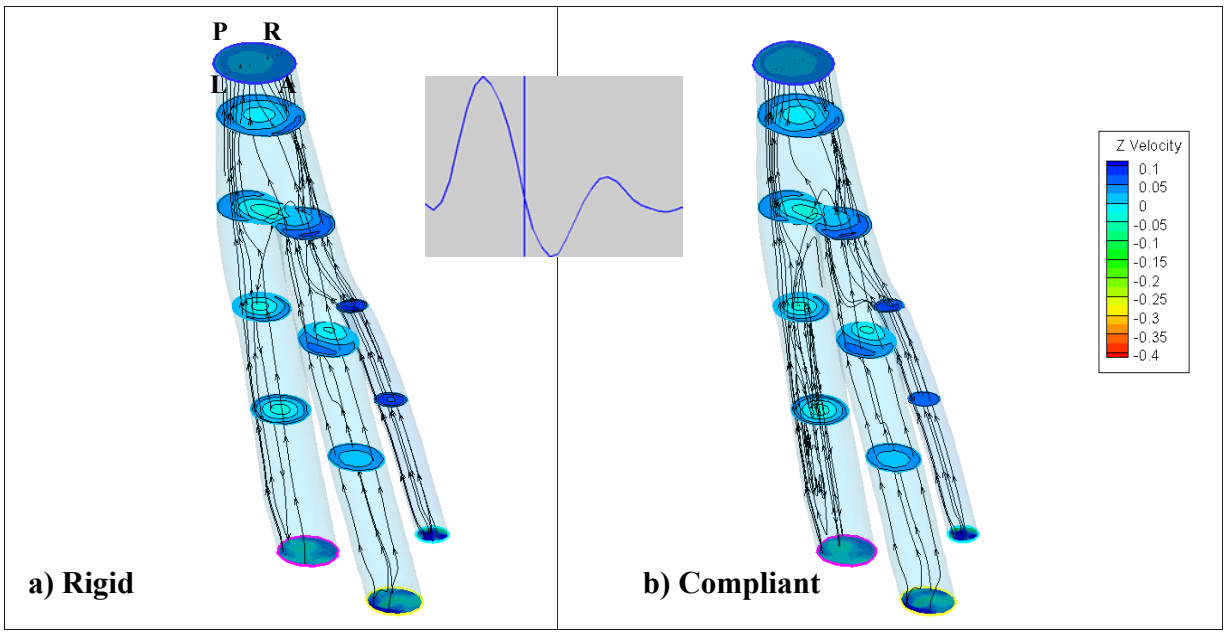

t = 0.2928 sec

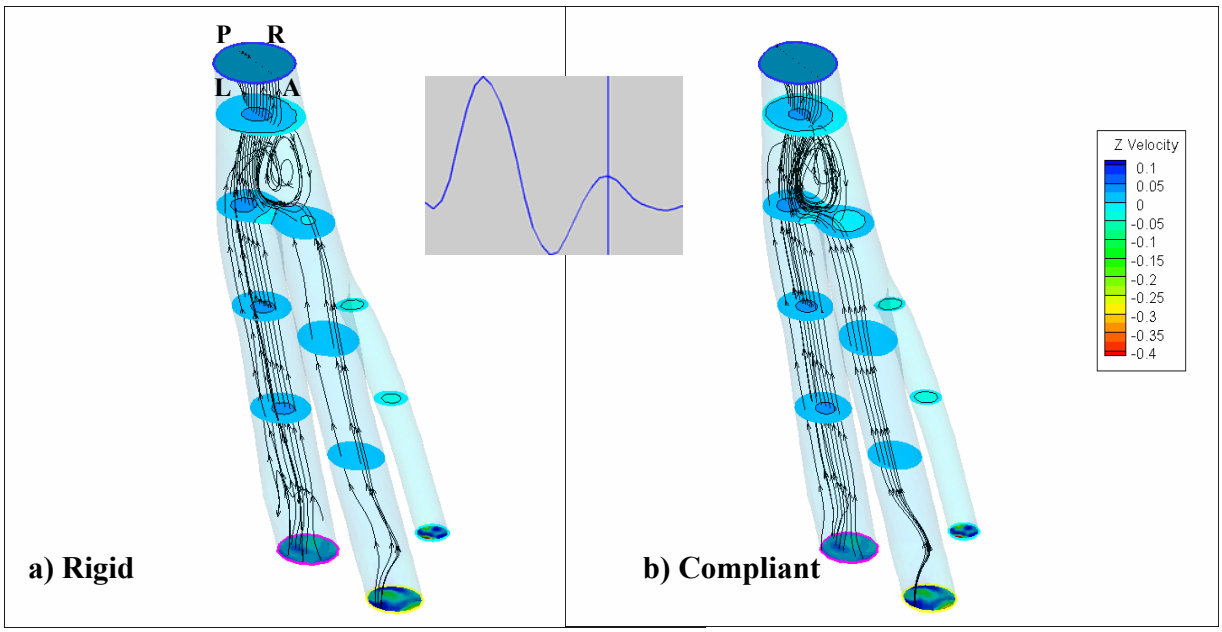

t = 0.5368 sec

Fig. 7.25 Stream line of rigid and compliant artery

Rigid **Compliant**

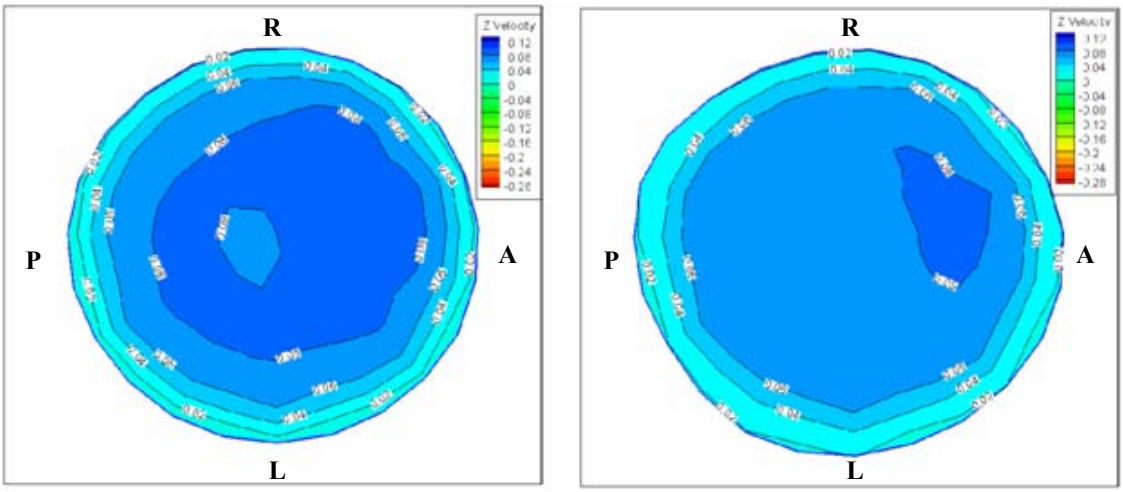

a) CFA Section at the second location in Fig. 7.19

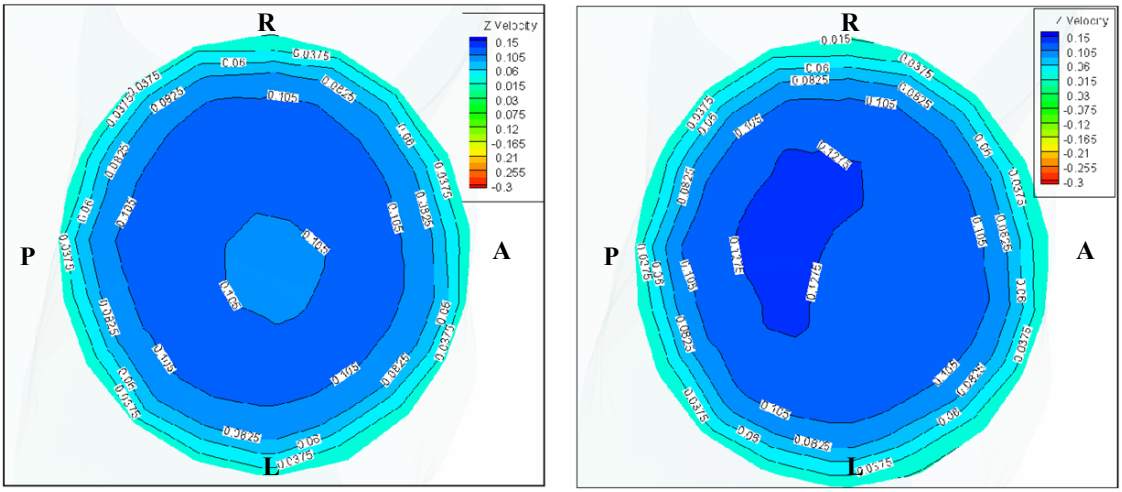

b) SFA Section at the third location in Fig. 7.19

Fig. 7.26 Velocity contour of CFA and SFA cross sections

7.3.5.2 Velocity validation with MRI

In order to validate computational and physiological data, the four position velocities of rigid, compliant, and MRI cross sections at the third location in Fig. 7.19 are extracted and compared as shown in Figs. 7.27 and 7.28. The results of rigid and compliant arteries do not demonstrate the severely skewed velocity near the anterior and

left wall at the peak systolic phase and small amplitude due to the reflection of pulse wave at the diastolic phase. However, the differences of velocity between anterior-left and posterior-right wall around the peak diastole are shown only in compliant artery. The differences may be strongly influenced by expansion of diameter, because the maximum pressure is loaded on the artery wall around the peak diastole. During the peak diastole, the velocity profiles of SFA cross section measured at the third location in Fig. 7.19 are compared as illustrated in Fig. 7. 29. The biased velocity profile of compliant artery is consistent with MRI data.

7.3.5.3 Wall displacement

Time-varing lumen diameters of CFA and SFA are measured at the second and third locations in Fig. 7.19. The maximum anterior-to-posterior lumen diameters of CFA and SFA at the peak pressure load are 6.3457 and 4.67 mm which is 5.7 and 3.7 percentage expansion of lumen diameter during diastolic cycle respectively as shown in Fig. 7. 30. Increase of anterior-to-posterior lumen diameters of CFA and SFA is larger than that of right-to-left ones. The much difference between anterior-to-posterior and right-to-left lumen diameter of SFA may be affected by the curvature of it.

7.3.5.4 Wall shear stress

The WSS distribution at the peak systole is illustrated in Fig. 7.31. It seems to be no differences between the rigid and compliant arteries in the figures. For finding the differences, the WSS values of entire rigid and compliant wall are compared and two locations of maximum difference are found in the range of 0 to 4 Pa as shown in Fig. 7.32. The WSS's of posterior wall of rigid/compliant CFA and PFA are shown in Fig. 7.33. The WSS of rigid artery is bigger than that of compliant one. In addition, the differences

of WSS of CFA and PFA around maximum pressure load are relatively big as plotted in Fig. 7.34. Therefore, the WSS is primarily affected by the velocity of blood flow and secondary by the compliance of arteries wall in the main effects of geometry of the arteries.

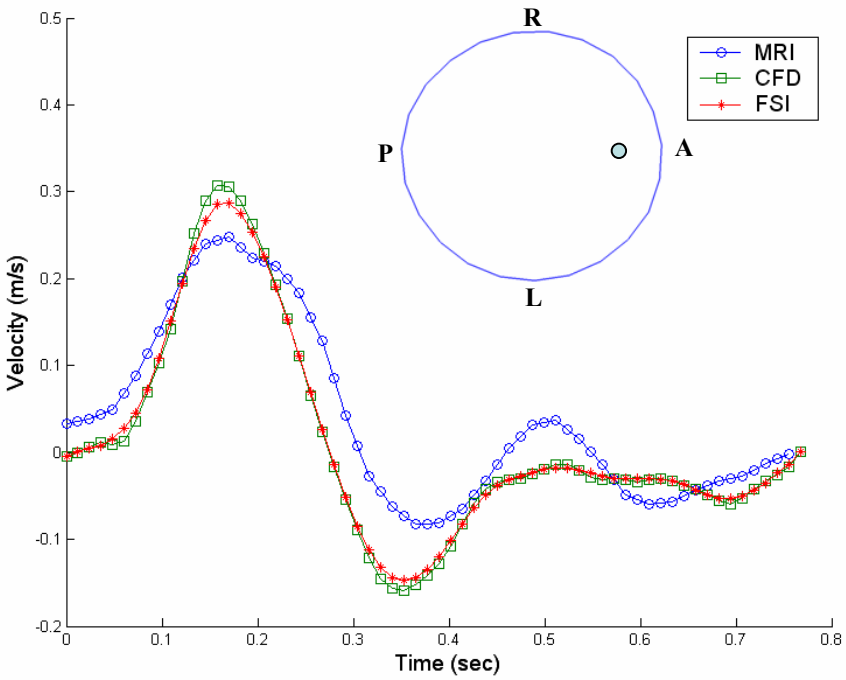

a) Anterior

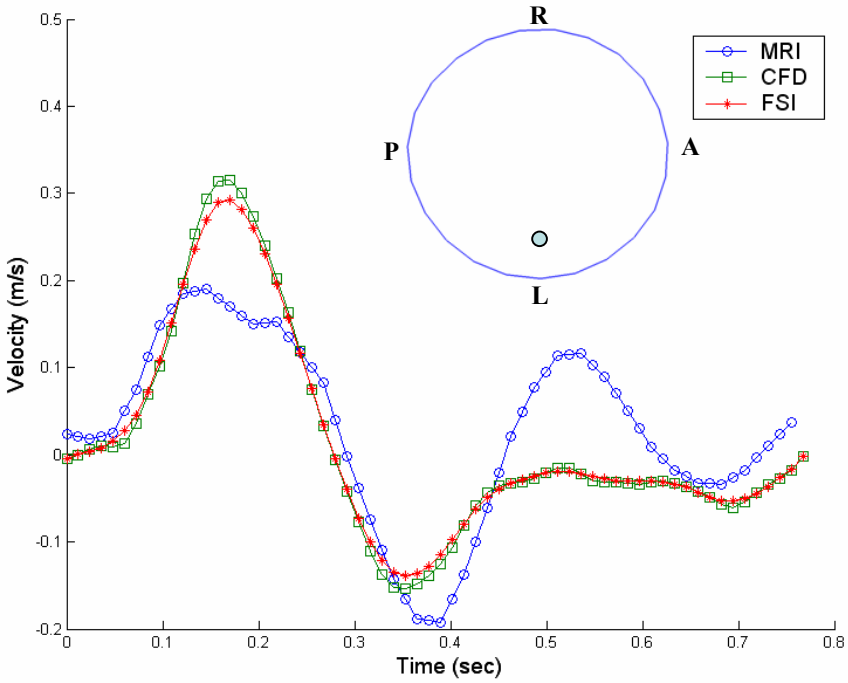

b) Left

Fig. 7.27 Time-dependent velocity near anterior and left wall

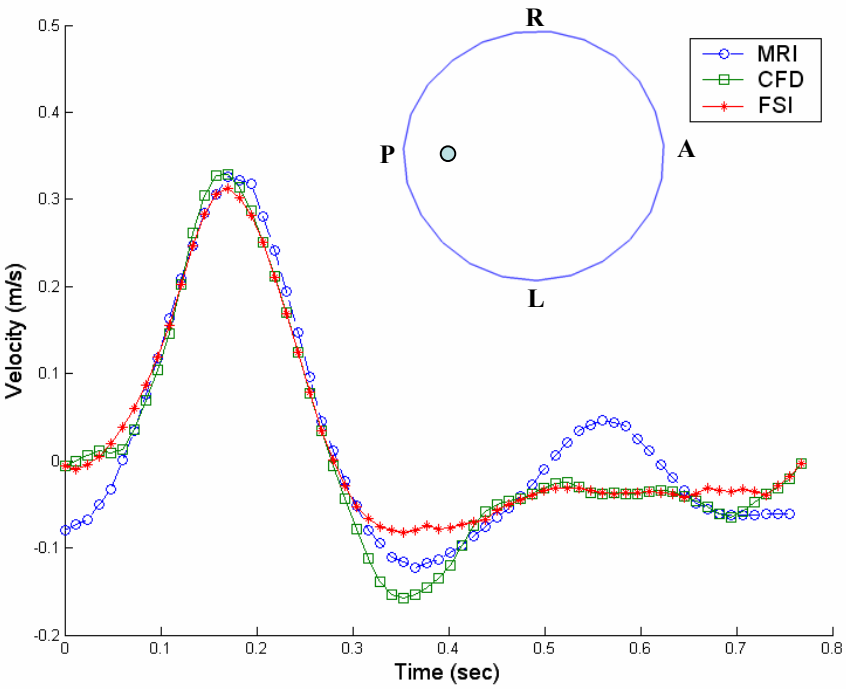

a) Posterior

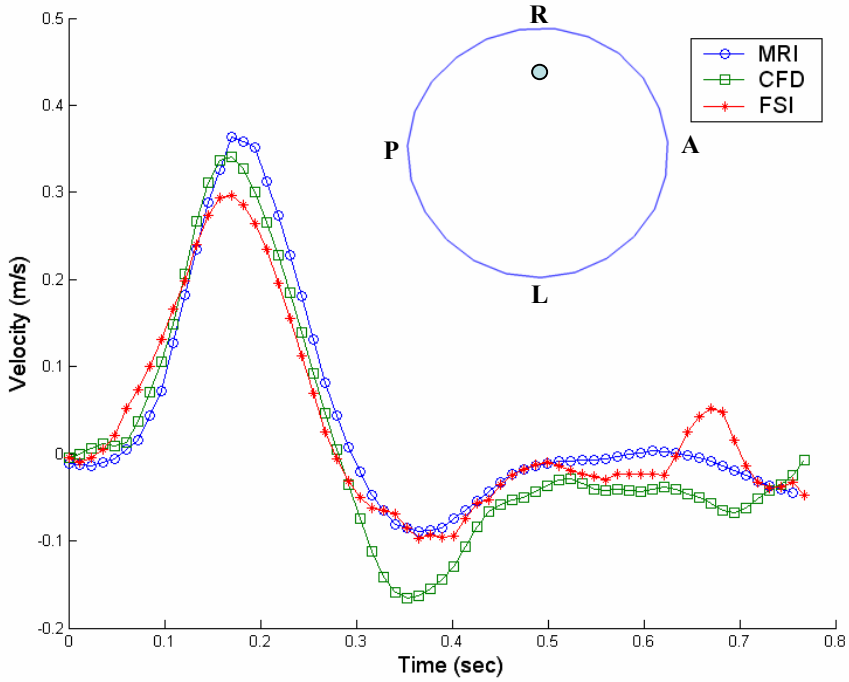

b) Right

Fig. 7.28 Time-dependent velocity near posterior and right wall

a) Compliant

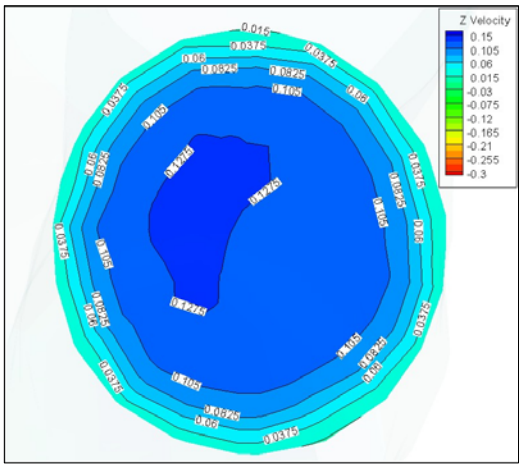

b) MRI

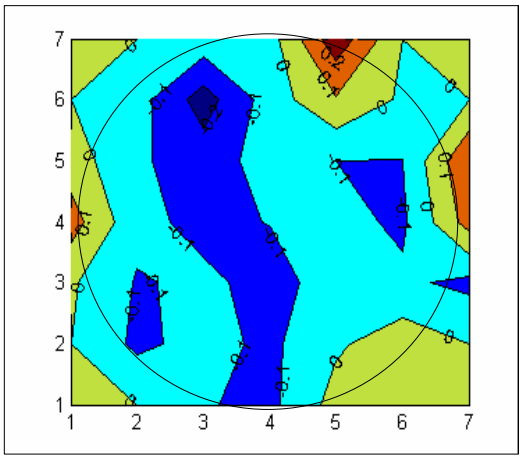

c) Rigid

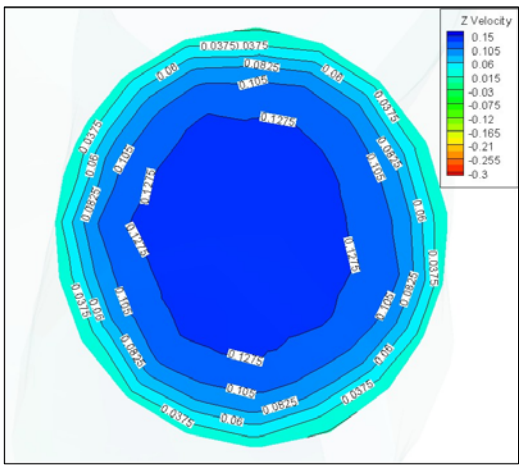

Fig. 7.29 Comparison of MRI and velocity of compliant/rigid SFA model

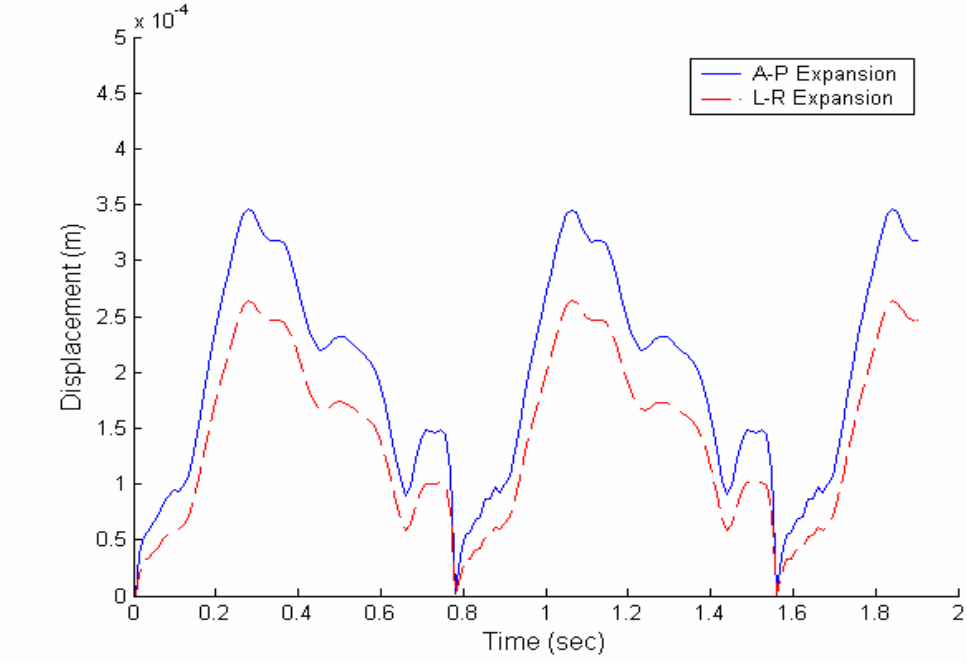

a) CFA

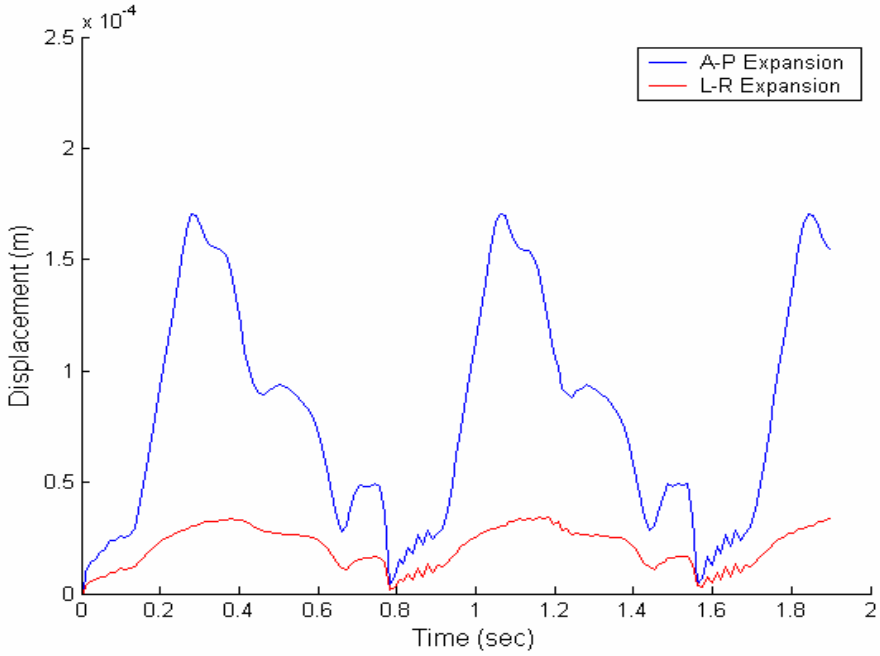

a) SFA

Fig. 7.30 Time-dependent lumen diameters of CFA and SFA

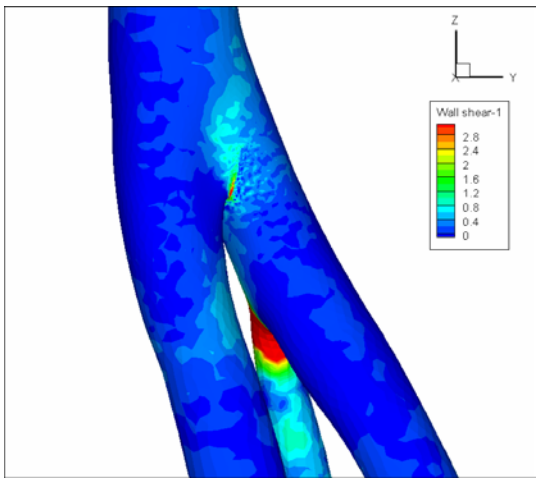

a) Rigid (Right)

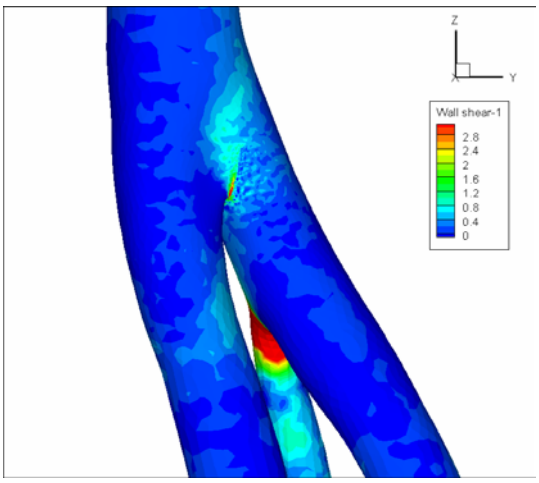

b) Compliant (Right)

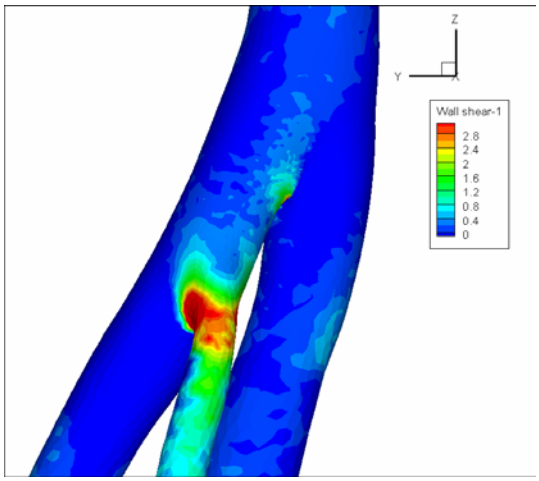

c) Rigid (Left)

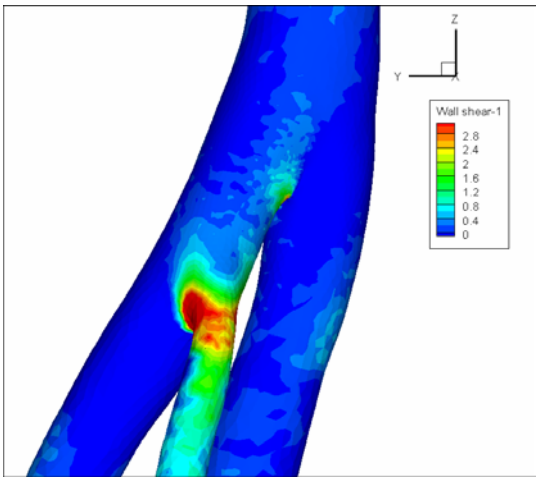

d) Compliant (Left)

Fig. 7.31 Wall shear stress distribution at peak systole

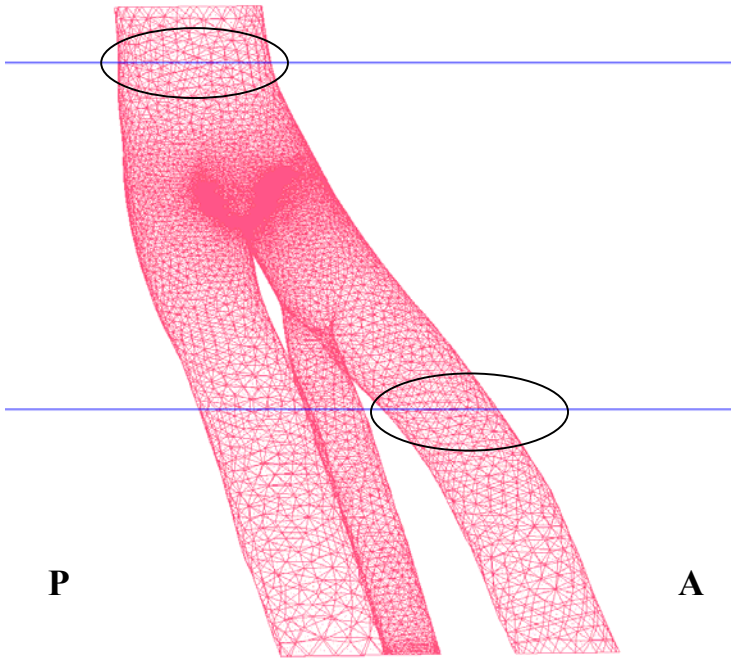

Fig. 7.32 Locations of measurement of WSS in CFA and PFA

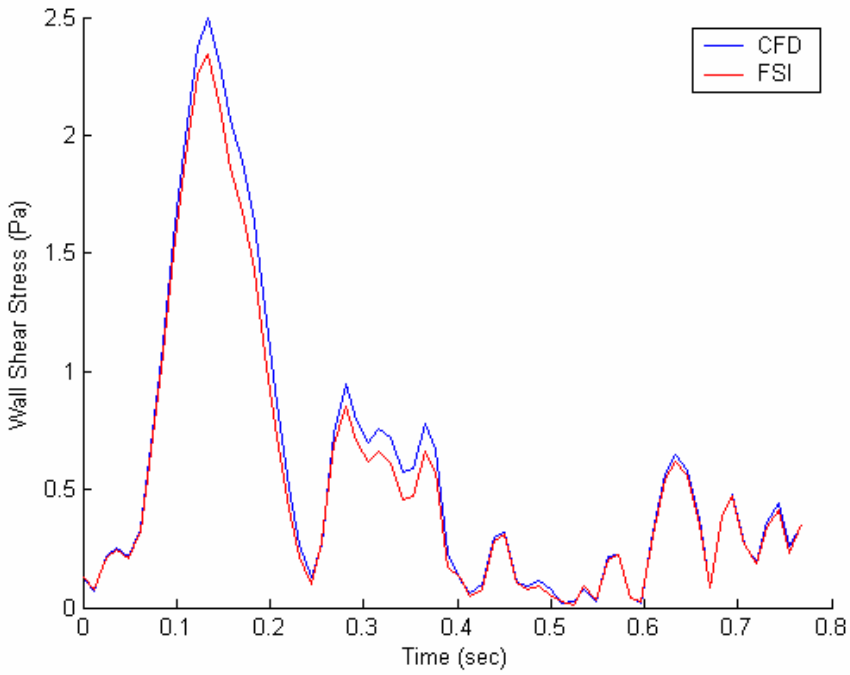

a) CFA

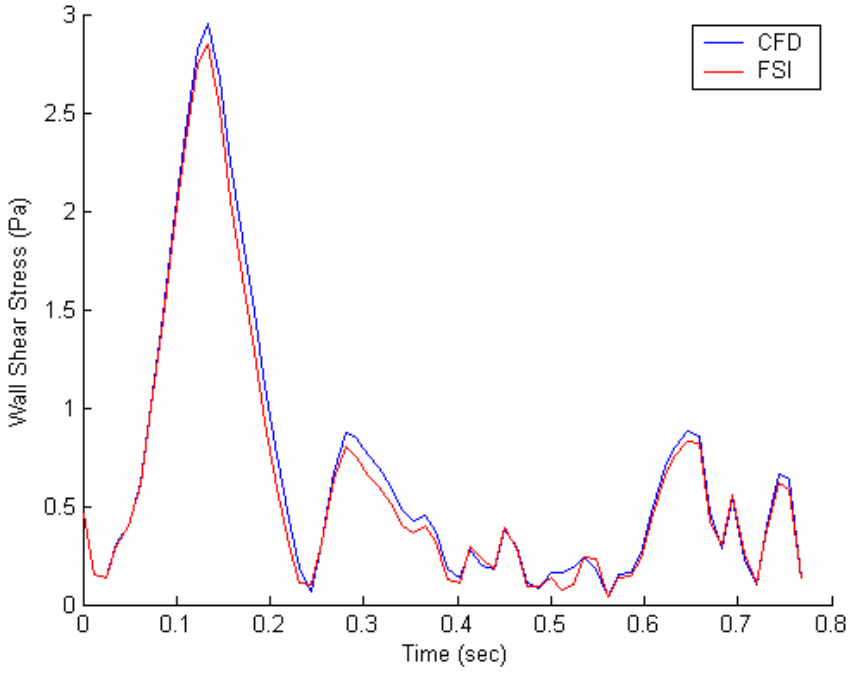

b)PFA

Fig. 7.33 Wall Shear Stress on posterior wall of CFA and PFA

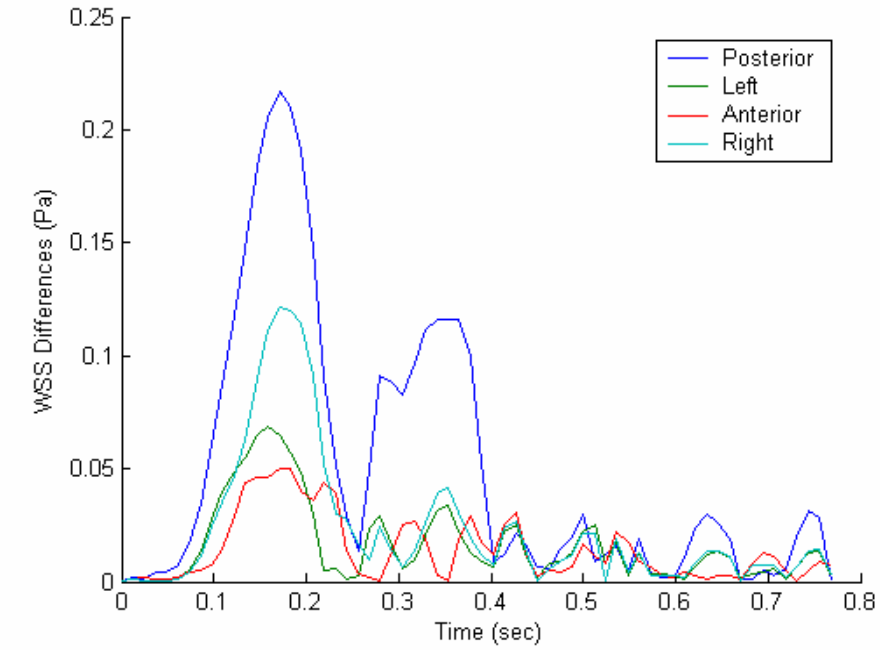

a) CFA

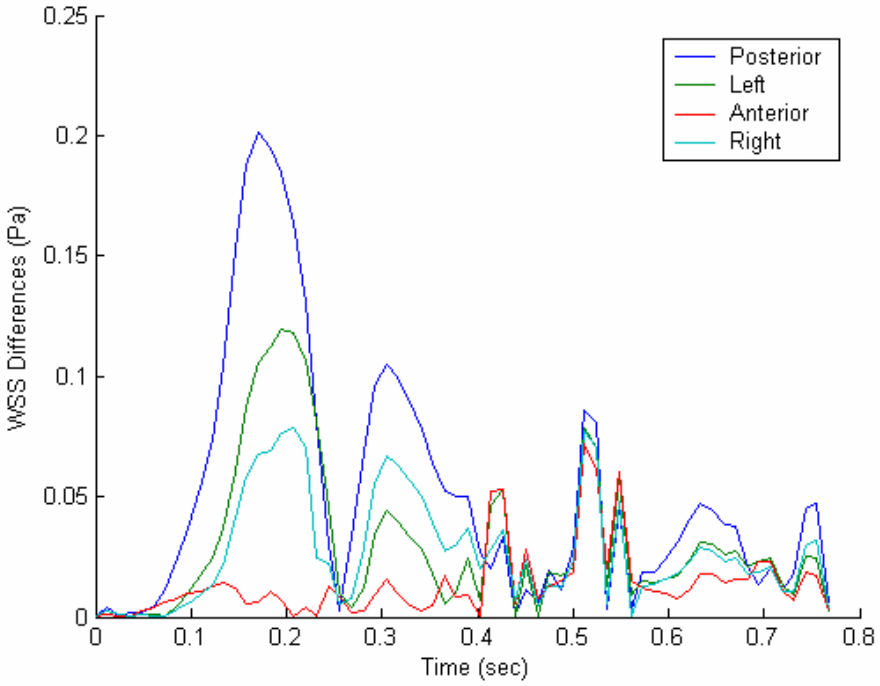

b)PFA

Fig. 7.34 Wall Shear Stress Differences between rigid and compliant CFA and PFA

7.4 Application III - Flutter of AGARD 445.6 Wing

7.4.1 Introduction

Flutter phenomena, one of aeroelastic instabilities of aircrafts, can be elucidated by FSI analysis. Recent advances in computational algorithms and hardware enable to analyze flutter problems of flight vehicles in an efficient and accurate manner [12, 157-159]. Especially, the flutter analysis of the AGARD 445.6 wing is a milestone for validating new developed FSI tools because the experimental data of the analysis are well documented [160]. Most of the FSI studies have used the conventional modal method that provides only flutter frequency and mode shape [161-163].

In this study, for a better insight of physical responses of the flutter, time marching full dynamic method is employed. The results from newly developed loosely-coupled FSI framework show good agreement with experimental data.

7.4.2 Geometry and grid

AGARD 445.6 wing has a quarter-chord sweep angle of 45 degrees, 1.65 for a panel aspect ratio, 0.66 for a taper ratio, and a NACA 65A004 airfoil type for cross section of the wing. The root chord of the wing is 0.559 m and the semi-span is 0.762 m. The detailed graphical geometry information can be found in Ref. [160].

The flow domain and common interface are discretized by 334,935 tetrahedral and 21,414 triangular elements, respectively. Fine mesh is employed in the leading and trailing edges to catch flow disturbance and generate exact NACA00649 airfoil type. The wing structure and common interface are discretized by 15,839 tetrahedral and 8,766 triangular elements, respectively. Fig. 7.35 illustrates the fluid and structural grid and grids for common interface.

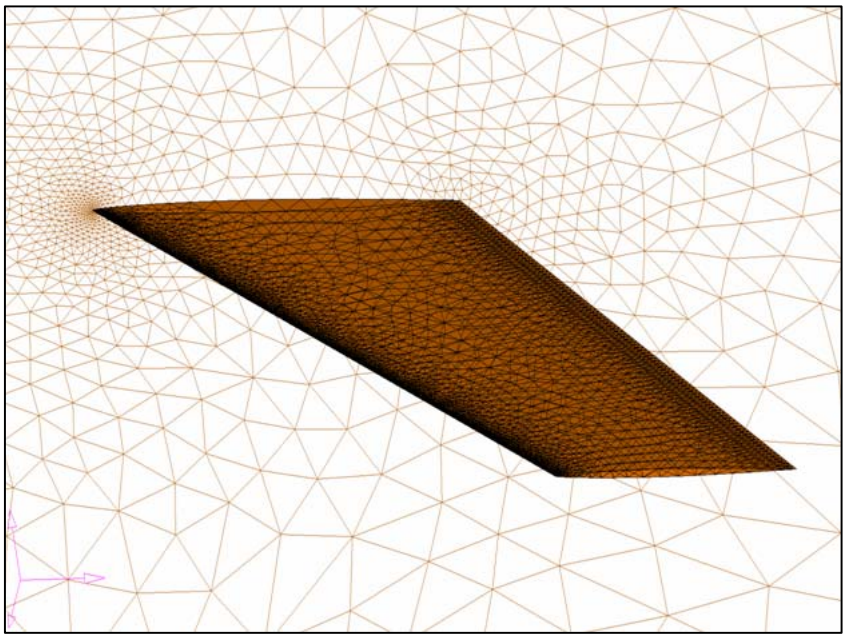

a) Fluid domain

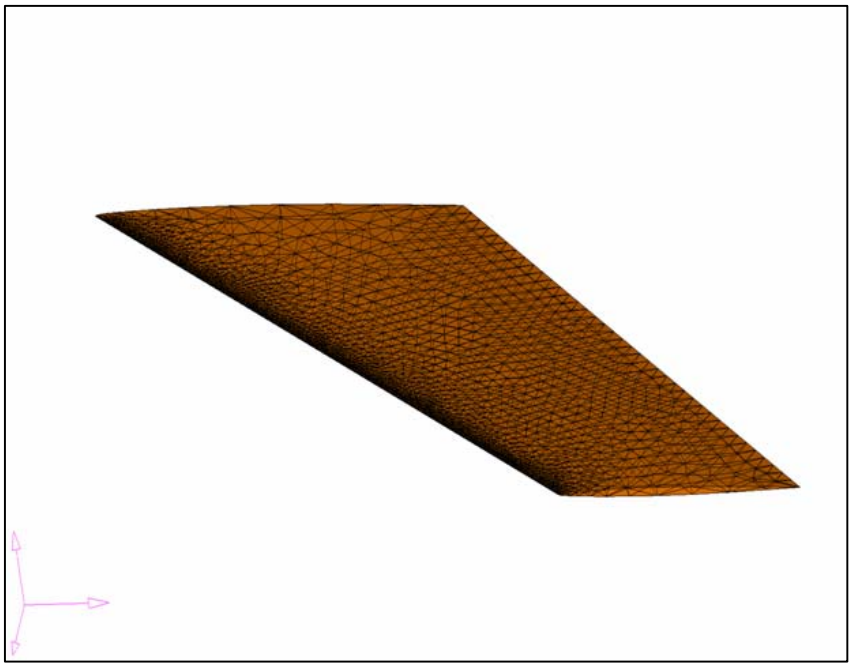

b) Structural domain

Fig. 7.35 Fluid and structural grids for AGARD 445.6 wing

7.4.3 Parameters and boundary conditions

7.4.3.1 Structure

The original wing used in the experiment [160] is made of laminated mahogany wood. The wing is perforated with holes along the leading and trailing edges. Ref. [160] provides total mass information, but it does not provide enough information for entire parameters for wing structures.

The wood has fibers along the wing span (x axis) which is swept 90 degrees with respect to y axis. The z axis is defined along the thickness of airfoil. Based on the coordinate systems defined above, the orthotropic mahogany wood properties [164] are listed in Table 7.3. The Poisson's ratios are shown in Table 7.4. The density is 415 kg/m^3.

Table 7.3 Elastic properties used for AGARD 445.6 wing

	Elastic modulus (GPa)
E_x	9.239
E_y	0.604
E_z	1.011
G_{xy}	0.623
G_{xz}	0.794
G_{yz}	0.264

For validating the finite element model with the material properties, a modal analysis is performed. The results of modal analysis agree with experimental data as shown in Table 7.5.

Table 7.4 Poisson's ratios used for AGARD 445.6 wing

Poisson's ratio	Values
ν_{xy}	0.034
ν_{xz}	0.033
ν_{yz}	0.326

Table 7.5 Natural frequency comparison of experimental and computational data

Natural Frequency (Hz)		
Mode	Experimental data	Computational data
1	9.60	9.59
2	38.10	39.30
3	50.70	53.36

7.4.3.2 Fluid

The fluid field is assumed as a laminar, Newtonian, viscous and incompressible flow. Navier-Stokes equation is chosen for analyzing the flow in FLUENT. The viscosity and density of air are set to 3.563e-05 kg/m-s and 0.428 kg/m^3, respectively. From the experimental results in the Ref. [160], the flutter frequency is 20.38 Hz at Mach number 0.499. In the FSI analysis, two tests are performed with Mach number 0.294 (dynamic pressure 2,209 Pa) and 0.499 (dynamic pressure 6,373 Pa) to capture stable and flutter conditions, respectively.

7.4.4 Time mapping

Time steps are determined as 0.005 and 0.0005 for CSD and CFD solver respectively. The time step for CSD solvers is set to be small enough to catch the experimental flutter frequency. Only CFD simulation is executed base on the time step until the solution is converged. From the convergence information, 10 subcycling time step for the CFD solver is determined. With the determined time step, 200 and 150 iterations for flutter and non-flutter cases are implemented, respectively. The auto-time step option in ANSYS is turned on to reduce CPU time and prevent divergence of solution.

7.4.5 Results

Fig. 7.36 illustrates the time-history displacement of leading and trailing edge at the tip of the wing at Mach 0.499 and 0.294 without structural damping. Since the structural damping effect is not considered in the FSI simulation, the wing tip of the case of Mach number 0.294 oscillates with constant amplitude and its tip of the case of Mach number 0.499 oscillates with increasing amplitude. However, the flutter frequency 19.5 Hz is similar to experimental flutter frequency 20.38 Hz. The snapshots of total pressure distribution at the time intervals are illustrated in Fig. 7.37.

7.5 Summary

The effects of compliance of blood vessel wall on arterial flow patterns or vice versa have been investigated through the simulation of straight/curved stenotic artery and in-vivo femoral artery bifurcation with the new FSI framework. In addition, the structural responses of aircraft wing in the flight envelops have been analyzed via simulating the flutter of AGARD 445.6 wing.

In the analysis of pulsatile flow through compliant straight/curved carotid stenotic arteries, the pulsatile flow was modeled by sinusoidal waves and Mooney-Rivlin model was used for the arteries. The arteries were pre-stretched and pre-stressed to consider residual stresses that play an important role in the mechanical response of the wall. The results from the simulation of the straight artery showed a little difference with the experimental results in terms of displacement, but the phase delay that can be detected only by FSI simulation was consistent with the experimental results. The strong recirculation of flow and high velocity on the outer wall in the curved stenotic artery demonstrated that the curvature an compliance of the artery plays a key role in the flow patterns and consequently affects WSS distribution on the wall.

For one of biofidelic and physiological applications, hemodynamics and structural responses of the in-vivo common femoral artery bifurcation have been performed. The pressure boundary condition at the inlet which was calculated from one-dimensional Navier-Stokes equation in elastic tube utilizing patient-specific MRI velocity profiles. The velocity mapping by the smoothing interpolation of MRI data at the three outlets (SFA, PFA, and LCA) was applied to observe the effect of skewed velocity profile from the curvature of the arteries. An inverse method for finding material coefficients used in an in-vivo material constitutive model was employed to prevent sudden expansion of blood vessel corresponding blood pressure during diastolic phase. Comparison of the flow pattern and WSS of rigid and compliant femoral artery bifurcation demonstrated that the FSI simulation with the FSI framework was more in line with experimental data than rigid body simulation. The results of two biomechanical applications demonstrated that the FSI framework can be a useful tool to enhance our understandings of the effects of

mechanical behaviors occurred by FSI on the development and progress of atherosclerosis.

Flutter and non-flutter cases of AGARD 445.6 wing using time marching full dynamic FSI analysis instead of conventional modal one were described in the third application. At Mach 0.499, a flutter boundary from the experiment, the wing oscillated with increasing amplitude due to the deficiency of realistic structural damping in this case. However, the flutter frequency 19.5 Hz was similar to experimental flutter frequency 20.38 Hz. Time marching full dynamic method, which is easily performed by the loosely-coupled FSI framework, enables to analyze large amplitude and time-dependent motion and nonlinear fluid behavior such as separated flow and turbulence, although it requires more computing time than conventional modal approach.

The results of three applications demonstrated that the new FSI framework is a useful and powerful tool for investigating and analyzing physical FSI phenomena.

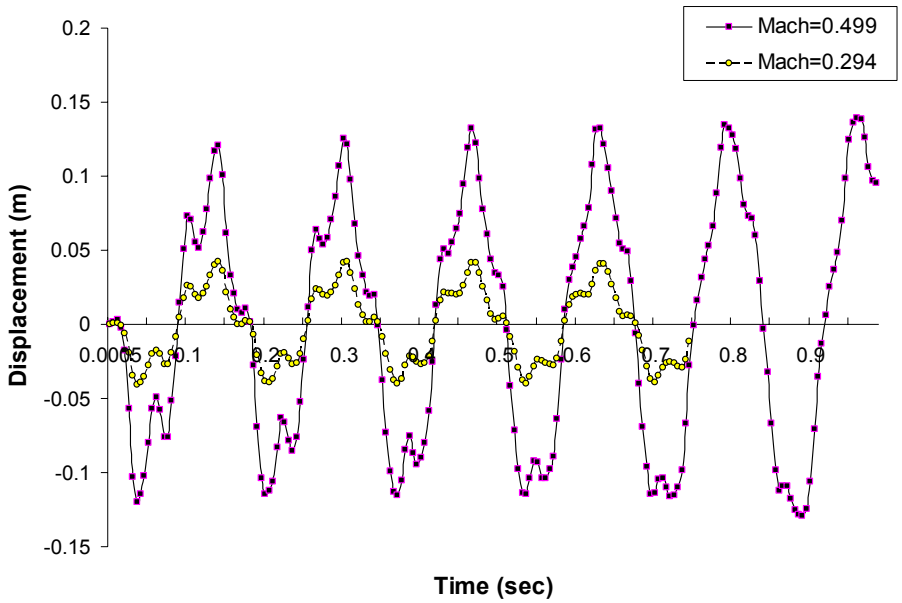

a) Trailing edge

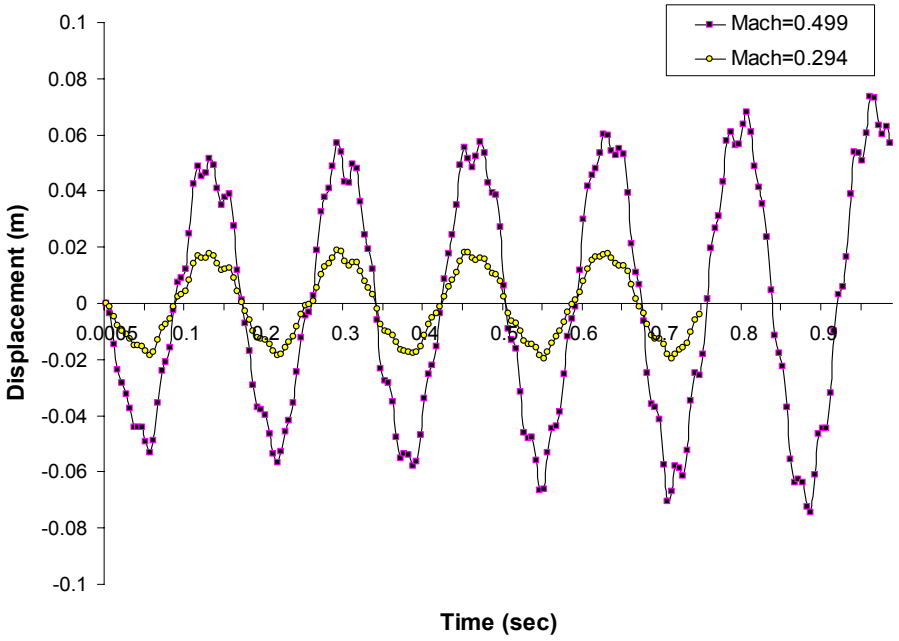

b) Leading edge

Fig. 7.36 Tip displacement comparison of Mach 0.499 and 0.294 at leading and trailing edge

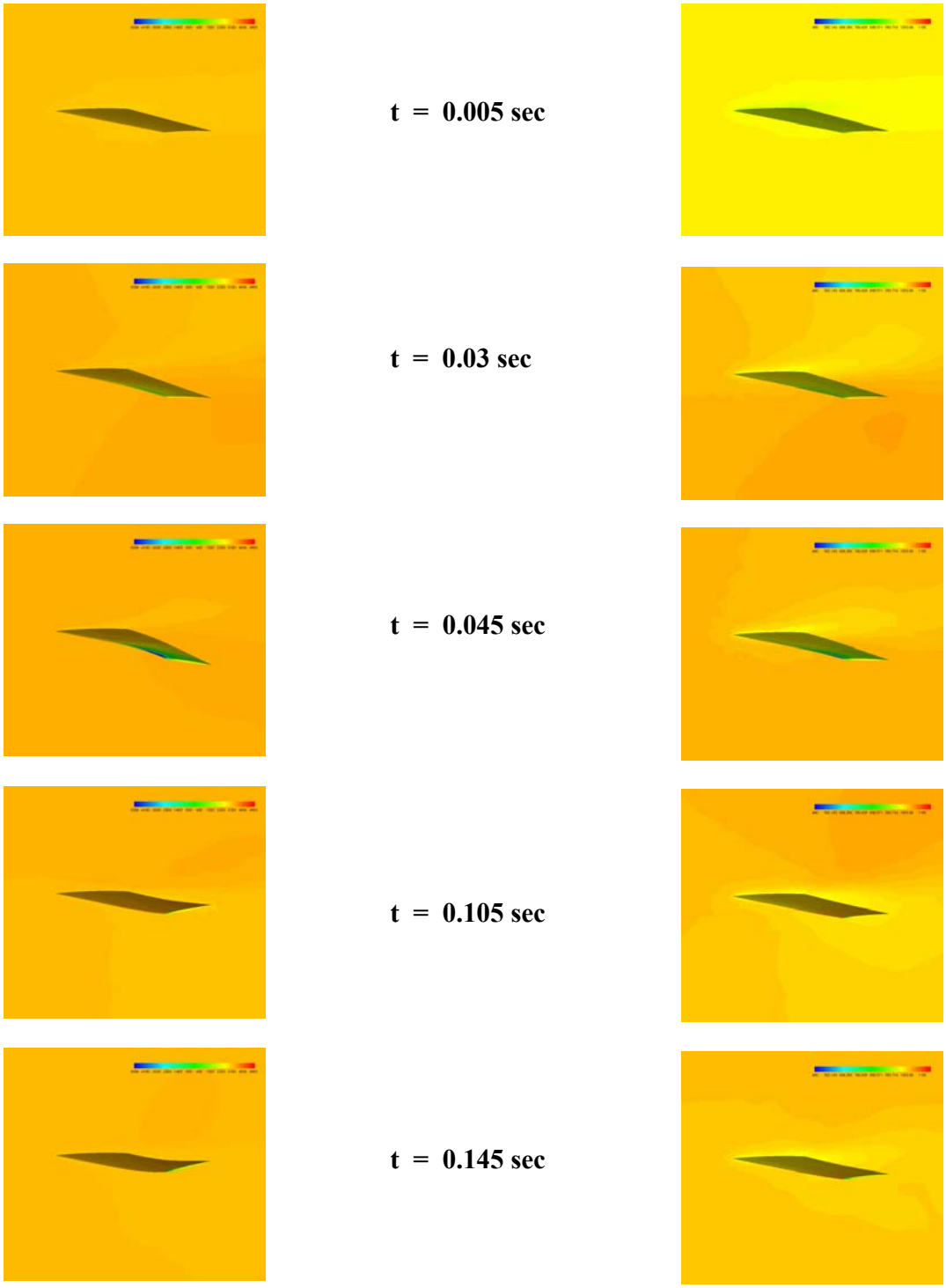

a) Mach 0.499 **b) Mach 0.294**

Fig. 7.37 Total pressure distribution of AGARD 445.6 wing

CHAPTER 8

CONCLUSIONS

A fluid structure interaction (FSI) framework was developed to solve FSI problems using a loosely-coupled method that has advantages of reusability of well-validated simulation codes for computational fluid dynamics (CFD) and computational structural dynamics (CSD) solvers. The framework consists of load projection, surface deformation, volume deformation, time mapping, and input/output control modules.

In this study, new algorithms for surface and volume deformation modules were developed. In the loosely-coupled method, interpolation (mapping) techniques are essential to transfer the data between CFD and CSD solvers that use different spatial discretization. A new hybrid deformation mapping method, Curvature gradient Index Local Fitting (CILF), was developed for motion transfer between unmatched unstructured grids on the common surfaces. CILF uses a surface spline method at local geometries having a high curvature gradient and a tracking method at the remaining geometries. This approach overcomes numerical instabilities and excessive computation time incurred by interpolating a large data set in the spline methods, as well as the low accuracy from tracking methods. Numerical results using two-dimensional analytical test functions and three-dimensional applications such as sphere and AGARD 445.6 wing deformation showed that the method provided efficient, accurate, and smooth interpolations in comparison to the traditional methods.

The movement of viscous (boundary) layers requires enormous computation time and memory due to grid condensation on the viscous layers. A simple and efficient topological local coordinate method was suggested for moving boundary layers. Based on the curvature gradient index, the new method uses an averaged point normal of moving surfaces and its relative angle to the local directional vector at local geometries having a high curvature gradient, and it uses a simple local coordinate at the remaining geometries. Whole volume grid movements from the fourth vibration modes of the AGARD 445.6 and NACA0012 wings were tested using the new method for boundary layers, and linear and semi-torisonal spring analogy for inviscid regions. The results demonstrated the efficiency of the suggested method.

For the purposes of validating the FSI framework developed, pulsatile blood flows through artificial straight/curved stenotic artery and in-vivo patient-specific femoral artery bifurcation and AGARD 445.6 wing flutter were simulated. In the artificial straight stenotic artery, the phase delay that can be detected only in FSI simulation was consistent with the experimental results, although there is a minor difference between the simulation and experimental results in terms of displacement. In the curved stenotic artery, strong recirculation of flow and high velocity on the outer wall indicates that the compliance and curvature of the artery plays a key role in the flow patterns and consequently affects wall shear stress (WSS) distribution on the wall.

The comparison of the flow patterns and WSS of rigid and compliant femoral artery bifurcation demonstrated that the FSI simulation that accounts for artery compliance is more in line with experimental data than flow only analysis in which the artery is just considered as a rigid one. The results of the biomechanical applications

demonstrated that the FSI framework can be a useful tool to enhance our understandings of the effects of biomechanical behaviors such as WSS and secondary flows on the development and progress of atherosclerosis.

Aircraft wing flutter is a physical phenomenon resulting from aeroelastic instability. Using the FSI framework, the flutter mode and frequency were obtained and their values were similar to experimental results. Instead of conventional modal approach, the time marching full dynamic method was performed in the FSI framework to provide a better insight of physical responses of the flutter such as large amplitude and time-dependent wing motion, separated flow, and turbulence.

The results of this study demonstrated that the FSI framework can be a useful and powerful tool to investigate and analyze real-world FSI phenomena.

REFERENCES

[1] Bathe, K.J., and Zhang, H., "Finite element developments for general fluid flows with structural interactions," *International Journal for Numerical Methods in Engineering*, Vol. 60, 2004, pp. 213-232

[2] Namkoong, K, Choi, H.G., and Yoo, J.Y., "Computation of dynamics fluid-structure interaction in two-dimensional laminar flows using combined formulation," *Journal of Fluids and Structures*, Vol. 20, 2005, pp.51-69

[3] Bennett, R. M. and Edwards, J. W., "An overview of recent developments in computational aeroelasticity," *AIAA Paper 98-2421,* 1998

[4] Dowell, E. H. and Hall, K. C., "Modeling of fluid-structure interaction," *Annu. Rev. Fluid Mech*. Vol. 33, 2001, pp. 445–90

[5] Tijsseling, A. S., "Fluid-structure interaction in liquid-filled pipe systems," *a review, Journal of Fluids and Structure,* Vol.10, 1996 pp.109-146

[6] Behr, M., Johnson, A., Kennedy, J., Mittal, S. and Tezduyar, T., "Computation of incompressible flows with implicit finite element implementations on the connection machine," *Computer Methods in Applied Mechanics and Engineering*, Vol. 108, 1993, pp. 99-118

[7] Kroyer, R., "FSI analysis in supersonic fluid flow," *Computers and Structures*, Vol. 81, 2003, pp. 755-764

[8] Carstens, V., Kemme, R., and Schmitt, S, "Coupled simulation of flow-structure interaction in turbomachinery," *Aerospace Science and Technology,* uncorrected, 2003

[9] Chiandussi, G., Bugeda, G. and Onate, E., "A simple method for automatic update of finite element meshes," *Commun*. *Numer*. *Meth*. *Engng*. Vol. 16, 2000, pp. 1-19

[10] Kevlahan, N. and Vasilyev, O. V., "An adaptive wavelet method for fluid structure interaction," *Direct and Large-Eddy Simulation-IV Workshop,* Enschede, The Netherlands, Jul 2001

[11] Sarrate, J., Huerta, A. and Donea, J., "Arbitrary Lagrangian–Eulerian formulation for fluid–rigid body interaction," *Computer Methods in Applied Mechanics and Engineering,* Vol. 190, Iss. 24-25, Mar 2001, pp. 3171-3188

[12] Gordnier, R. E., and Visbal, M. R., "Development of a three-dimensional viscous aeroelastic solver for nonlinear panel flutter," *Journal of Fluids and Structures,* Vol. 16, Iss. 4 , May 2002, pp. 497-527

[13] Sussman, T. and Sundqvist, J., "Fluid-structure interaction analysis with a subsonic potential-based fluid formulation," *Computers and Structures*, Vol. 81, No. 8-11, May 2003, pp. 949-962

[14] Tang, D., Yang, C. Walker, H., Kobayashi, S., and Ku, D. N., "Steady flow and wall compression in stenotic arteries: a 3-d thick-wall model with fluid-wall interactions," *Journal of Biomechanical Engineering,*Vol.123, 2001, pp. 548-557

[15] Tang, D., Yang, C. Walker, H., Kobayashi, S., and Ku, D.N., "A 3-d thin-wall model with flow-structure interactions for blood flow in carotid arteries with symmetric and asymmetric stenoses," *Computers and Structures*, Vol. 72, 1999, pp.357-377

[16] Tang, D., Yang, C. Walker, H., Kobayashi, S., and Ku, D.N., "Simulating cyclic artery compression using a 3D unsteady model with fluid structure interactions," *Computers and Structures*, Vol. 80, 2002, pp. 1651 – 1665

[17] Tang, D., Yang, C. Walker, H., Kobayashi, S., and Ku, D.N., "Effect of a lipid pool on stress/strain distributions in stenotic arteries: 3d FSI models," *Journal of Biomechanical Engineering,* Vol. 126, , June 2004, pp.363-370

[18] Whiting, B., and Neill, D. J., "Interfacing external, high order aerodynamics into MSC/NASTRAN for aeroelastic analyses," *MSC Aerospace User's Conference,* Nov 1997

[19] Love, M., Garza, T.D.L., Charlton, E., and Egle, D., "Computational aeroelasticity in high performance aircraft flight loads," *ICAS 2000 CONGRESS,* 2000

[20] Shkarayev, S., Krashantisa, R., and Tessler, A., "An inverse interpolation method utilizing in-flight strain measurements for determining loads and structural response of aerospace vehicles," *Proceedings of 3rd International Workshop on Structural Health Monitoring*, Stanford, CA, Sep 2001, pp. 336-343

[21] Kamakoti, R., Lian, Y., Regisford, S., Kurdila, A., and Shyy, W., "Computational aeroelasticity using a pressure-based solver," *AIAA 2002-0869,* 2002

[22] Potsdam, M. A., and Guruswamy, G. P., "A parallel multiblock mesh movement scheme for complex aeroelastic applications," *AIAA-2001-0716,* 2001

[23] Doi, H., "Fluid/Structure coupled aeroelastic computations for transonic flows in turbomachinery," *Proceedings of ASME Turbo Expo 2002*, Amsterdam, Jun 2002

[24] Beckert, A., "Coupling fluid (CFD) and structural (FE) models using finite interpolation elements," *Aerospace Science and Technology*, Vol. 4, Iss. 1 , Jan 2000, pp. 13-22

[25] Martins, J. R. R. A., Alonso, J. J., and Reuther, J. J., "High-fidelity aero-structural design optimization of a supersonic business jet," *AIAA 2002–1483*, 2002

[26] Ifju, P. G., Jenkins, D. A., Ettinger, S. Lian, Y. and Shyy, W., "Flexible-wing-based micro air vehicles," *AIAA 2002-0705,* 2002

[27] Melville, R., Gordnier, R., Rizzetta, D., Morgan, P., and Visbal, M., "Demonstration and validation of high fidelity fluid/structure analysis for flight vehicles," *UGC2002,* Austin, Texas, Jun 2002

[28] Zhang, W, Herrera, C., Atluri, S. N., and Kassab, G.S.,"Effect of surrounding tissue on vessel fluid and solid mechanics," *Journal of Biomechanical Engineering*, Vol. 126, Dec 2004, pp.760-769

[29] Kim, Y. H., and Kim, J. E., "New hybrid interpolation method for motion transfer in fluid structure interactions," *Journal of Aircraft*, Vol. 43, 2006, pp. 567-569

[30] Kim, Y. H., and Kim, J. E., "A modularized interface code with new interpolation method for analyzing fluid structure interaction," *Proceedings of SECTAM XXII,* Tuskegee, AL, Aug. 15-17, 2004

[31] Farhat, C., Lesoinne M., and LeTallec, P., "Load and motion transfer algorithms for fluid/structure interaction problems with non-matching discrete interfaces: Momentum and energy conservation, optimal discretization and application to aeroelasticity," *Computer Methods in Applied Mechanics and Engineering*, Vol. 157, 1998, pp.95-114

[32] Löhner, R., "Robust, vectorized search algorithms for interpolation on unstructured grids," *Journal of Computational Physics*, Vol. 118, 1995, pp. 380-387

[33] Harder, R. L., "Interpolation using surface splines," *Journal of Aircraft*, Vol. 9, 1972, pp.189-191

[34] Duchon, J., "Splines minimizing rotation-invariant semi-norms in sobolev spaces. constructive theory of functions of several variables," *Lecture Notes in Mathematics*, 1977, pp.85-100

[35] Hardy, R. L., "Multiquadric equations of topographic and other irregular surfaces," *Journal of Geophysical Research*, Vol. 76, 1971, pp.1905-1915

[36] Samareh, J.A., "Aeroelastic deflection of NURBS geometry," *Proceedings of 6th International Conference on Numerical Grid Generation in Computational Field Simulation.*, Univ. of Greenwich, Avery Hill Campus, London, UK, Jul. 1998

[37] Murti, V., and Valliappan, S., "Numerical inverse isoparametric mapping in remeshing and nodal quality contouring," *Computers & Structures*, Vol. 22, 1986, pp.1011–1021

[38] Pidaparti, R. M. V., "Structural and aerodynamic data transformation using inverse isoparametric mapping," *Journal of Aircraft*, Vol. 29, 1992, pp.507-509

[39] Byun, C., and Guruswamy G. P., "Wing-body aeroelasticity on parallel computers," *Journal of Aircraft*, Vol. 33, 1996, pp. 421-428

[40] Maman, N., and Farhat, C., "Matching fluid and structure meshes for aeroelastic computations: A parallel approach," *Computers & Structures*, Vol. 54, 1995, pp.779-785

[41] Cebral, J. R., and Löhner, R., "Conservative load projection and tracking for fluid-structure problems," *AIAA Journal*, Vol. 35, 1997, pp.687-692

[42] Smith, M.J., Hodges, D.H., and Cesnik, C. E. S., "Evaluation of computational algorithms suitable for fluid-structure interactions," *Journal of Aircraft*, Vol. 37, 2000, pp.282-294

[43] Smith, M.J., Hodges, D.H., and Cesnik, C. E. S., "An evaluation of computational algorithms to interface between CFD and CSD methodologies," *U.S. Air Force Research Lab. TR-96-3055*, Nov. 1995.

[44] Kim, Y. H., and Kim, J. E., "A new hybrid interpolation method using surface tracking, fitting and smoothing function applied for aeroelasticity," *AIAA Paper 2005-2347, Proceedings of 46th AIAA/ASME/ASCE/AHS/ASC Structures, Structural Dynamics and Materials Conference*, Austin, TX, Apr., 18-21, 2005.

[45] Batina, J. T., "Unsteady Euler airfoil solutions using unstructured dynamic meshes," *AIAA Paper 89-0115*, 27th AIAA Aerospace Sciences Meeting, January, 1989.

[46] Farhat, C., Degand, C., Koobus, B., and Lesoinne, M., "Torsional springs for two-dimensional dynamic unstructured fluid meshes," *Computational Methods in Applied Mechanics and Engineering*, Vol.163, 1998, pp. 231-245

[47] Bottasso, C. L., Davide, D., and Serra, R., "The ball-vertex method: a new simple spring analogy method for unstructured dynamic meshes," *Computational Methods in Applied Mechanics and Engineering*, Vol.194, 2005, pp.4244-4264

[48] Degand, C., and Farhat, C., "A three-dimensional torsional spring analogy method for unstructured dynamic meshes," *Computers and Structures,* Vol. 80, 2002, pp. 305-316

[49] Murayama, M., Nakahashi, K., and Matsushima, K., "Unstructured dynamic mesh for large movement and deformation," *AIAA Paper 2002-0122*, 40th AIAA Aerospace Sciences Meeting, January, 2002

[50] Burg, C. O. E., "A robust unstructured grid movement strategy using three-dimensional torsional springs," *AIAA Paper 2004-2529,* 2004

[51] Zeng, D., and Ethier, R., "A semi-torsional spring analogy model for updating unstructured meshes in 3D moving domains," *Finite Elements in Analysis and Design*, Vol. 41, 2005, pp.1118-1139

[52] Johnson, A. and Tezduyar, T., "Mesh update strategies in parallel finite element computations of flow problems with moving boundaries and interfaces," *Computational Methods in Applied Mechanics*, Vol.119**,** 1994, pp.73–94

[53] Lin, P., Martinelli, L., and Baker, T. J., "Time dependent calculations on adaptive unstructured meshes with Time evolving boundaries,", *AIAA 2002-0858*, Reno, 2002

[54] Johnson, A. and Tezduyar, T., "Simulation of multiple spheres falling in a liquid-filled tube," *Computational Methods in Applied Mechanics and Engineering*, Vol.134, 1996, pp.351-373

[55] Yang, Z., Mavriplis, D. J., "Unstructured dynamic meshes with higher-order time integration schemes for the unsteady navier-stokes equations," *AIAA 2005-1222*, Reno, 2005

[56] Chiandussi, G., Bugeda, G., and Oñate, E., "A simple method for automatic update of finite element meshes," *Communications in Numerical Methods in Engineering*, Vol.16, 2000, pp. 1-19

[57] Kim, D. H., Park, Y. M., Lee, I., and Kwon, O. J., "Nonlinear aeroelastic computation of wings with pylon/finned-store using parallel unstructured Euler solver," *AIAA 2002–1289,* Reno, 2002

[58] Zhang, S., and Belegundu, A. D., "A systematic approach for generating velocity fields in shape optimization," *Structural Optimization*, Vol. 5, 1993, pp. 84–94

[59] Kholodar, D., Morton, S. and Cummings, R., "Deformation of unstructured viscous grids," *AIAA-2005-926*, 2005

[60] Farhat, C., and Lesoinne, M., "Two efficient staggered algorithms for the serial and parallel solution of three-dimensional nonlinear transient aeroelastic problems," *Computer Methods in Applied Mechanics and Engineering,* Vol. 182, n 3-4, Feb. 2000, pp. 499-515

[61] Piperno, S., Farhat, C., and Larrouturou, B., "Partitioned procedures for the transient solution of coupled aeroelastic problems Part I: Model problem, theory and two-dimensional application," *Computer Methods in Applied Mechanics and Engineering,* Vol. 124, No. 1-2, Jun 15, 1995, pp.79-112

[62] Piperno, S., Farhat, C., and Larrouturou, B., "Partitioned procedures for the transient solution of coupled aeroelastic problems Part II: Energy transfer analysis and three-dimensional applications," *Computer Methods in Applied Mechanics and Engineering*, Vol. 190, No. 24-25, Mar 2, 2001, pp.3147-3170

[63] Piperno, S., "Explicit/Implicit fluid/structure staggered procedures with a structural predictor and fluid subcycling for 2d inviscid aeroelastic simulations," *International Journal for Numerical Methods in Fluids,* Vol. 25, No. 10, Nov 30, 1997, pp.1207-1226

[64] Farhat, C., Geuzaine, P., and Brown, G., "Application of a three-field nonlinear fluid-structure formulation to the prediction of the aeroelastic parameters of an F-16 fighter," *Computers & Fluids* Vol. 32, 2003, pp.3–29

[65] Li, K., Santamore, W. P., Morley, D. L. and Tulenko, T. N., " Stenotic amplification of vasoconstriction responses," *Americal Journal of Physiology. Heart and Circulatory Physiology,* 1989, pp. H1041-1051

[66] Cao, J. and Rittgers, S. E., "Particle motion within in vitro models of stenosed internal carotid and left anterior descending coronary arteries," *Annals of Biomedical Engineering,* Vol. 26, 1998, pp.190–199

[67] Gach, H. M., and Lowe, I. J., "Measuring flow reattachment lengths downstream of a stenosis using MRI," *Journal of Magnetic Resonance Imaging*, Vol. 12 pp.939–948

[68] Doriot, P., "Estimation of the supplementary axial wall stress. generated at peak flow by an arterial stenosis," *Physics In Medicine And Biology,* Vol. 48, 2003, pp.127-138

[69] Ku, D. N., Kobayashi, S., Wootton, D. M., and Tang, D., "Compression from dynamic pressure conditions in models of arterial disease," *Annals of Biomedical Engineering,* Vol. 25(supp. 1), pp.S-22

[70] Ku, D. N., Zeigler M. N., and Downing, J. M., "One-dimensional steady inviscid flow through a stenotic collapsible tube," *Journal of Biomechanical Engineering,* Vol. 112, 1990, pp. 444–450

[71] Mittal, R., Simmons, S. P., and Udaykumar, H. S., "Application of large-eddy simulation to the study of pulsatile flow in a modeled arterial stenosis," *Journal of Biomechanical Engineering,* Vol. 123, 2001, pp.325-332

[72] Mallinger, F., and Drikakis, D., "Instability in three-dimensional, unsteady, stenotic flows," *Heat and Fluid Flow*, Vol. 23, 2002, pp.657-663

[73] Lee, T. S., Liao, W., and Low, H. T., "Numerical simulation of turbulent. ow through series stenoses," *International Journal for Numerical Methods in Fluids,* Vol. 42, 2003, pp.717-740

[74] Varghese, S. S., and Frankel, S.H., "Numerical modeling of pulsatile turbulent flow in stenotic vessels," *Journal of Biomechanical Engineering,* Vol.125, 2003, pp.445-460

[75] Ryval, J., Straatman, A. G., and Steinman, D.A., "Two-equation turbulence modeling of pulsatile flow in a stenosed tube," *Journal of Biomechanical Engineering,* Vol. 126, 2004, pp.625-35

[76] Yao, H., Ang, K.C., Yeo, J. H., and Sim, E. K., "Computational modelling of blood flow through curved stenosed arteries," *Journal of Medical Engineering & Technology*, Vol. 24, 2000, pp.163–168

[77] Mooney, M., "A theory of large elastic deformation," *Journal of Applied Physics*, Vol.11, 1940, pp.582–592

[78] Fung, Y.C., Fronek, K., and Patitucci, P., "Pseudoelasticity of arteries and the choice of its mathematical expression," *Americal Journal of Physiology. Heart and Circulatory Physiology,* Vol. 237, 1979, pp. H620–631

[79] Chuong, C. J., and Fung, Y. C., "Three-dimensional stress distribution in arteries," *Journal of Biomechanical Engineering,* Vol. 105, 1983, pp.268-274

[80] Takamizawa K., and Hayashi, K., "Strain energy density function and uniform strain hypothesis for arterial mechanics," *Journal of Biomechanical Engineering,* Vol. 20, 1987, pp.7–17

[81] Vaishnav, R. N., Young, J. T., Janicki, J. S., and Patel, D. J., "Distribution of stresses and of strain-energy density through the wall thickness in a canine aortic segment," *Circulation Research,* Vol. 32, 1973, pp.577–83

[82] Humphrey, J. D., "An evaluation of pseudoelastic descriptors used in arterial mechanics," *Journal of Biomechanical Engineering,* Vol. 121, 1999, pp.259–62

[83] Holzapfel, G. A., Gasser, T. C., and Ogden, R. W., "A new constitutive framework for arterial wall mechanics and a comparative study of material models," *Journal of Elasticity* Vol. 61, 2000, pp.1–48

[84] Chuong, C. J., and Fung, Y. C., "On residual stresses in arteries," *Journal of Biomechanical Engineering,* Vol.108, 1986, pp.189–192

[85] Zulliger, M. A., Fridez, P., Hayashi, K., and Stergiopulos, N., "A strain energy function for arteries accounting for wall composition and structure," *Journal of Biomechanics,* Vol. 37, 2004, pp.989–1000

[86] Vito, R. P., and Dixon, S. A., "Blood vessel constitutive models—1995–2002," *Annual Review of Biomedical Engineering,* Vol. 5, 2003 pp.413-439

[87] Gow, B. S., and Taylor, M. G., "Measurement of viscoelastic properties of arteries in the living dog," *Circulation Research,* Vol. 23, 1968, pp.111-122

[88] Anliker, M., Moritz, W. E., and Ogden, E., "Transmission characteristics of axial waves in blood vessels," *Journal of Biomechanics,* Vol.1, 1968, pp.235-246

[89] Vaishnav, R. N., Vossoughi, J., Patel D. J., Cothran, L. N., Coleman, B. R., and Ison-Franklin, E. L., "Effect of hypertension on elasticity and geometry of aortic tissue from dogs,"*Journal of Biomechanical Engineering,* Vol. 112, 1990, pp.70-74

[90] Rachev, A., Stergiopulos, N., and Meister, J. J., "A model for geometric and mechanical adaptation of arteries to sustained hypertension," *Journal of Biomechanical Engineering,* Vol. 120, 1998, pp.9-17

[91] Armentano, R. L., Megnien, J. L., Simon, A., Bellenfant, F., Barra, J., and Levenson, J., "Effects of hypertension on viscoelasticity of carotid and femoral arteries in humans," *Hypertension*, Vol. 26, 1995, pp.48 -54

[92] Armentano, R. L., Graf, S., Barra, J. G., Vehkovsky, G., Baghvo, H., Sinchez, R., Simon, A., Pichel, R. H., and Levenson, J., "Carotid wall viscosity increase is related to intima-media thickening in hypertensive patients," *Hypertension,* Vol. 31, 1998, pp.534-539

[93] Young, J. T., Vaishnav, R. N., and Patel, D. J., "Nonlinear anisotropic viscoelastic properties of canine arterial segments," *Journal of Biomechanics,* Vol. 10, 1977, pp.549-559

[94] Cheung, J. B., and Hsiao, C. C., "Nonlinear anisotropic viscoelastic stresses in blood vessels," *Journal of Biomechanics,* Vol. 10, 1972, pp.607-619

[95] Wu, S. G., and Lee G. C., "On nonlinear viscoelastic properties of arterial tissue *Journal of Biomechanical Engineering,* Vol. 106, 1984, pp.42-47

[96] Demiray, H., "A quasi-linear constitutive relation for arterial wall materials," *Journal of Biomechanics,* Vol. 29, 1996, pp 1011-1014

[97] Holzapfel, G. A., Gasser, T. C., and Stadler, M., "A structural model for the viscoelastic behavior of arterial walls: continuum formulation and finite element simulation," *European Journal of Mechanics. A Solids*, Vol. 21, 2000, pp.441–63

[98] Kaazempur-Mofrad, M. R., Younis, H. F., Patel, S., Isasi, A., Chung, C., Chan, R.C., Hinton D. P., Lee, R. T, and Kamm, R. D., "Cyclic strain in human carotid bifurcation and its potential correlation to atherogenesis: Idealized and anatomically-realistic models," *Journal of Engineering Mathematics*, Vol. 47, 2003, pp.299-314

[99] Lally, C., Dolan, F., and Prendergast, P. J., "Cardiovascular stent design and vessel stresses: a finite element analysis," *Journal of Biomechanics*, Vol. 38, 2005, pp.1574–1581

[100] Kim, Y. H., Kim, J. E., Choi, M., and Baek, J., "Multiphysics modeling and simulation of pulsatile flow through a curved stenotic artery," *The Huntsville Simulation Conference 2005, The Society for Modeling and Simulation International*, Huntsville, AL, Oct., 26-27, 2005.

[101] Sanctis, J. T. D., "Percutaneous interventions for lower extremity peripheral vascular disease," *American family physician,* Vol. 64, 2001, pp. 1965-1972

[102] Becker, G. J., McClenny, T. E., Kovacs, M.E., Raabe, R. D., and Katzen, B. T., "The importance of increasing public and physician awareness of peripheral arterial disease," *J. Vasc. Interv. Radiol.*, Vol. 13, 2002, pp. 7−11

[103] Smedby, Ö., Johansson, J., Mölgaard, J., Olsson, A. G., Walldius, G., and Erikson, U., "Predilection of atherosclerosis for the inner curvature in the femoral artery," *Arteriosclerosis, Thrombosis, and Vascular Biology,* Vol.15, 1995, pp.912-917

[104] Smedby, Ö., Nilsson, S., and Bergstrand, L., "Development of femoral atherosclerosis in relation to flow disturbance," *Journal of Biomechanics*, Vol. 29, 1996, pp.543-547

[105] Jones, C. J. H., Lever, M. J., Ogasawara, Y., Parker, K. H., Tsujioka, K., Hiramatsu, O., Mito, K., Caro, C. G., and Kajiya, F., "Blood velocity distributions within intact canine arterial bifurcations," *American Journal of Physiology*, Vol. 262, 1992, pp. H1592 - H1599

[106] Wensing, P. J. W., Meiss, L., and Mali, W. P. T. M., and Hillen, B., "Early atherosclerotic lesions spiraling through the femoral artery," *Arterioscler. Thromb. Vasc. Biol.,* Vol. 18, 1998, pp. 1554-1558

[107] Anayiotos, A., Jones, S., Giddens, D. P., Glagov, S., and Zarins, C. K., "Shear stress at a compliant model of the human carotid bifurcation," *Journal of Biomechanical Engineering,* Vol. 116, 1994, pp.98-106

[108] Anayiotos, A.S., Pedroso, P.D., Elefhteriou, E.C., Venugopalan, R., and Holman, W., "Effect of A flow-streamlining implant at the distal anastomosis of a coronary artery bypass graft," *Annals of Biomedical Engineering,* Vol. 30, 2002, pp. 917-926

[109] Gijsen, F. J. H., Palmen, D. E. M., van der Beek, M. H. E., van de Vosse F. N., van Dongen, M. E. H., and Janssen, J. D., "Analysis of the axial flow field in stenosed carotid artery bifurcation models--LDA experiments," *Journal of Biomechanics*, Vol. 29, 1996, pp. 1483-1489

[110] Ku, D. N., Giddens, D. P., Zarins, C. K., and Glagov, S., "Pulsatile flow and atherosclerosis in. the human carotid bifurcation," *Atheriosclerosis*, Vol. 5, 1985, pp. 293–302

[111] Caro, C. G., Parker, K. H., Fish, P.J. and Lever, M. J., "Blood flow near the arterial wall and arterial disease," *Clin. Hemorheol*., Vol. 5, 1985, pp. 849-871

[112] Rhee, K., and Lee, S. M., "Effects of radial wall motion and flow waveform on the wall shear rate distribution in the divergent Vascular Graft," *Annals of Biomedical Engineering,* Vol. 26, 1998, pp. 955–964

[113] Wu, S.P., Ringgaard, S., Oyre, S., Hansen, M.S., Rasmus, S., Pedersen, E. M., "Wall shear rates differ between the normal carotid, femoral, and brachial arteries: an in vivo MRI study," *J. Magn. Reson. Imaging*, Vol. 19, 2004, pp. 188‐193

[114] Chen, J., and Lu, X. Y., "Numerical investigation of the non-Newtonian pulsatile blood flow in a bifurcation model with a non-planar branch," *Journal of Biomechanics*, Vol.39, 2006, pp. 818-832

[115] Starmans-Kool, M. J., Stanton, A. V., Zhao, S., Xu, X. Y., Thom, S. A., and Hughes, A. D., "Measurement of hemodynamics in human carotid artery using ultrasound and computational fluid dynamics," *J. Appl. Physiol.,* Vol, 92, 2002, pp. 957 – 961

[116] Kornet, L., Hoeks, A. P., Lambregts, J., and Reneman, R. S., "Mean wall shear stress in the femoral arterial bifurcation is low and independent of age at rest," *J. Vasc. Res.* Vol. 37, 2000, pp.112-122

[117] Kornet, L., Hoeks, A. P., Lambregts, J., and Reneman, R. S., "In the femoral artery bifurcation, differences in mean wall shear stress within subjects are associated with different intima-media thickness," *Arterioscler. Thromb. Vasc. Biol*. Vol. 19, 1999, pp. 2933-2939

[118]Liu, Y., Hamilton, A., Nagaraj, A., Yan, L. L., Liu, K., Lai, Y-G., McPherson, D. D., and Chandran, K. B., "Alteration in fluid mechanics in porcine femoral arteries with atheroma development, Annals of Biomedical Engineering," Vol. 32, 2004, pp. 544–554

[119] Stroud, J. S., Berger, S. A., and Saloner, D., "Numerical analysis of flow through a severely stenotic carotid artery bifiurcation," *Journal of Biomechanical Engineering,* Vol.124, 2002, pp. 9-20

[120] Fukushima, E., ‘‘Nuclear magnetic resonance as a tool to study flow,’’ *Annu. Rev. Fluid Mech.,* Vol. 31, 1999, pp. 95–123

[121] Jou, L. D., van Tyen, R., Berger, S. A., and Saloner, D., ‘‘Calculation of the Magnetization Distribution for Fluid Flow in Curved Vessels,’’ *Magn. Reson. Med.,* Vol. 35, 1996, pp. 577–584

[122] Botnar, R., Rappitsch, G., Scheidegger, M. B., Liepsch, D., Perktold, K., and Boesiger, P., “Hemodynamics in the carotid artery bifurcation: a comparison between numerical simulations and in vitro MRI measurements,” *Journal of Biomechanics,* Vol. 33, 2000, pp. 137-144

[123] Hyun, S., Kleinstreuer, C., and Archie, J. P., “Computational analysis of effects of external carotid artery flow and. occlusion on adverse carotid bifurcation hemodynamics,” *J. Vascular Surgery,* Vol. 37, 2003, pp. 1248-1254

[124] Ku, J. P., Elkins, C. J., and Taylor, C. A., "Comparison of CFD and MRI flow and velocities in an in vitro large artery bypass graft model," *Annals of Biomedical Engineering,* Vol. 33, 2005, pp. 257-269

[125] Lei, M., Kleinstreuer, C., and Archie, J. P., “Geometric design improvements for femoral graft-artery junctions mitigating restenosis,” *Journal of Biomechanics*, Vol. 29, 1996, pp. 1605−1614

[126] Liou, T., Li, Y., and Juan, W., “Numerical and experimental studies on pulsatile flow in aneurysms arising laterally from a curved parent vessel at various angles,” *Journal of Biomechanics* (In Press) Accepted 25 May 2006

[127] Sherwin, S. J., Shah, O., Doorly, D. J., Peiro J., Papaharilaou, Y., Watkins, N., Caro, C. G., and Dumoulin, C. L., “The influence of out-of-plane geometry on the flow within a distal end-to-side anastomosis,” *Journal of Biomechanical Engineering,* Vol.122, 2000, pp. 86-95

[128] Birchall, D., Zaman, A., Hacker, J., Davies G., and Mendelow, D., “Analysis of haemodynamic disturbance in the atherosclerotic carotid artery using computational fluid dynamics,” *Eur. Radiol.* Vol. 16, 2006, pp. 1074–1083

[129] Giordana, S., Sherwin, S. J., Peiro, J., Doorly, D. J., Crane, J. S., Lee, K. E., Cheshire, N. J. W., and Caro, C. G., “Local and global geometric influence on steady flow in distal anastomoses of peripheral bypass grafts,” *Journal of Biomechanical Engineering*, Vol. 127, 2005, pp. 1087 – 1098

[130] Köhler, U., Marshall, I., Robertson, M. B., Long, Q., Xu, X. Y., and Hoskins, P., "MRI measurement of wall shear stress vectors in bifurcation models and comparison with CFD predictions," *J. Magn. Reson. Imaging,* Vol. 14, 2001, pp. 563–573

[131] Long, Q., Xu, X. Y., Ariff, B., Thom, S. A., Hughes, A. D., Stanton, A. V., "Reconstruction of blood flow patterns in a human carotid bifurcation: A combined CFD and MRI study," *J. Magn. Reson. Imaging*, Vol. 11, 2000, pp. 299 – 311

[132] Marshall, I., Zhao, S., Papathanasopoulou, P., Hoskins, P., Xu, Y., "MRI and CFD studies of pulsatile flow in healthy and stenosed carotid bifurcation models," *Journal of Biomechanics,* Vol. 37, 2004, pp. 679-87

[133] Myers, J. G., Moore, J. A., Ojha, M., Johnston, K. W., and Ethier, C. R., "Factors influencing blood flow patterns in the human right coronary artery," *Annals of Biomechanical Engineering*, Vol. 29, 2001, pp. 109-120

[134] Steinman, D. A., Thomas, J. B., Ladak, H. M., Milner, J. S., Rutt, B. K., and Spence, J. D., "Reconstruction of carotid bifurcation hemodynamics and wall thickness using computational fluid dynamics and MRI," *Magn. Reson. Med.* Vol. 47, 2002, pp. 149-159

[135] Steinman, D. A., "Image-based computational fluid dynamics modeling in realistic arterial geometries," *Annals of Biomedical Engineering*, Vol. 30, 2002, pp. 483-97

[136] Kaazempur-Mofrad, M. R., Isasi, A. G., Younis, H. F., Chan, R. C., Hinton, D. P., Sukhova, G., LaMuraglia, G. M., Lee, R. T., and Kamm, R. D., "Characterization of the atherosclerotic carotid bifurcation using MRI finite element modeling, and histology," *Annals of Biomedical Engineering*, Vol. 32, 2004, pp. 932–946

[137] Zhao, S. Z., Papathanasopoulou, P., Long, Q., Marshall, I., and Xu, X. Y., "Comparative study of magnetic resonance imaging and image-based computational fluid dynamics for quantification of pulsatile flow in a carotid bifurcation phantom," *Annals of Biomedical Engineering*, Vol. 31, 2003, pp. 962–971

[138] Cebral, J. R., Yim, P. J., Loehner, R., Soto, O., and Choyke, P.L., "Blood flow modeling in carotid arteries with computational fluid dynamics and MR imaging," *Academic Radiology,* Vol. 9, pp. 1286-1299

[139] Li, Z., and Kleinstreuer, C., "Fluid-structure interaction effects on sac-blood pressure and wall stress in a stented aneurysm," *Journal of Biomechanical Engineering,* Vol. 127, 2005, pp. 662-671

[140] Maurits, N.M, Loots, G. E., and Veldman, A. E., "The influence of vessel wall elasticity and peripheral resistance on the carotid artery flow wave form: A CFD model compared to in vivo ultrasound measurements," *Journal of Biomechanical Engineering*, (In Press) Accepted 14 December 2005

[141] Moayeri, M. S., and Zendehbudi, G. R., "Effects of elastic property of the wall on flow characteristics through arterial stenosis," *Journal of Biomechanics,* Vol. 36, 2003, pp. 525-35

[142] Perktold, K., and Rappitsch, G., "Computer-simulation of local blood-flow and vessel mechanics in a compliant carotid-artery bifurcation model," *Journal of Biomechanics*, Vol. 28, 1995, pp. 845- 856

[143] Ramaswamy, S. D., Vigmostad, S. C., Wahle, A., Lai, Y. G., Olszewski, M. E., Braddy, K. C., Brennan, T. M., Rossen, J. D., Sonka, M., Chandran, K. B., "Fluid dynamic analysis in a human left anterior descending coronary artery with arterial motion," *Annals of Biomedical Engineering*, Vol. 32, 2004, pp. 1628-1641

[144] Tang, D. L., Yang, C., Zheng, J., Woodard, P. K., Sicard, G. A., Saffitz, J. E., and Yuan, C., "3D MRI-based multicomponent FSI models for atherosclerotic plaques," *Annals of Biomedical Engineering*, Vol. 32, 2004, pp. 947-960

[145] Younis, H. F., Kaazempur-Mofrad, M. R., Chan, R.C., Isasi, A. G., Hinton, D. P., Chau, A. H., Kim, L. A., and Kamm, R. D., "Hemodynamics and wall mechanics in human carotid bifurcation and its consequences for atherogenesis: investigation of Inter-Individual Variation," *Biomech. Model. Mechanobiol.,* Vol. 3, 2004, pp. 17–32

[146] Younis, H. F., Kaazempur-Mofrad, M. R., Chung, C., Chan, R. C., and Kamm, R. D., "Computational analysis of the effects of exercise on hemodynamics in the carotid bifurcation," *Annals of Biomedical Engineering,* Vol. 31, 2003, pp. 995-1006

[147] Zhao, S. Z., Xu, X. Y., Hughes, A. D., Thom, S. A., Stanton, A. V., Ariff, B., and Long, Q., "Blood flow and vessel mechanics in a physiologically realistic model of a human carotid arterial bifurcation, Journal of Biomechanics," Vol. 33, 2000, pp. 975-984

[148] http://www.eng.uab.edu/me/ETLab/

[149] Ito, Y., Shum, P. C., Shih, A. M., Soni, B. K., Nakahashi, K., "Robust generation of high-quality unstructured meshes on realistic biomedical geometry," *Int. J. Num. Meth. Eng.,* Vol. 65, 2006, pp. 943-973

[150] Smilde, T. J., van den Berkmortel, F. W., Boers, G. H., Wollersheim, H., de Boo, T., van Langen, H., and Stalenhoef, A. F., "Carotid and femoral artery wall thickness and stiffness in patients at risk for cardiovascular disease, with special emphasis on hyperhomocysteinemia," *Arterioscler. Thromb. Vasc. Biol.* Vol. 18, 1998, pp. 1958–1963

[151] Prendergast, P. J., Lally, C., Daly, S., Reid, A. J., Lee, T. C., Quinn, D., and Dolan, F., "Analysis of prolapse in cardiovascular stents: a constitutive equation for vascular tissue and finite element modeling," *Journal of Biomechanical Engineering,* Vol. 125, 2003, pp. 692−699

[152] Tai, N. R., Giudiceandrea, A., Salacinski, H. J., Seifalian, A. M., and Hamilton, G., "In vivo femoropopliteal arterial wall compliance in subjects with and without lower limb vascular disease," *J. Vasc. Surg.*, Vol. 30, 1999, pp. 936–945

[153] Berger, S. A., "Flow in large vessels," In: Cheer, A. Y., van Dam, C. P., eds. *Contemporary mathematics: fluid dynamics in biology.* Providence, RI: American Mathematical Society, 1993, pp. 479–518

[154] Higgins, C., B., and Roos, A., *MRI and CT of the Cardiovascular System*, *Second Edition*, Lippincott Williams & Wilkins

[155] Kim, Y. H., and Kim, J. E., "A new feature preserving smoothing interpolation method in partitioned multidisciplinary problems," *The Sixth Mississippi State - UAB Conference on Differential Equations & Computational Simulations*, Mississippi State University, MS, May 13-14, 2005.

[156] Kim, Y. H., Kim, J. E., Ito, Y., Shih, A. M., and Anayiotos, A., "Hemodynamic of the in-vivo common femoral artery bifurcation using loosely-coupled fluid structure interaction framework," *The Huntsville Simulation Conference 2006, The Society for Modeling and Simulation International*, Huntsville, AL, Oct., 17-19, 2006

[157] Mukhopadhyay, V., "Wing flutter analysis and parametric study," Langley Research Center, Hampton, Virginia, *NASA-TM- 110276,* 1996

[158] Sadeghi, M., Yang, S., Liu, F., and Tsai, H.M., "Parallel computation of wing flutter with a coupled Navier-Stokes/CSD method," *AIAA-2003-1347,* 2003

[159] Lee-Rausch, E. M., and Batina, J. T., "Wing flutter boundary prediction using unsteady Euler aerodynamic method," *Journal of Aircraft*, Vol. 32, 1995, pp. 416−422

[160] Yates, E. C. Jr., "AGARD Standard Aeroelastic Configurations for Dynamic Response, Candidate Configuration I. Wing 445.6," *AGARD-R- 765,* 1985

[161] Liu, F., Cai, J., Zhu, Y., Tsai, H. M., and Wong, A. S. F., "Calculation of wing flutter by a coupled fluid-structure Method," *Journal of Aircraft,* Vol. 38, 2001, pp. 334-342

[162] Stephens, C. H., Arena, Jr., A. S., and Gupta, K. K., "Application of the Transpiration Method for Aeroservoelastic Prediction using CFD," *AIAA 98-2071*, 1998

[163] Lee-Rausch M.E., and Batina, J., "Calculation of AGARD wing 445.6 flutter using Navier-Stokes aerodynamics", *AIAA 93-3476,* 1993

[164] Yosibash, Z., Kirby, R.M., Myers, K., Szabo, B., and Karniadakis, G., "High-order finite elements for fluid structure interaction problems," *AIAA-2003-1729,* 2003